MECHANICAL AND ELECTRICAL CHARACTERIZATION OF PRINTED FLEXIBLE ELECTRONICS DEFORMED OVER COMPLEX SURFACES

A Thesis
Presented to
The Academic Faculty

by

Isaac A. Bower

In Partial Fulfillment
of the Requirements for the Degree
Master of Science in the
George W. Woodruff School of Mechanical Engineering

Georgia Institute of Technology
December 2018

MECHANICAL AND ELECTRICAL CHARACTERIZATION OF PRINTED FLEXIBLE ELECTRONICS DEFORMED OVER COMPLEX SURFACES

Approved by:

Dr. Suresh K. Sitaraman, Advisor
School of Mechanical Engineering
Georgia Institute of Technology

Dr. Emmanouil M. Tentzeris
School of Electrical and Computer Engineering
Georgia Institute of Technology

Dr. W. Hong Yeo
School of Mechanical Engineering
Georgia Institute of Technology

Date Approved: December 5, 2018

ACKNOWLEDGEMENTS

I would first like to thank Dr. Suresh Sitaraman for being my advisor and helping me through the graduate school process. He has not only provided me with the resources to complete my research, but also helped me grow and learn how to approach complex academic problems. In addition, I would like to thank Dr. Manos Tentzeris and Dr. Hong Yeo for being on my committee and providing valuable feedback on my research.

I would also like to thank the members of the Computer-Aided Simulation of Packaging Reliability (CASPaR) Lab. They have not only helped and provided me with insight, but also have become good friends.

I would like to thank the other graduate students involved in the NextFlex 2.6: Flexible Antenna Array Technology (FAAT) project for their help. In addition, I would like to thank Dr. John Williams and Dr. John Rogers of Boeing Corporation for their input and support of the project.

I would like to thank my parents for their love and support. Their encouragement and help have enabled me to accomplish this milestone. I would not be where I am without them.

I would like acknowledge that this thesis work is based, in part, on research sponsored by Air Force Research Laboratory under agreement number FA8650-15-2-5401, as conducted through the flexible hybrid electronics manufacturing innovation institute, NextFlex. The U.S. Government is authorized to reproduce and distribute reprints for Governmental purposes notwithstanding any copyright notation thereon. The views and

conclusions contained herein are those of the author and should not be interpreted as necessarily representing the official policies or endorsements, either expressed or implied, of Air Force Research Laboratory or the U.S. Government.

TABLE OF CONTENTS

LIST OF TABLES

LIST OF FIGURES

SUMMARY

In many different applications, substrates with flexible electronics are bent or adhered to complex curved surfaces. Therefore, it is vital to understand how the performance of these flexible electronics changes, when the substrates with flexible electronics are deformed over these complex surfaces. In this thesis, tests were developed for characterizing the mechanical and electrical performance of printed sensors and antennas deformed over various surfaces such as a spherical dome and a saddle. The sensors and the antennas were fabricated by inkjet printing silver nanoparticle ink on flexible polymer substrates such as polyethylene terephthalate (PET), polyimide, and liquid crystal polymer (LCP). Test fixtures were designed for attaching to a universal test machine, and were fabricated using 3D printing of PolyLactic Acid (PLA). These fixtures were used to test the printed sensors and antennas under monotonic and cyclic loadings. The electrical performance and the fatigue behavior of the printed structures were monitored in situ during the tests. Scanning Electron Microscopy (SEM) imaging was used to examine the effect of the deformations on the ink microstructure. In addition to the physical testing, simulations of the various deformation cycles were conducted on the sensors and antennas. Through simulations, the stress and strain distributions were examined in the deformed structures, and the changes in electrical characteristics with deformed shapes were determined through experiments. Also, relationships between the change in electrical resistance and the applied strain were determined. This work provides both a test methodology for deforming flexible electronics on complex surfaces as well as a better understanding of how printed silver inks will perform under such deformations.

CHAPTER 1

INTRODUCTION

Flexible electronics is an emerging field with an immense amount of applications such as human health monitoring [1, 2], communications [3, 4], wearable and smart fabrics [5, 6], and others Being able to be bent, stretched, twisted, folded, and conformed to surfaces are attractive properties for flexible electronics. These properties provide ease of use, durability, comfort, and adaptability.

Recently, there is increased interest in printed electronics on flexible substrates to facilitate various stretching, bending, twisting, and folding operations. These printing methods are used to apply various materials such as conductors [7] and dielectrics [5]. Popular printing methods include inkjet, aerosol, screen, gravure, and flexographic printing. Figure 1 shows screen, gravure, inkjet, and micro-dispense [8], Figure 2 shows aerosol jet [9], and Figure 3 shows flexographic [10] printing methods used to fabricate flexible electronics.

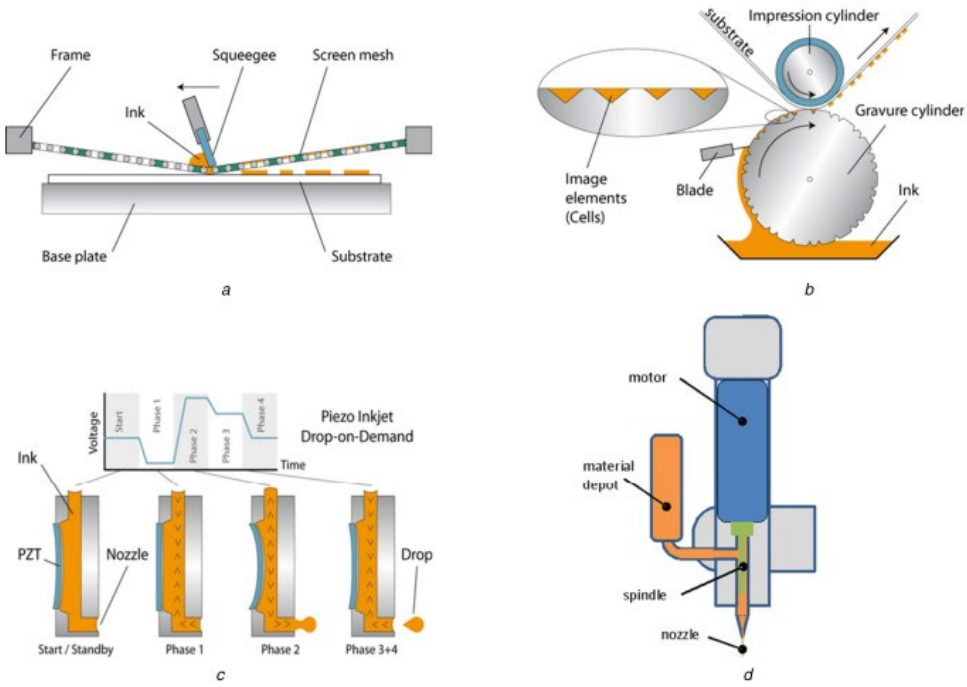

Figure 1: Various printing methods for fabricating flexible electronics. a) Screen, b) Gravure, c) Inkjet, and d) Micro-dispense [8]

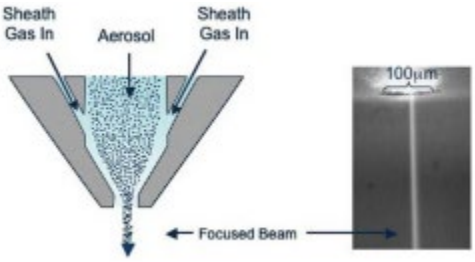

Figure 2: Aerosol Jet® printing [9]

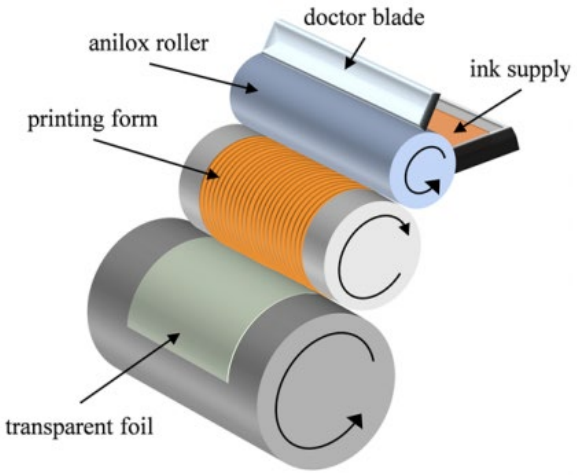

Figure 3: Flexographic printing [10]

Each of the different printing techniques has its own set of advantages and disadvantages. For example, Gravure and flexographic printing are good for large production but has expensive initial tooling setups. Inkjet printing is initially cheaper, but has issues with thermal compatibility of substrates with curing processes required by the inks. Aerosol jet printing can produce fine features, but is slow. Screen printing is cost effective and easy to use, but has feature size limitations. Micro-dispense printing allows the dispensing of very viscous inks, but also has feature size limitations. The ideal printing method depends on many factors such as feature size, length of production run, and type of substrate.

Various substrates are used in the fabrication of flexible electronics such as polymers, glass, metals, paper, etc. Polymer materials commonly used include polyimide (PI), polyethylene terephthalate (PET), polyethylene naphthalate (PEN), thermoplastic polyurethane (TPU), and liquid crystal polymer (LCP). Polyimide is commonly used due to its ability to withstand very high temperatures [11] which are needed for many inks used

in inkjet and aerosol jet printing. PET is cheaper, but it cannot withstand as high of temperatures [12]. TPU is a hyperelastic material and works well in applications where stretchability is essential, but it also cannot handle high temperatures. LCP is a good choice for high speed applications due to its low loss and low moisture absorption [13], but has limited flexibility and stretchability.

There are many different categories of flexible electronics that are fabricated by printing. These include antennas [3, 4], conductors, inductors, sensors, capacitors [5, 14], batteries [15, 16], and many others. This thesis will be focusing specifically on inkjet-printed strain sensors and antennas.

Because these electronics are made with the intent of being deformed, work needs to be done to understand how their performance changes when stretched, bent, twisted, or otherwise deformed. Most tests that are conducted focus on stretching [17-19] or uniaxial bending [20-22]. There is also an ASTM testing standard for uniaxial mandrel bending of printed electronics [23]. Even though these tests provide useful information about the performance of these electronics, in actual applications, the flexible electronic systems undergo multiaxial deformation when conformed to complex surfaces. Because of this, tests need to be developed to test the reliability of these devices and their materials on such multiaxial surfaces. In this work, a test is developed for conforming flexible printed electronics to multiaxial surfaces such as a dome or saddle shape. This test is then used to test the performance or inkjet-printed flexible strain sensors and antennas and understand the behavior of their materials under this type of cyclic loading.

CHAPTER 2

OBJECTIVES AND SCOPE

Flexible electronics are used in many different applications, but there is not a thorough understanding of their electrical and mechanical performance when conformed to complex surfaces. Most of the existing studies focus on stretching, bending, folding, and other operations, and these bending and folding operations are typically done about one axis. Thus, there is significant gap in understanding the electrical and mechanical behavior of flexible electronic elements when bent or stretched over complex surfaces. Thus, the objective of this thesis is to study the mechanical and electrical performance of inkjet-printed silver ink elements conformed over complex sculptured surfaces. In particular, this thesis uses the following approach to achieve its objectives:

1. Fabricate strain sensors and antennas by inkjet printing silver nanoparticle ink onto various flexible polymer substrates. Two different silver inks are used on two different substrates: Polyethylene terephthalate (PET) and liquid crystal polymer (LCP).
2. Design and fabricate fixtures to be used to perform biaxial bending of flexible electronics over complex surfaces.
3. Test and monitor resistance of sensors and performance of antennas under monotonic and cyclic deformations.
4. Image ink structures using Scanning Electronic Microscopy (SEM) to investigate mechanical failure.
5. Perform finite-element simulations to examine stresses and strains in ink structures of sensors and antennas. Obtain mechanical properties of the ink through nanoindentation and from literature.

6. Relate the numerically-obtained strain distribution with DC resistance data obtained through experiments.
7. Identify locations of ink failure on the sensor and antenna through stresses obtained from finite-element simulations as well as through SEM images.
8. Provide an overall assessment of the performance of tested flexible substrates on complex surfaces.

CHAPTER 3

LITERATURE REVIEW

3.1 Printed Ink Characterization Techniques

Work has been done to understand the microstructure and mechanical properties of printed conductive inks used in flexible electronics. Mechanical properties such as Young's Modulus need to be obtained to create accurate material models to be used in structural simulations.

Various methods are used to obtain mechanical properties on thin metal films. One of the methods is to perform a tensile test on a free-standing thin metal film. There is an ASTM standard for tensile testing of thin metal films [24]. Unfortunately, there are issues with using this type of test to obtain mechanical properties of thin printed metal films. One issue was with the difficulty of printing and curing the metal films and then releasing it from the material that it was deposited on in order to obtain freestanding films. Attempts were made to print and cure the silver nanoparticle ink onto a sacrificial layer and then release it, but the film was difficult to handle and ultimately crumbled before being able to test. In addition, it has been shown that thin metal films on flexible polymer and elastomer substrates can undergo much higher strains that those that are freestanding [25, 26].

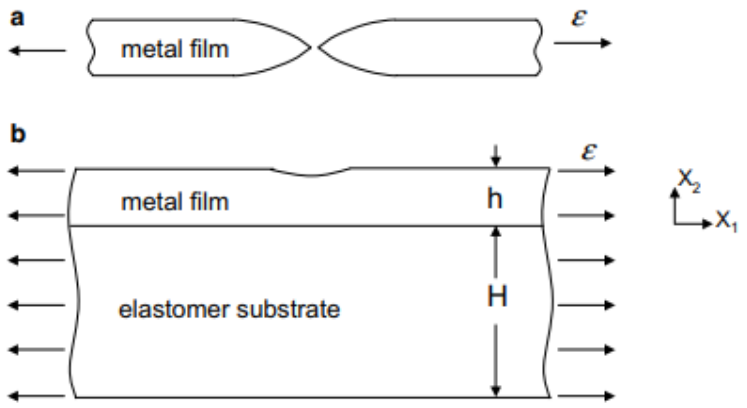

Figure 4: Straining of freestanding metal film vs. metal film on elastomer substrate [26]

Because of this, the strains at yield and fracture obtained from a tensile test will not reflect those seen by a printed metal film on polymer substrate used in a flexible electronic device.

An alternate method for obtaining the modulus of printed metal film is nanoindentation. This method eliminates the release and handling difficulties present in freestanding film tensile testing. This method has been used previously to obtain the modulus of silver nanoparticle ink films [27]. It is well known that the mechanical properties of a material changes with its porosity [28, 29]. Because the particle size distribution is different for different inks, and porosity changes with curing temperature and time, it is not accurate to use mechanical properties obtained for silver nanoparticle ink structures made from a different ink or different curing parameters.

3.2 Mechanical Tests

Multiple tests have been developed and used to investigate the performance of flexible electronics when deformed. Much of the work involves either stretching [30, 31]

or uniaxial bending [32, 33], but there has also been some involving twisting [34, 35]. Figure 5 shows an example of a stretching test [36] and Figure 6 shows a parallel plate bending test [20].

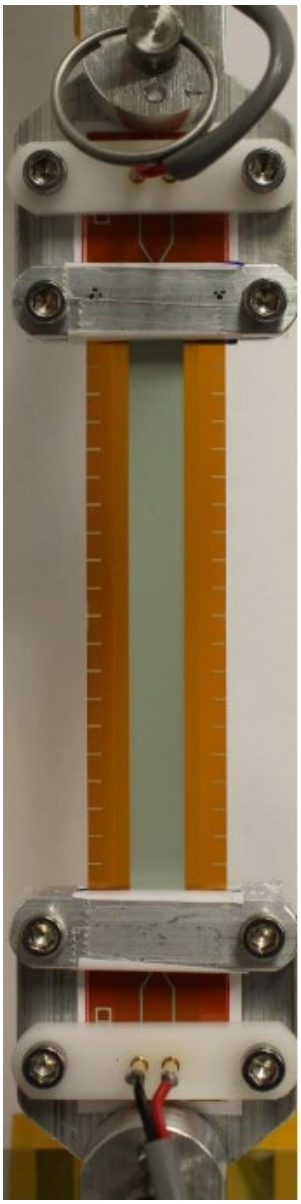

Figure 5: Uniaxial stretching test being used on silver ink printed on Kapton® [36]

Figure 6: Parallel plate bending test [20]

There is also an ASTM standard for a uniaxial bending test using mandrels [23]. This test method bends printed electronics to the radius of the chosen mandrel [23]. Figure 7 shows a schematic of this test method [23].

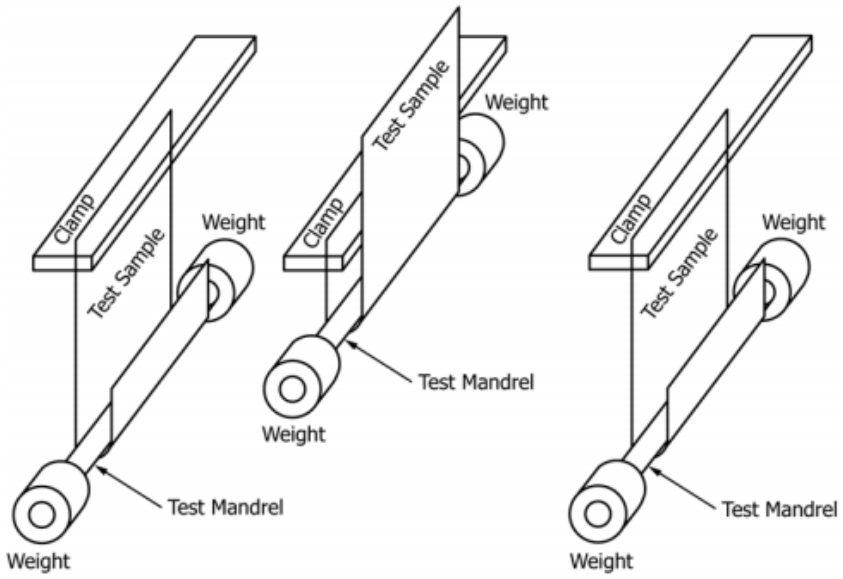

Figure 7: ASTM F2750-16 mandrel bending test [23]

Twisting tests can provide more complex loading than uniaxial tension or bending. For example the test setup used in Figure 8 has the sample clamped at both ends, and then one of the ends is twisted [35].

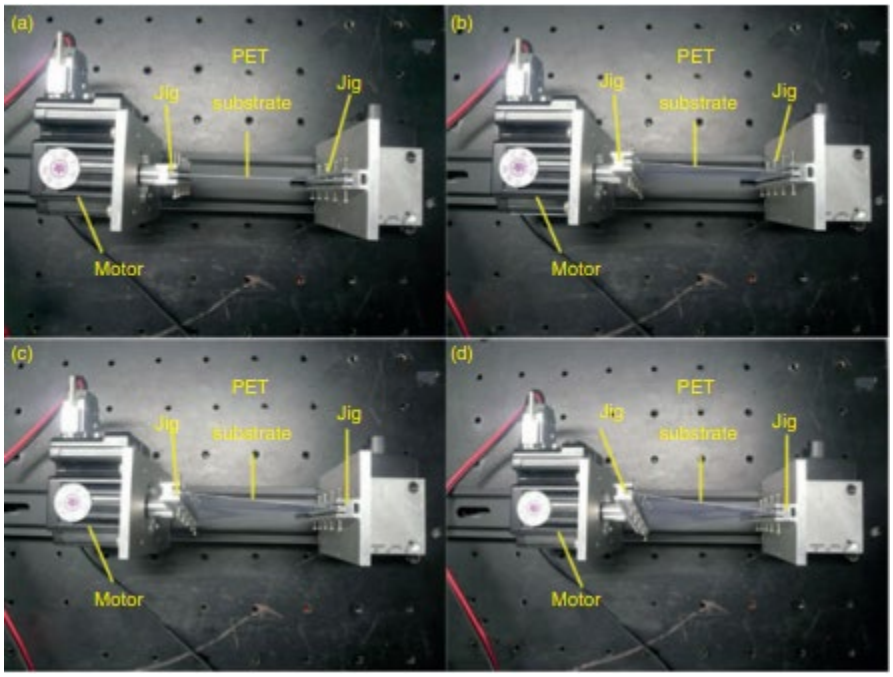

Figure 8: Example of twisting test setup for flexible electronics [35]

This type of test provides a twisting deformation to the sample as well as a tension load depending on how many degrees of rotation is applied.

Most of the mechanical tests used for flexible electronics test simple deformations (uniaxial stretching and bending). Even the more complex ones, such as twisting or even biaxial stretching, still may not capture the exact loading that a flexible electronic system will experience during use. It is therefore necessary to develop a test method for more complex loadings. This test method needs to be able to apply complex deformations seen

when flexible electronics are conformed to surfaces as well as be able to be adapted for many different surface geometries.

3.3 Effect of Strain on Electrical Performance

It is understood that the electrical resistance of a material increases with positive strain (tension) and decreases with negative strain (compression). The resistance of a conductor is given in (1).

$$R = \frac{\rho L}{A} \tag{1}$$

Where R is the electrical resistance, ρ is the resistivity of the material, L is the length of the conductor, and A is the cross sectional area of the conductor. Due to the Poisson effect, the cross sectional area decreases as the length increases. The ratio of the strained resistance with the final resistance is given in (2).

$$\frac{R}{R_0} = \frac{\frac{\rho L}{A}}{\frac{\rho L_0}{A_0}} = \frac{L}{L_0}\frac{A_0}{A} = \left(\frac{L}{L_0}\right)^2 \tag{2}$$

The type of ink used can affect the amount of strain that a printed silver conductor can undergo before losing conductivity. Screen printed silver flake in polymer matrix inks on stretchable substrates can undergo high strains while still being conductive [37, 38]. These types of inks on stretchable substrates can undergo many cycles at strains as high as 20% [37]. Silver nanoparticle inks used in inkjet and aerosol jet printed are not as stretchable as silver flake in polymer matrix inks. The reason for this is that cured structure is significantly different. These inks consist of silver nanoparticles dispersed in a fluid. After printing, the fluid evaporates off during the curing process and the particles fuse

together. This leaves a porous silver ink structure. Because the silver in these structures is not in a polymer matrix, it is easier to small cracks in the structure to develop [39].

3.4 Failure of Printed Ink Structures

Printed ink structures can fail in multiple ways. Physically, they can experience delamination or cracking. If the adhesion between the ink and substrate is not adequate, areas of the printed ink can flake off of the substrate. In addition, when the substrate is twisted, bent, or stretched, cracking can occur. Many times, a single deformation of the structure will change the electrical performance of printed structure, but when the structure returns to its original shape, the performance returns to normal. The failure usually occurs during many deformations. Because many of flexible electronics are used in situations where they are loaded repeatedly for many cycles (example: wearable sensors for human health monitoring), the fatigue life needs to be understood.

Previous work on understanding the effect of cyclic loading on the electrical and mechanical performance of printed silver nanoparticle ink structures has been done for uniaxial bending [39, 40] and stretching [19, 31]. Figure 9 shows an example of resistance results of a silver nanoparticle ink structure subjected to cyclic tensile loading at 1% and 2% strain from O. Glushko, A. Klug, E.J.W. List-Kratochvil, and M.J. Cordill [31].

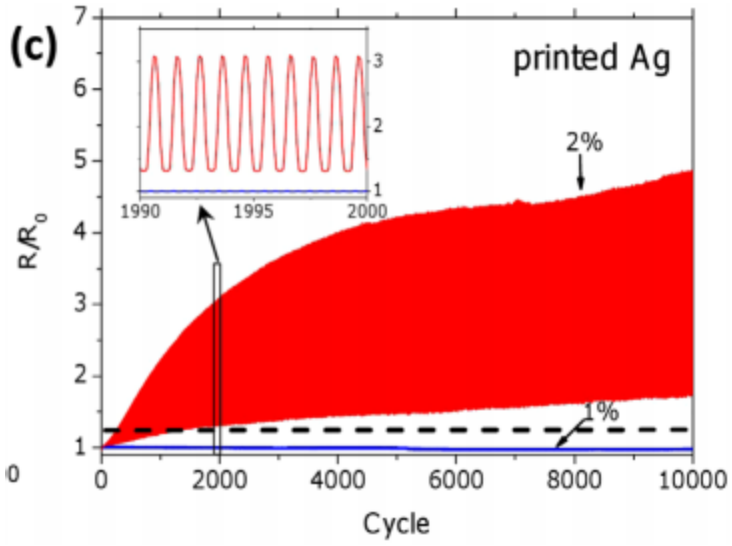

Figure 9: Electrical resistance of printed silver nanoparticle ink structure subjected to 1% and 2% cyclic tensile strain [31]

Similarly, a graph of the electrical resistance of another silver nanoparticle ink structure subjected to cyclic uniaxial bending is shown in Figure 10 from Quintero et al. [40].

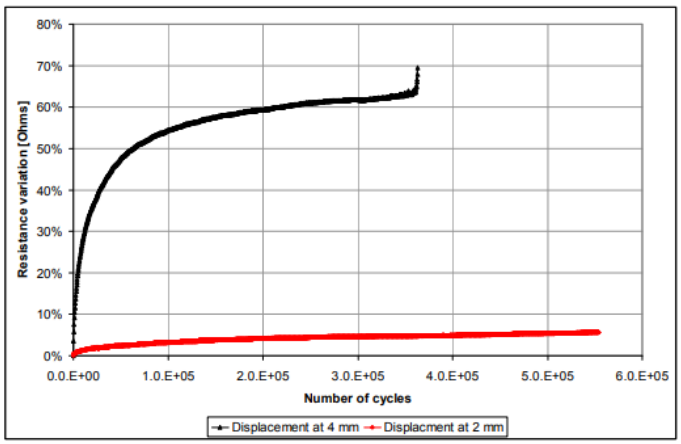

Figure 10: Electrical resistance of printed silver nanoparticle ink structure subjected to uniaxial bending [40]

The increase in resistance during cycling is due to the creation of cracks and their propagation over many cycles. Many times there will be many of these cracks visible on the structure and they propagate in a jagged direction. Figure 11 shows an SEM image of cracking in an inkjet-printed silver nanoparticle ink structure during cyclic tensile testing from Glushko et al. [31].

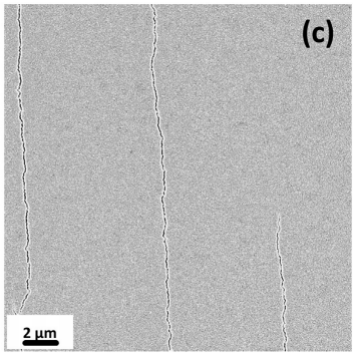

Figure 11: SEM image of cracking in silver nanoparticle ink structure after tensile fatigue testing [31]

CHAPTER 4

FABRICATION OF SENSORS AND ANTENNAS

Strain sensors and antennas were fabricated using a variety of inks, substrates, and curing methods. Liquid crystal polymer (LCP) and polyethylene terephthalate (PET) were used as substrates and two different silver nanoparticle inks were used as conductors. The inks were deposited using inkjet printing and both air drying and oven curing of the inks were utilized.

4.1 Fabrication of Strain Sensor

The strain sensor utilized a serpentine pattern with six parallel lines. Four pads were placed on one side to facilitate four-point measurement. The four-point pads are located sufficiently away from the strain sensor lines so that the pads are outside the fixtures. The CAD model of the strain sensor with dimensions is shown in Figure 12.

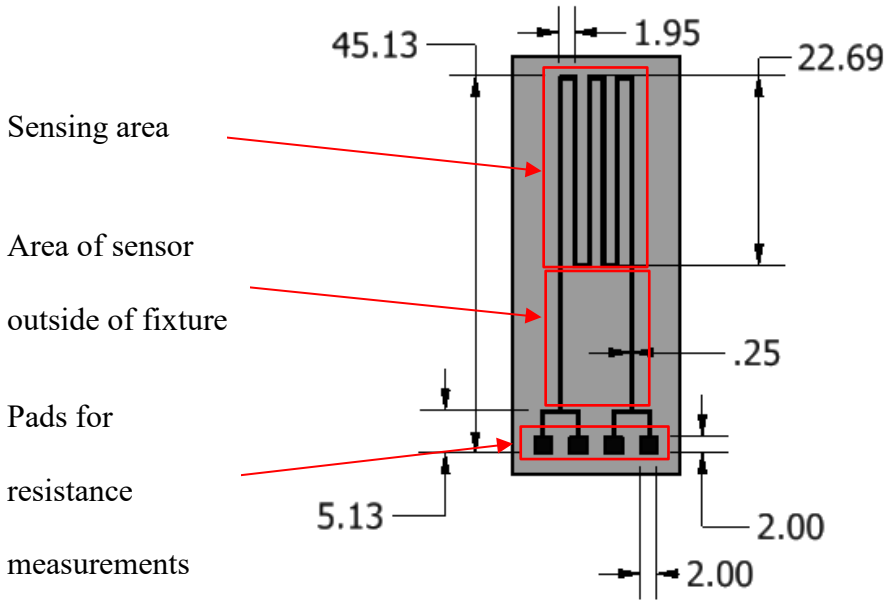

Figure 12: Strain Sensor Design (dimensions in millimeters)

The first set of sensors were fabricated by inkjet printing silver ink using an Epson® Stylus® C88+ desktop printer. This normal desktop printer made for printing documents was altered by replacing the normal ink cartridges with ones filled with Novacentrix® Metalon® JS-B25P silver ink.

The ink used is made to be suitable for use with desktop Epson® printers [41]. It is a water-based ink with a 25% by weight silver content [41]. The substrate chosen for this ink was Novele™ IJ-220, a microporous coated PET. The thickness of this substrate was 140 µm [42]. The coating helps with particle-to-particle contact of the printed ink. The silver particles in the ink have a capping agent to help with controlling particle size and to prevent clumping of the particles in the ink. When the ink is printed, the coating helps move the capping agent off the particles so they come into contact and become

electrically conductive. This makes it possible to have electrically conductive ink patterns without thermal curing. Therefore, the first set of sensors was allowed to dry in the ambient air for several hours before testing the electrical resistance. Table 1 below shows the resistance of five different samples dried in the air.

Table 1: Resistance of strain sensor made with Novacentrix® Metalon® JS-B25P ink on Novele™ IJ-220 PET dried in the air

Sample	**Resistance (Ω)**
1	302.6
2	301.6
3	377.2
4	299.8
5	309.2
Average	314.7

Even though the ink is conductive after drying at room temperature, the electrical resistance can be decreased by oven curing. Therefore, for the second set of samples, the printed patterns were cured in an oven at 90°C for 30 minutes. This temperature was chosen because it was suggested not to heat up the PET over 100 °C. The oven curing had a beneficial impact on the resistance of the silver ink, and the resistance dropped by 53%

compared to air-dried samples. Another method of curing the Novacentrix™ ink on PET would be to use photonic curing. This method uses a flashing light to cure the silver while happening fast enough that the substrate does not heat up substantially. This alternative could lead to even further curing without worrying about damage to the substrate. Photonic curing is not used in this work, but would be a useful method to explore. Table 2 below shows the resistances of five air dried and five oven cured samples.

Table 2: Resistance of strain sensor made with Novacentrix® Metalon® JS-B25P ink on Novele™ IJ-220 PET cured in oven at 90°C for 30 minutes

Sample	Resistance (Ω)
6	167.0
7	167.3
8	128.5
9	135.7
10	146.0
Average	148.9

Although the thermally-cured samples showed lower resistance, the samples warped compressing the ink structures as shown in Figure 13.

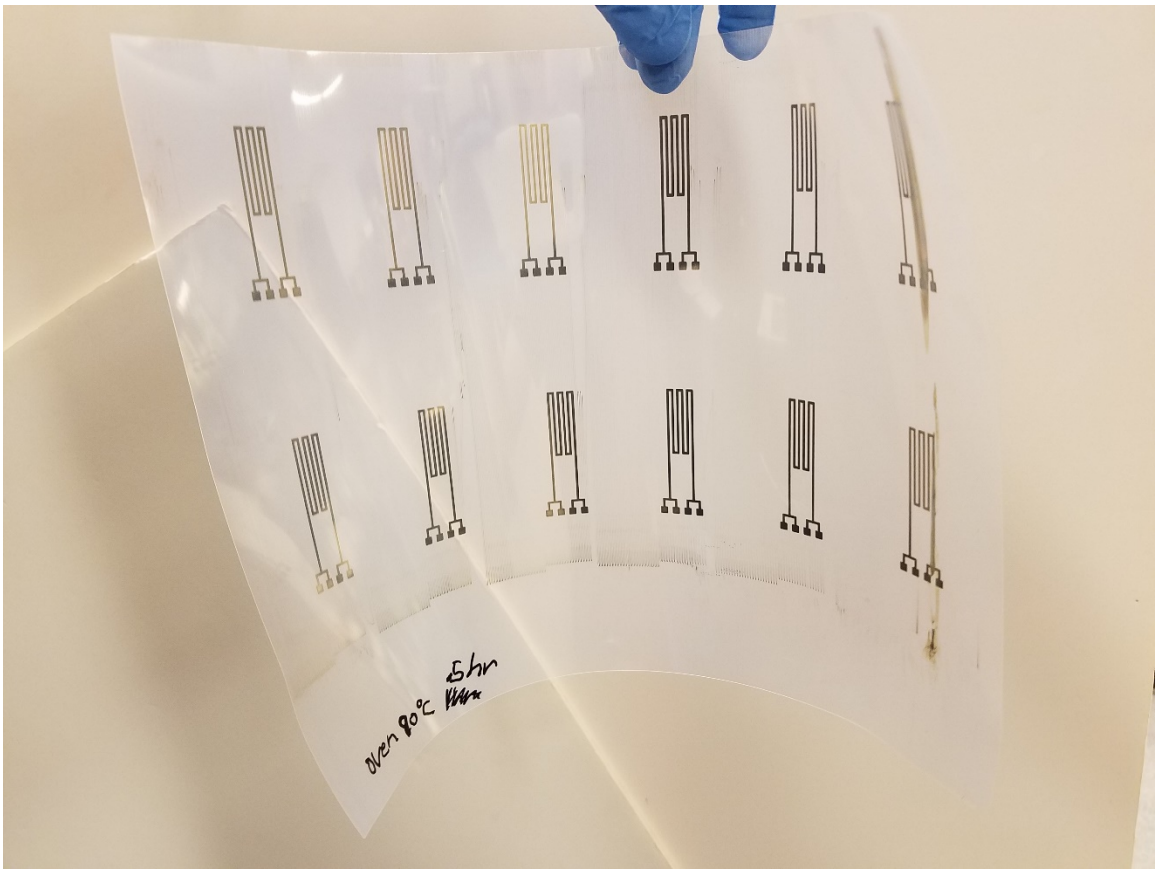

Figure 13: Warped sheet of oven cured Novacentrix® Metalon® JS-B25P ink strain sensors on Novele™ IJ-220 PET

The third set of sensors were fabricated at the Athena Lab at Georgia Tech using a Fujifilm Dimatix™ 2831 inkjet printer. This printer was expected to have better results due to it being designed for printing electronics.

The ink used with the Dimatix™ 2831 printer was the Sun Chemical® Suntronic™ EMD 5730 silver ink. This is a solvent-based silver nanoparticle ink with a 40% silver content [43]. This ink has a significantly higher silver content than the Novacentrix® Metalon® JS-B25P ink. Also, the viscosity of the ink is 10-13 cPs [43] which is

significantly higher than the 3-5 cP for the Novacentrix® Metalon® JS-B25P ink [41] that is used in a normal desktop printer.

The ink was printed onto 177.8 μm thick (7 mil) Rogers Ultralam® 3850HT LCP. Because the substrate remains stationary while the print head moves, it was possible to apply multiple layers of ink in the same spots. In order to obtain better electrical performance, four layers ink were printed on top of each other in the strain sensor pattern. Because of the substrate being fed from the top through the printer and out of the front with the Epson printer, it was not possible to print multiple layers of ink on the PET samples. After printing the LCP samples, they were cured in an oven at 200°C for 30 minutes. This curing method was chosen due to recommendations of researchers who had been using the ink before. This temperature and time also fits in the range given by Sun Chemical® [43]. Figure 14 shows some of these printed sensors on LCP after curing and trimming.

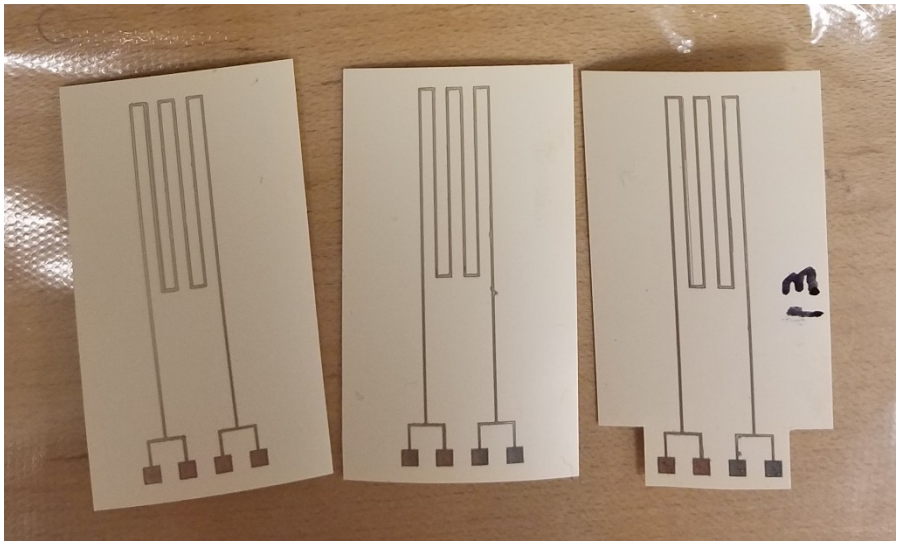

Figure 14: Sensors made with Sun Chemical® Suntronic™ EMD 5730 ink on Rogers Ultralam® 3850HT LCP

Initial resistance values of five different Sun Chemical® Suntronic™ EMD 5730 ink samples are shown in Table 3.

Table 3: Resistance of strain sensors made with Sun Chemical® Suntronic™ EMD 5730 ink on Rogers Ultralam® 3850HT LCP cured in oven at 200°C for 30 minutes

Sample	Resistance (Ω)
1	19.55
2	30.91
3	21.88
4	26.37
5	24.06
Average	24.55

All of the samples printed with the Epson® printer had only one layer of ink. Depositing multiple layers of ink on top of each other was attempted, but was not successful. Because the PET had to be removed from the bottom and fed back through the top and also because the feeder was not extremely consistent, it was difficult to make the patterns from multiple passes line up. When multiple passes were performed, the patterns were in the same general area, but still did not layer perfectly on top of each other.

One can see that the resistances of the sensors made with the Sun Chemical® Suntronic™ EMD 5730 ink are significantly lower than those made with the Novacentrix®

Metalon® JS-B25P ink. This is most likely due to having printed multiple layers on top of each other, not having the ink in a porous coating, and the higher cure temperature. Figure 15 shows one of these printed sensors with Sun Chemical® Suntronic™ EMD 5730 on Rogers Ultralam® 3850HT LCP while Figure 16 shows a sensor made with Novacentrix® Metalon® JS-B25P ink on Novele™ IJ-220 PET cured in the oven.

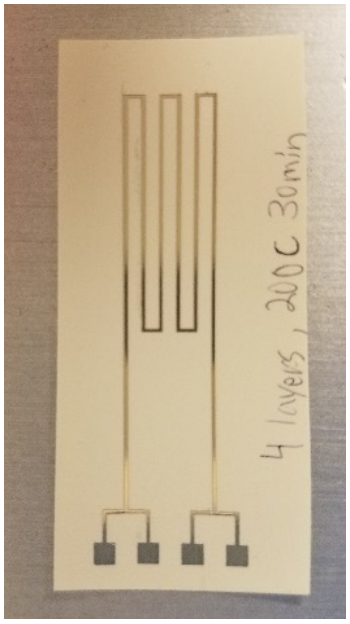

Figure 15: Sensor made with Sun Chemical® Suntronic™ EMD 5730 ink on Rogers Ultralam® 3850HT LCP

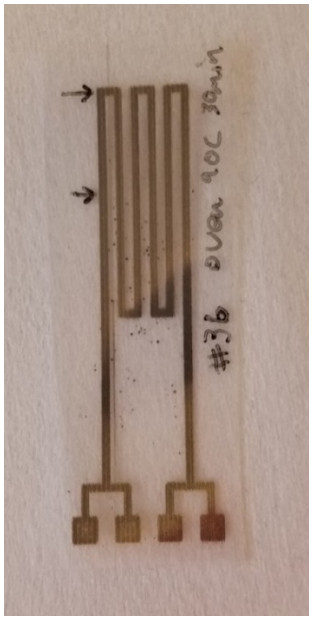

Figure 16: Sensor made with Novacentrix® Metalon® JS-B25P ink on Novele™ IJ-220 PET

4.2 Fabrication of Circular Patch-Array Antenna

The antenna was designed in a collaborative effort between Georgia Tech and Boeing. The antenna was intended to operate at 10 GHz. It was designed to be low cost, flexible, and low profile. The design was a circular patch array type. As the fabrication

process matured, the size of the array was moved from a 2x2 to a 4x4 and then to an 8x8. The antenna was fabricated at the Athena Lab at Georgia Tech using silver ink as the conductor, copper for the ground plane, and flexible polymers for the dielectric layers. Figure 17 shows an image of the various antenna layers. The middle copper conductor layer was used initially, but was later removed when a soldered end launch connector was switched out for a clamping type.

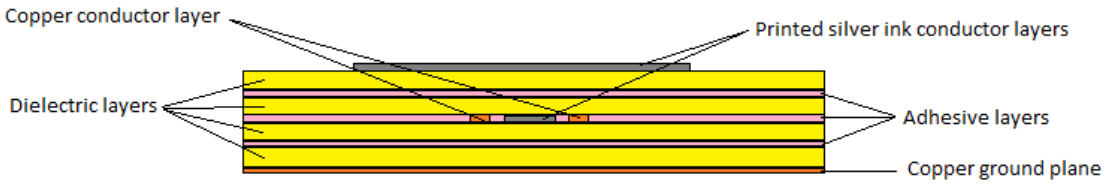

Figure 17: Antenna layers stackup

Figure 18 and Figure 19 show the top and middle printed ink layer designs.

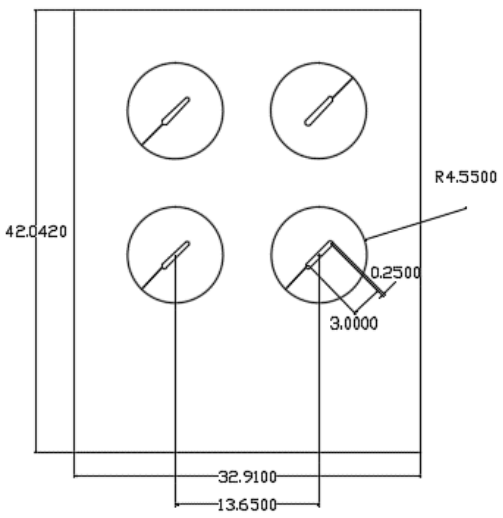

Figure 18: 2x2 antenna top ink layer

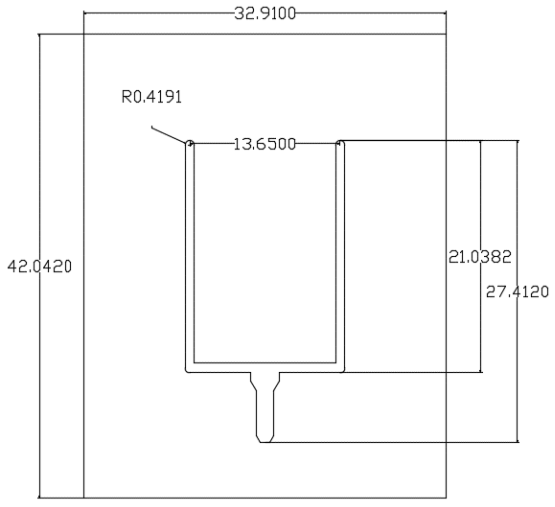

Figure 19: 2x2 antenna middle ink layer

The materials chosen were Rogers Ultralam® 3850HT LCP for the dielectric layers, Sun Chemical® Suntronic™ EMD 5730 for the silver ink layers, and copper for the ground plane. The layers were bonded together using 3M 966 adhesive transfer tape. The dielectric layers were each 177.8 µm thick, the copper was 17.78 µm, and the ink 5 µm.

The middle and top ink layers were fabricated by inkjet printing of the silver ink onto the LCP using the Dimatix™ 2831 printer. These layers of LCP were then cured in an oven at 200°C for 30 minutes. Figure 20 shows the two ink and middle bare LCP layers of a 2x2 antenna after curing and trimming.

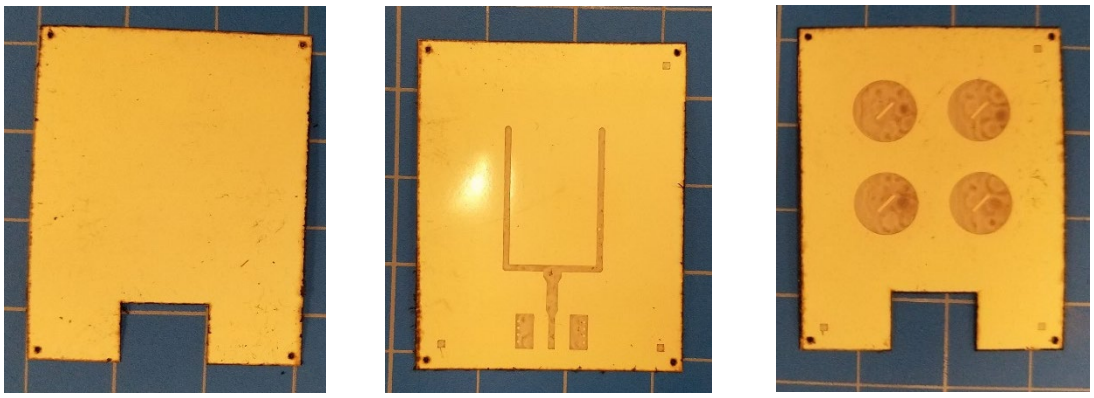

Figure 20: Left to right: bare middle dielectric layer, middle ink layer, and top ink layer of 2x2 Rogers Ultralam® 3850HT LCP antenna after curing and trimming

The layers were bonded together with the transfer tape at room temperature. The final assembled 2x2 antenna is shown in Figure 21 without the connector attached. After assembly, this antenna was flexible enough to easily bend with one's hand, which can be seen in Figure 22.

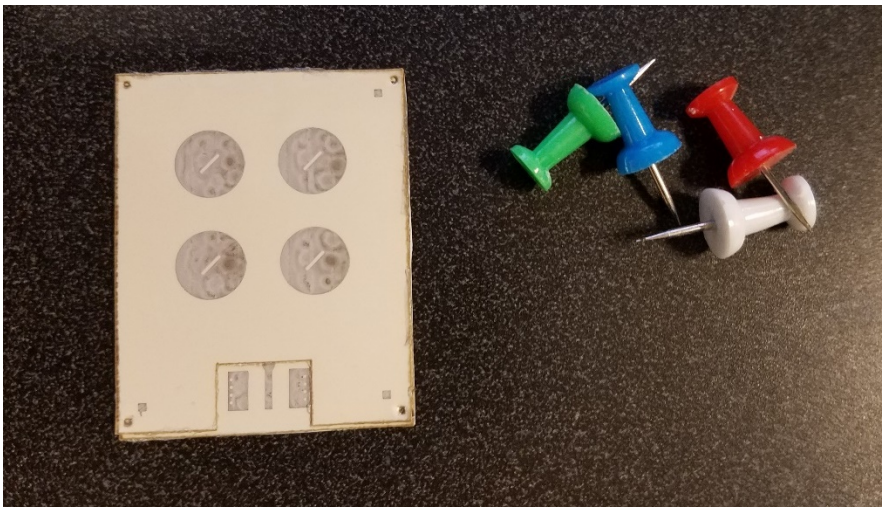

Figure 21: Assembled 2x2 Rogers Ultralam® 3850HT LCP antenna

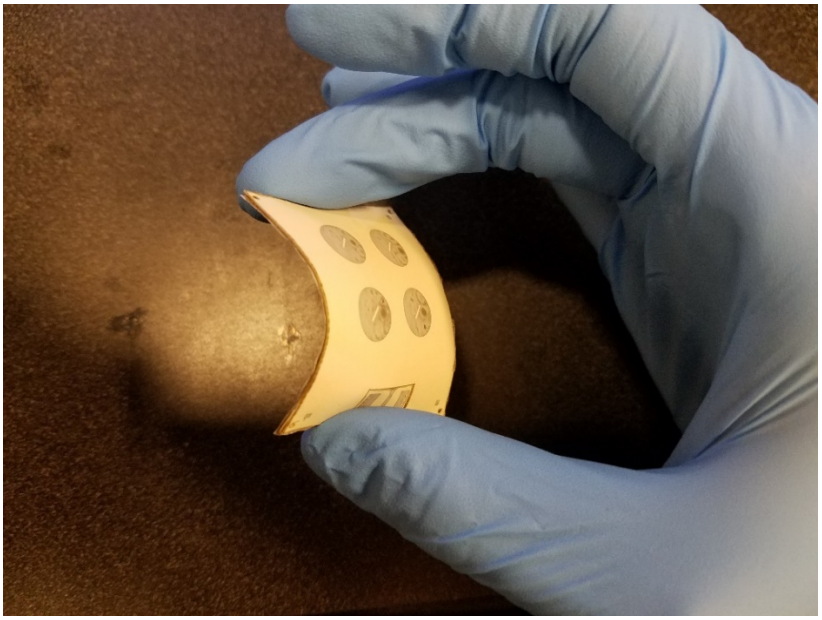

Figure 22: Flexing of 2x2 Rogers Ultralam® 3850HT LCP antenna

The final ink layer thickness was 5 μm. The antenna did not show significant warpage after the bonding process was complete. A Southwest® end-launch connector was then attached by cutting two holes for the screws at the end of the antenna near the connection point and then hand tightening the screws until the connector was snug.

An encapsulation layer was added to the top of the antenna to protect against damage from scraping or scratching and also for environmental protection. The encapsulation layers was added using a roll to roll slot-die coater. DuPont™ Elvax® 250 EVA was the material applied. After application, the encapsulation was cured at 120°C for three hours. After curing, the final thickness of the coating was 80 µm. Figure 23 shows a picture of the roll to roll slot-die coating setup and Figure 24 shows a 4x4 Pyralux® polyimide antenna under the coater.

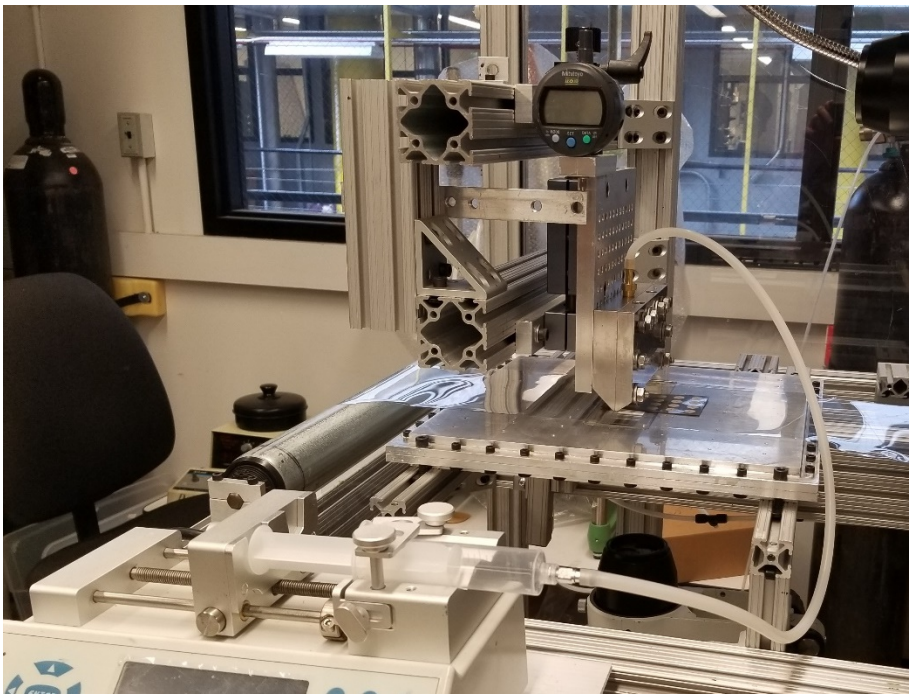

Figure 23: Slot-die coater setup

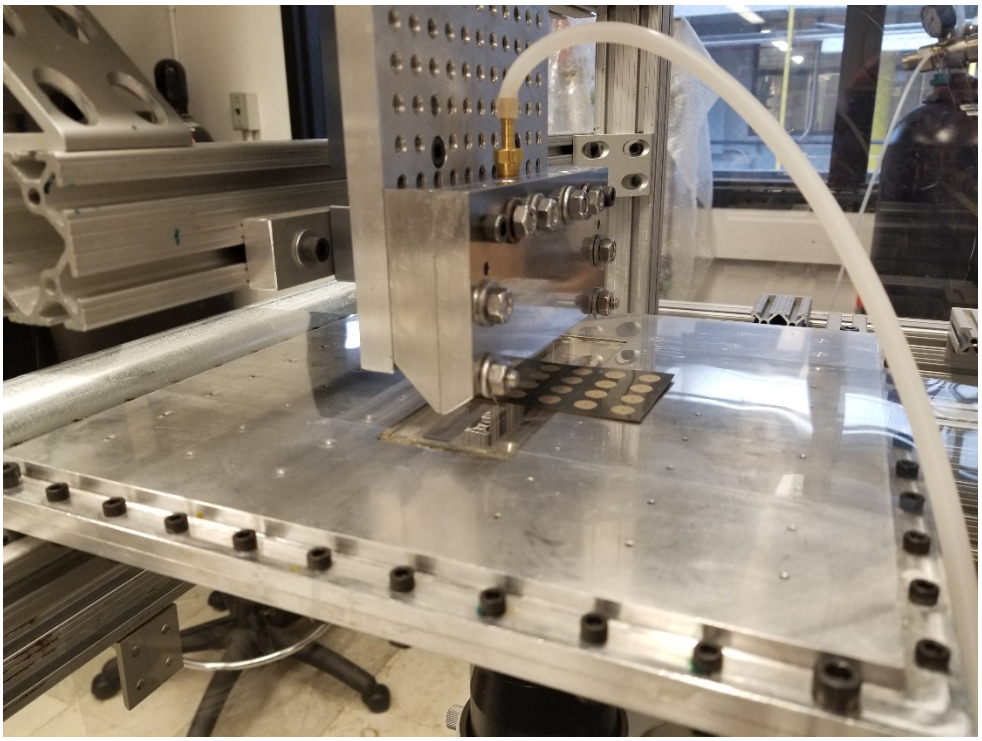

Figure 24: 4x4 Pyralux® polyimide antenna under slot-die coater

In addition to the LCP antenna fabricated at Georgia Tech, a similar antenna was fabricated by Boeing using different materials. The stack up of the antenna is like that shown in Figure 17, but the layers have different heights. The conductor layer designs on the antenna were the same as those used by Georgia Tech as well. For the dielectric layers, 254 μm (10 mil) Pyralux® polyimide was used. The ink used for the conductor layers was DuPont CB028 and it was dispensed using an nScrypt system. The layers were bonded together using the same 3M 966 adhesive transfer tape that was used with the LCP antennas. Figure 25 shows a 4x4 polyimide antenna.

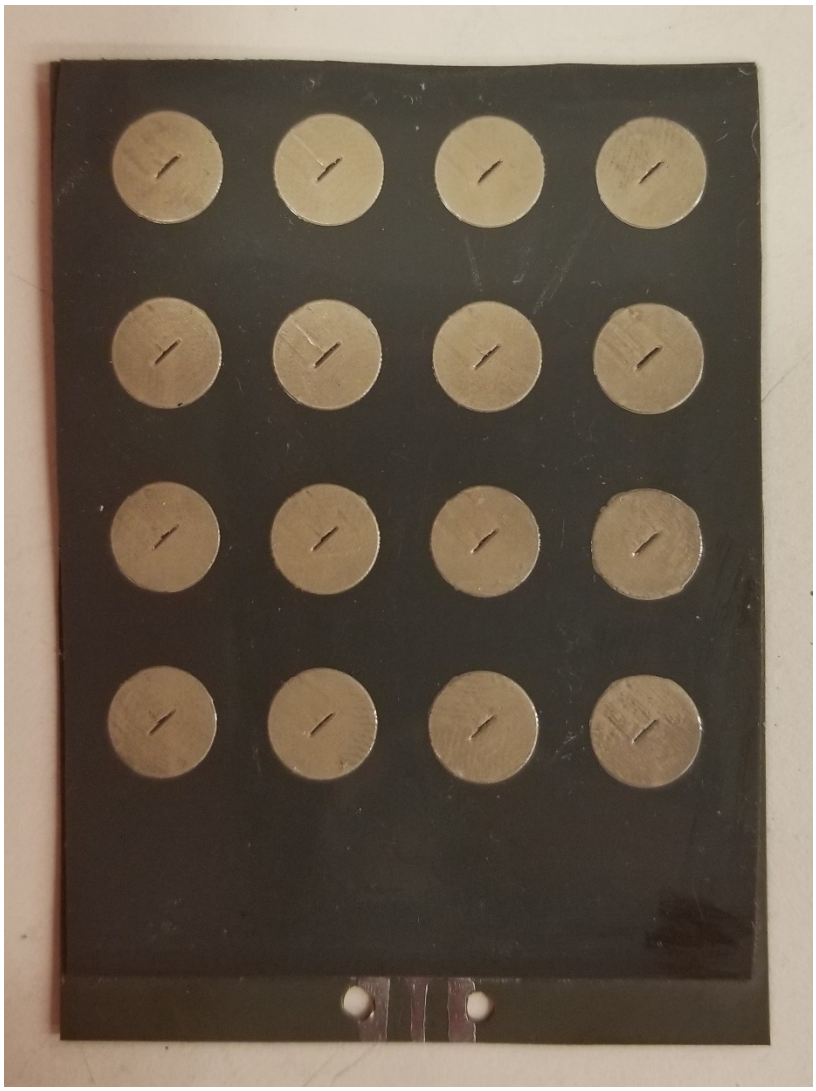

Figure 25: 4x4 Pyralux® polyimide antenna

The ink layers on the polyimide antennas were about 30 μm thick, about six times that of the ink layers on the LCP antennas. In addition, the entire thickness was much greater as well due to the dielectric layers being 254 μm thick compared to the 177.8 μm thick LCP dielectric layers. When bending the antenna by hand, one could tell that the Pyralux® antenna was significantly less flexible.

In order to compare the performance of silver ink to copper as a conductor material for antennas, an 8x8 antenna was fabricated with copper alongside the ink antenna. This copper antenna used the same dielectric layers and adhesive as the LCP antennas, but the copper patterns were fabricated by wet etching. The same thickness LCP clad with one half ounce copper was used in this etching process. The thickness of the copper conductor layers were 17.78 μm. Figure 26 shows an assembled 8x8 copper antenna.

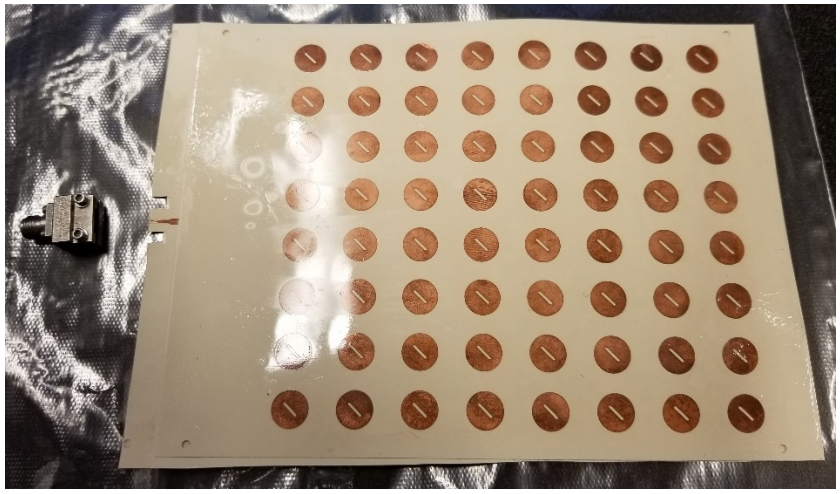

Figure 26: 8x8 copper Rogers Ultralam® 3850HT LCP antenna

CHAPTER 5

DESIGN AND FABRICATION OF BIAXIAL MECHANICAL TESTING FIXTURES

5.1 Design of Sculptured Surface Fixtures

A two-part fixture system was designed to conform the electronics to the desired shapes. These fixtures were designed with matching surfaces where the two would press together with the sample in between. When the fixtures were pushed together, it would force the sample to conform to the surface shape. In addition, mounting areas were designed into the fixtures to use for attaching them to a Test Resources™ 100 universal test machine (UTM). Figure 27 and Figure 28 show CAD models of the two matching four-inch radius saddle and dome fixture sets. For the fixtures that did not have flat edges, such as the dome, a cutout was made on each of the two fixtures to give a flat edge where the entire sample would be covered by the fixture.

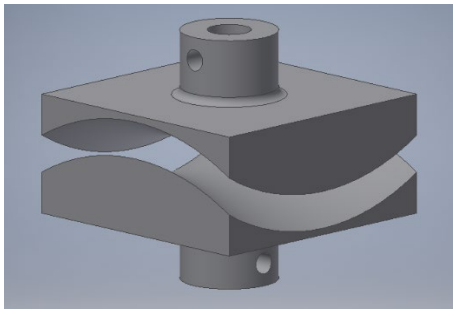

Figure 27: 4 in. radius saddle-like bend fixtures

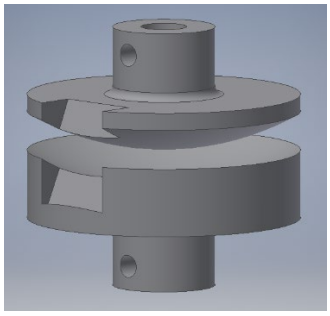

Figure 28: 4 in. radius dome bend fixtures

5.2 Sculptured Surfaces

Table 4 shows the dimensions and geometry of various fixtures fabricated, and the type of sample tested with that fixture. As seen, most of the radii used in this study are much larger than the thickness of the substrate, and these radii were chosen to represent selected segments of various aircraft structures.

Table 4: Surfaces used in testing the sensors and antennas

Fixture Geometry	Fixture Dimensions	Type of Sample Tested
Dome (spherical)	4 in. (101.6 mm) radius	Strain Sensor
Saddle-Like (convex and concave)	4 in. (101.6 mm) radius in convex and concave directions	Strain Sensor
Barrel-like shape	4 in. (101.6 mm) radius swept on a 40 in. (1016 mm) radius	Antenna
Saddle-like shape	4 in. (101.6 mm) radius swept on a 40 in. (1016 mm) radius	Antenna

Figure 29 shows the CAD models of the surfaces used in fabricating the test fixtures.

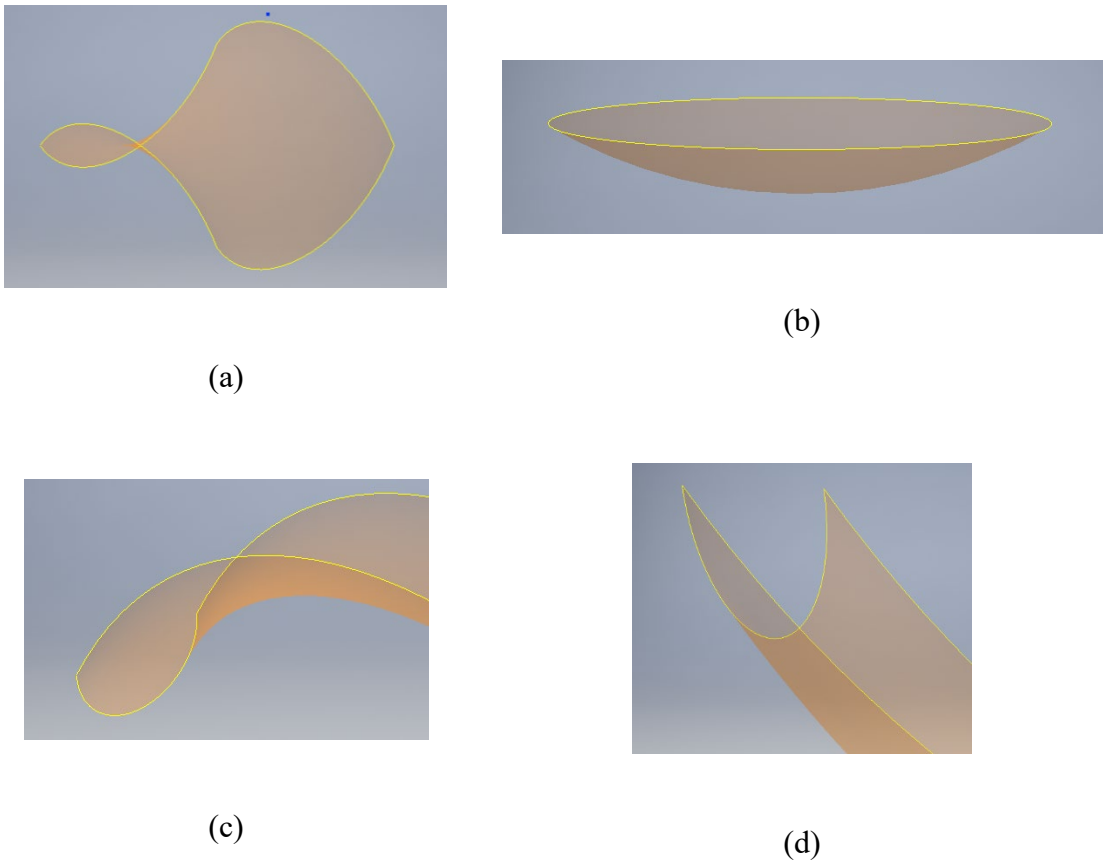

(a)

(b)

(c)

(d)

Figure 29: CAD models of surfaces used in test fixtures. (a) 4 in. saddle-like surface, (b) 4 in. dome surface, (c) 4x40 in. saddle-like surface, (d) 4x40 in. barrel-like surface

Test fixtures and attachments needed to be fabricated in order to physically test the printed sensors and antennas on complex curved surfaces. The two types of surfaces that were tested were dome and saddle shapes. For each of these types, surfaces were made

with equal and differing radii of curvature in the two bend directions. With differing radii of curvature, one of the directions of the saddle bend is much tighter than the other and the dome shape becomes a barrel-like surface. The surfaces utilizing differing radii of curvature used a 10:1 ratio for the radii. The surfaces with equal radii of curvature were made to be used with the sensors, while the ones with differing radii of curvature were used for the bending of the antenna. This was due to finding it very difficult to make the antenna conform to the surfaces with equal radii of curvature.

5.3 Fabrication of Sculptured Surface Fixtures

The fixtures were fabricated using an Ultimaker 2+ 3D printer. The material used to make the fixtures was Polylactic Acid (PLA). Figure 30 shows the 3D printed fixtures with equal radii of curvatures.

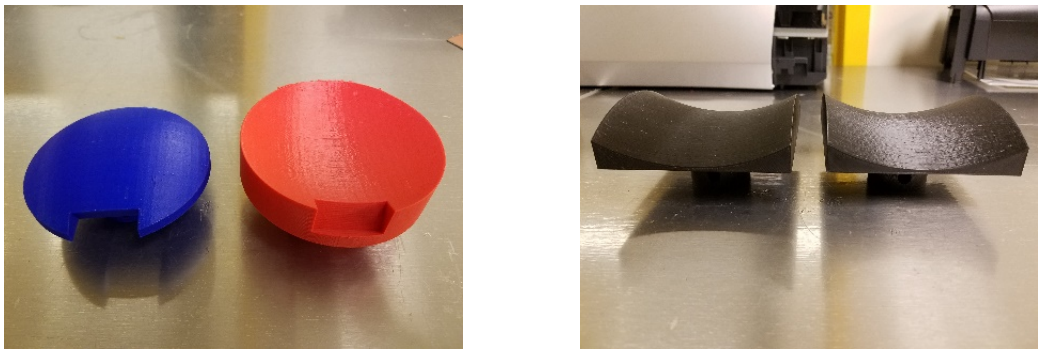

Figure 30: 3D printed fixtures of 4 in. dome (left) and 4 in. saddle-like (right) surfaces

Figure 31 shows the fixtures with the 10:1 ratio radii of curvature.

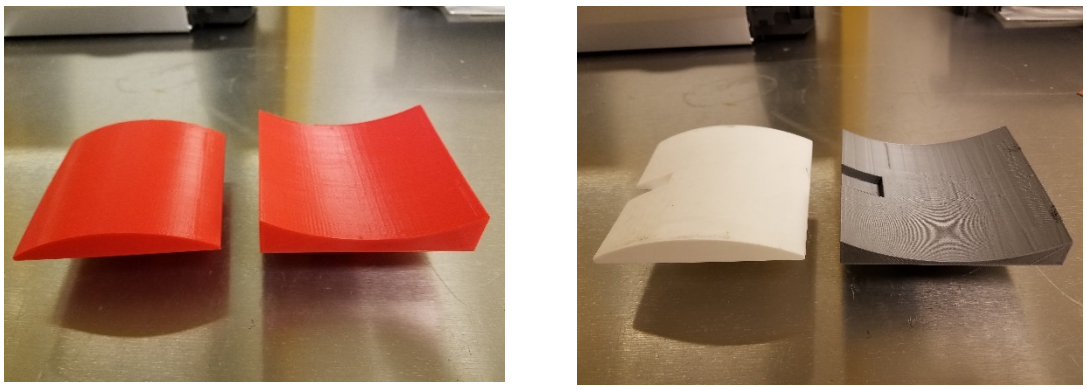

Figure 31: 3D printed fixtures of 4x40 in. barrel-like (left) and 4x40 in. saddle-like (right) surfaces

For testing the 8x8 antennas, larger fixtures had to be designed for the entire area of the antenna to be conformed to the surface. The same radii of curvatures were used for these larger fixtures. Figure 32 shows the larger 4x40 in. saddle-like fixtures and Figure 33 shows the larger 4x40 in. barrel-like fixtures.

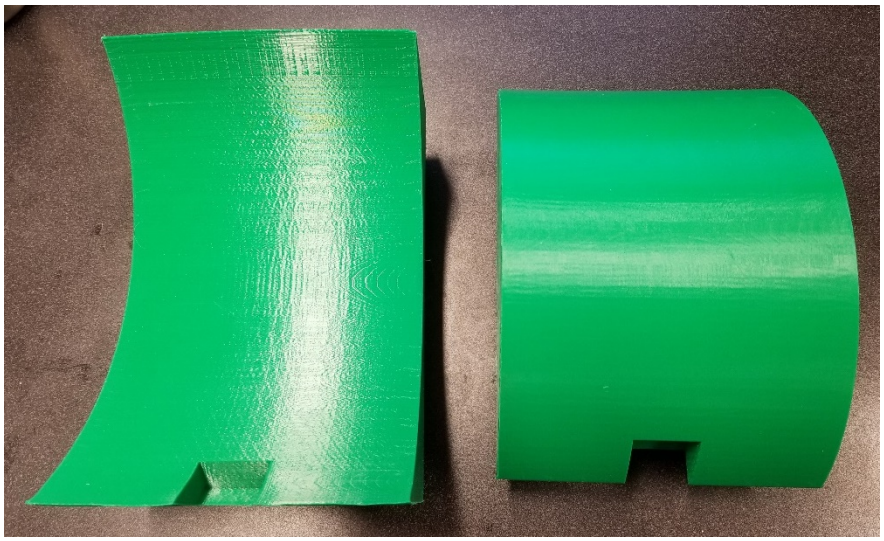

Figure 32: 4x40 in. saddle-like fixtures for 8x8 antennas

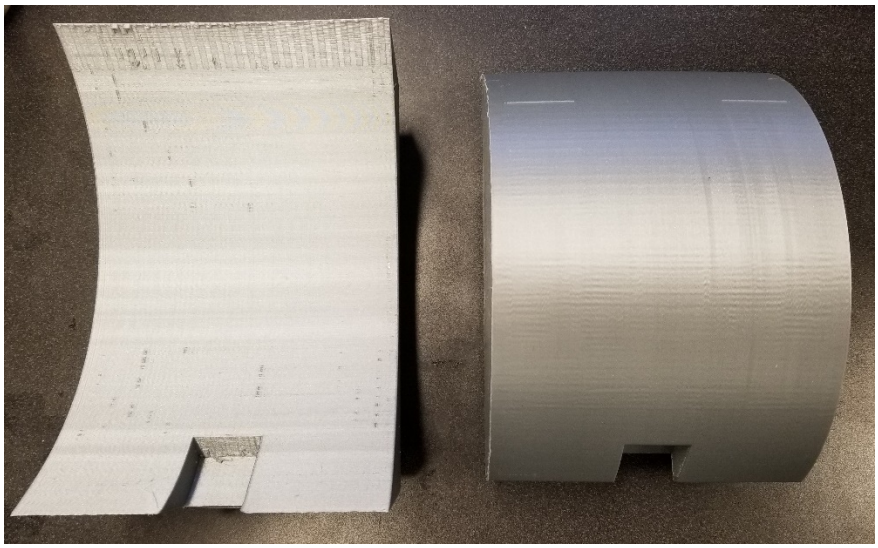

Figure 33: 4x40 in. barrel-like fixtures for 8x8 antennas

To perform the tests, the fixtures were fastened to the universal test machine. The bottom fixture remained stationary while the top fixture moved vertically. The 4 in. saddle-like bend fixtures are shown attached to the UTM in Figure 34.

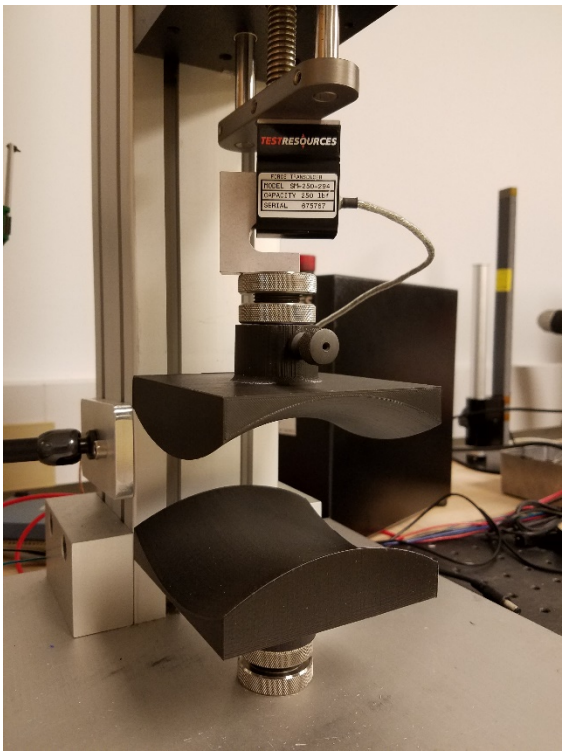

Figure 34: 4 in. saddle-like fixtures on Test Resources™ 100 UTM

CHAPTER 6

BIAXIAL MECHANICAL TESTING OF SENSOR SAMPLES

6.1 Connection to the Sample

A pogo pin fixture was fabricated in order to facilitate easy measurements of the sensors during testing. This fixture consists of four pogo pins glued into a top holder and a bottom piece with a flat surface. Screws were placed in two outer holes on the top piece and screwed into threaded holes on the bottom piece. The sensor was placed in between the two pieces and the screws were tightened. As the screws were threaded through the bottom piece, the pogo pins clamped down onto the pads of the sensor. Figure 35 shows a sensor on LCP with the pogo pin fixture attached.

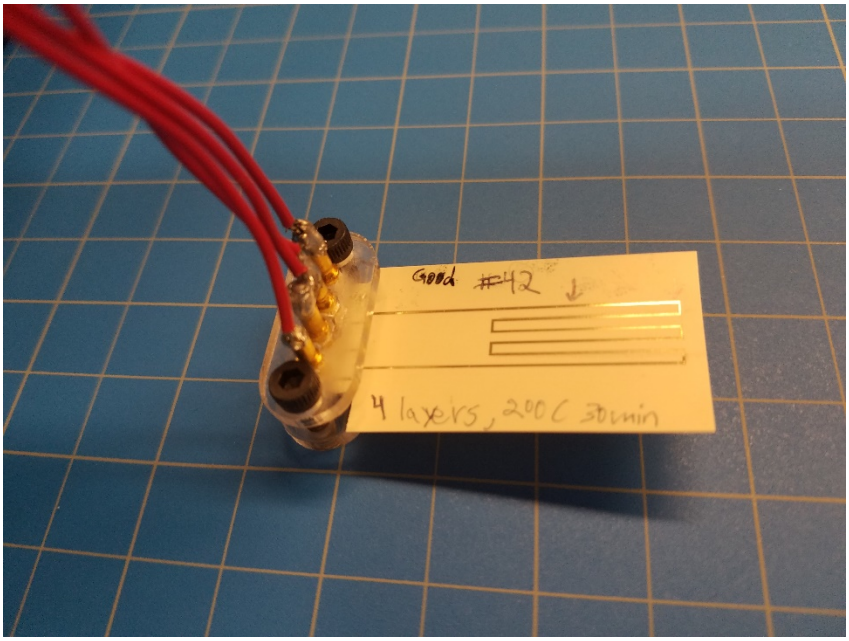

Figure 35: LCP sensor with pogo pin connector attached

6.2 Sensor Testing Setup

To test the sensors, the pogo pin connector was first attached to the pads as shown in Figure 35 and then attached to the fixtures on the UTS as shown in Figure 36. Soft wipes were placed under and on top of the sample to prevent the fixtures from scraping the sample. A few small pieces of tape were attached to the bottom side of the pogo pin connector and the bottom fixtures in order to keep the sample in place.

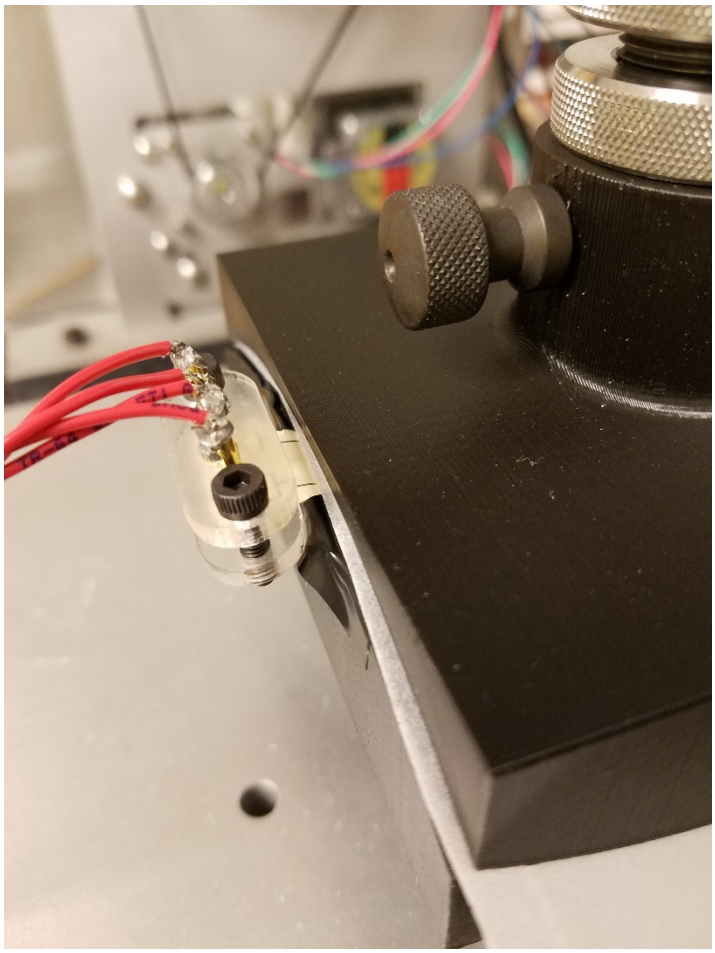

Figure 36: LCP sensor in 4 in. saddle-like fixtures

Figure 37 shows the sensor in the dome fixture where the pogo pin connector is in the cutout area.

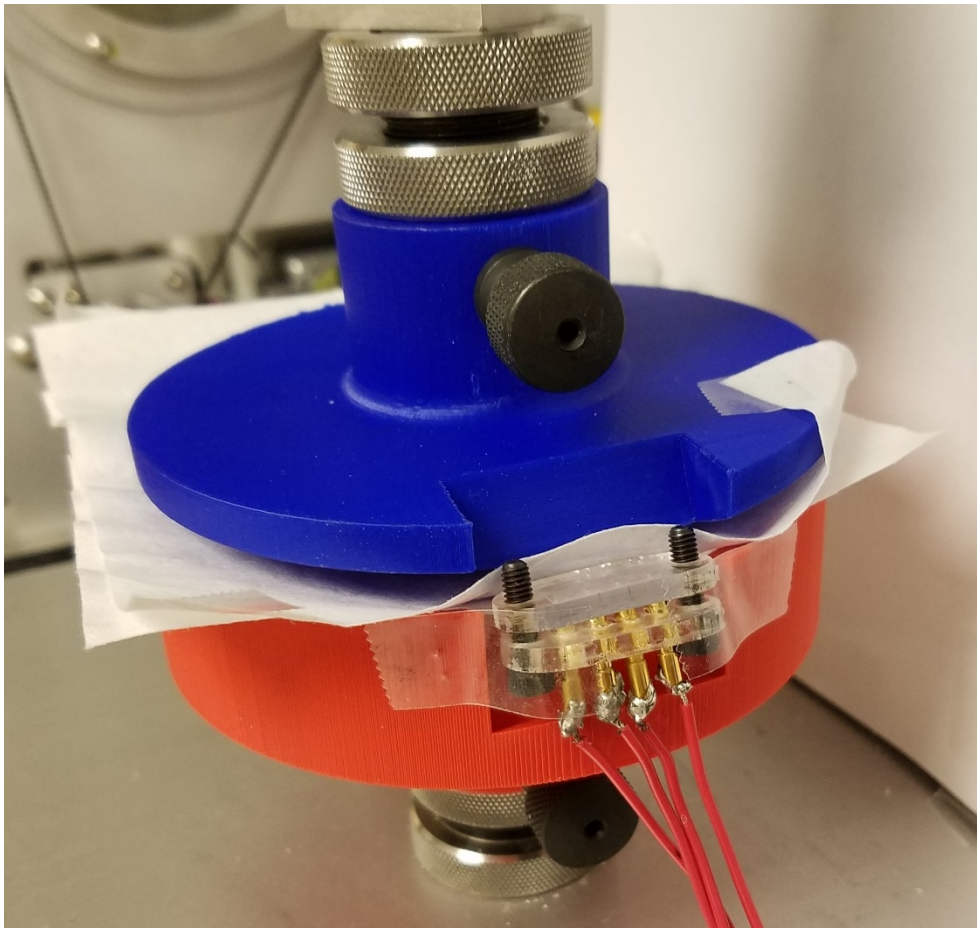

Figure 37: Sensor in 4 in. dome fixtures

The full setup with the sensor in place with wires attached to multimeter can be seen in Figure 38.

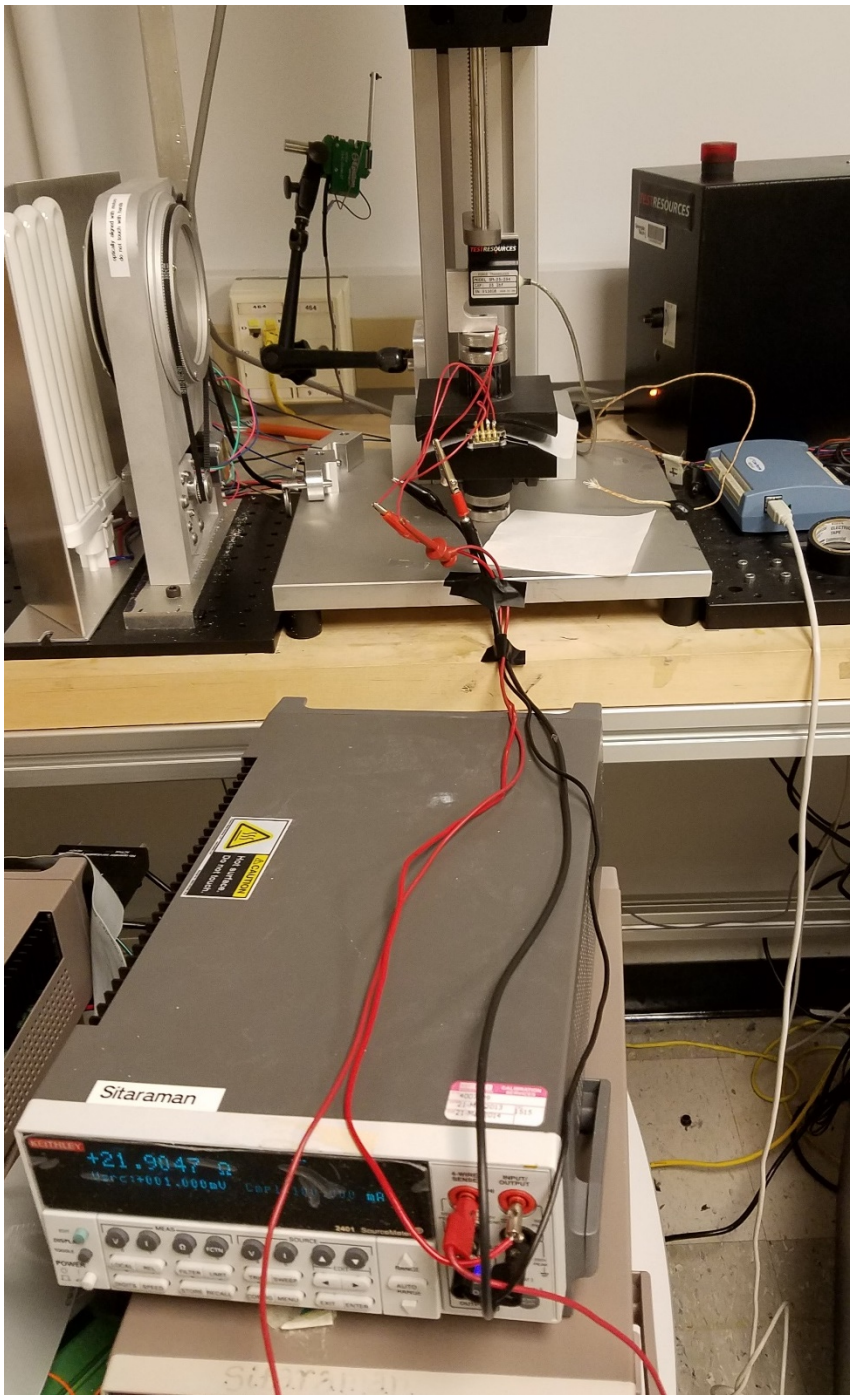

Figure 38: Full setup of LCP sensor in 4 in. saddle-like fixtures with multimeter

The sample with the pogo pin connector was first placed on the bottom fixture and held in place with a tape. The top fixture was at a sufficient distance away from the bottom

fixture without any contact with the sample. The top fixture was then given a downward displacement of 20 mm/min. The displacement continued until there was a position load high enough to show that the sample was fully clamped (around 100 N depending on which fixtures and substrate materials were being used). When this load reading was reached, the displacement was stopped and the sample was held fully clamped for 10 seconds. This is the loading part of the experiment. The top fixture was then given an upward displacement of 20 mm/min to unload the sample. This upward movement was continued for 45 seconds so that the top fixture was far away at a place where it was no longer touching the sample. The downward movement, hold, and upward movement for a total 100 seconds complete one cycle. The resistance measurements were monitored throughout the test. Tests were conducted for 100 to 300 cycles, not necessarily until failure. The focus of this thesis is to understand resistance change over biaxial surfaces primarily under monotonic loading. Thus, the fatigue characteristics are preliminary and are intended to understand the resistance change with cycling. Also, most of the intended applications for the selected samples, especially the antennas, are expected to undergo at best a few hundred cycles. Ongoing work by others at Georgia Tech may focus on biaxial fatigue loading until complete cracking and failure.

The sensors tested were oriented where the ink structures were in tension during the dome tests and tension in the length direction and compression in the width direction during saddle-like testing. Figure 39 and Figure 40 how the tension and compression directions on the sensor geometry.

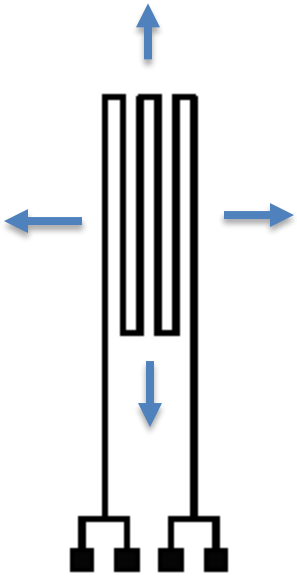

Figure 39: Tension and compression directions during dome test

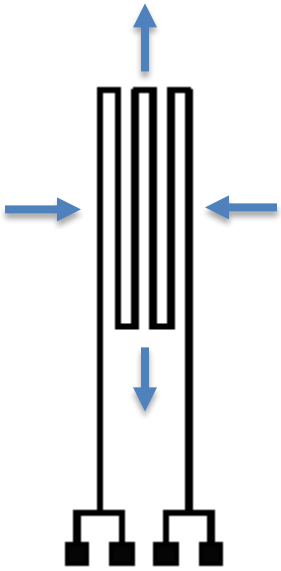

Figure 40: Tension and compression directions during saddle-like surface test

6.3 Testing of Air-Dried Sensor Sample on PET

First, the air-dried PET samples with Suntronic™ ink were tested on the 4 in. dome. Figure 41 and Figure 42 show the resistance results of one of the tests using air dried ink. The change in resistance from undeformed to deformed was about 0.1%.

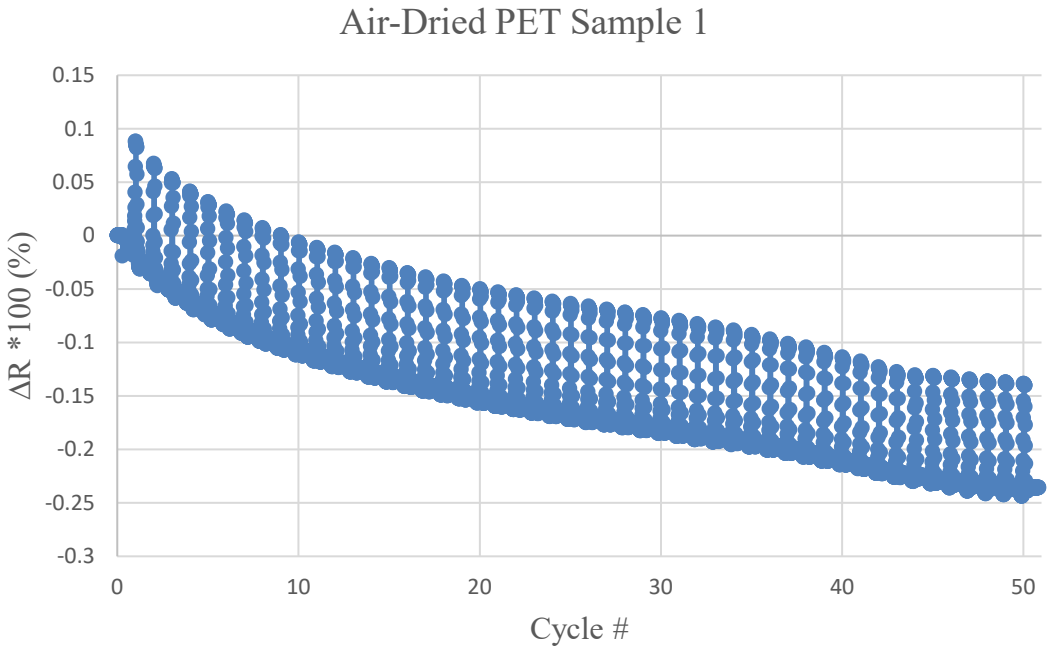

Figure 41: Results of air-dried PET sample 1 during 4 in. dome test

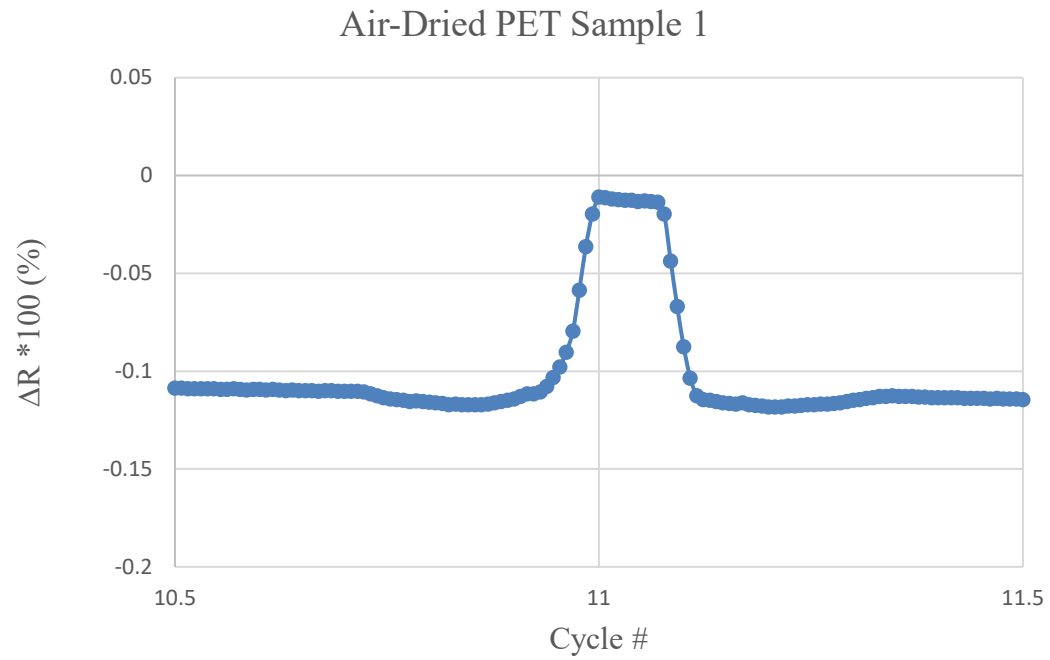

Figure 42: Close view of results of air-dried PET sample 1 during 4 in. dome test

In Figure 42, the flatter area before and after the bump represents the time where the sensor is not under any load. The increase in resistance just before the bump represents the time when the sensor starts to be loaded, the flat area with higher resistance represents the 10 seconds where the sensor is fully clamped, and the area with sharp decreasing resistance represents the sensor being unloaded. One can see from Figure 42 that the change in resistance is about 0.1%. It should be pointed out that although the resistance increased during loading in each cycle, the overall resistance showed a continued decrease in resistance with cycling. This phenomenon has been seen in the same ink in other yet-to-be-published research by other collaborating researchers elsewhere. Additional discussion on this phenomenon is presented in a later section in this chapter.

Figure 43 shows another air-dried PET sample subjected to a 4 in. dome test. The gap in the resistance band from about 38 cycles to about 45 cycles is due to an accidental programming change in data sampling rate, and is not related to any real resistance change or failure in the sample. As seen, the resistance suddenly increases after 50 cycles and stays higher thereafter. This is due to cracking of the ink due to fatigue loading, as shown later in SEM images.

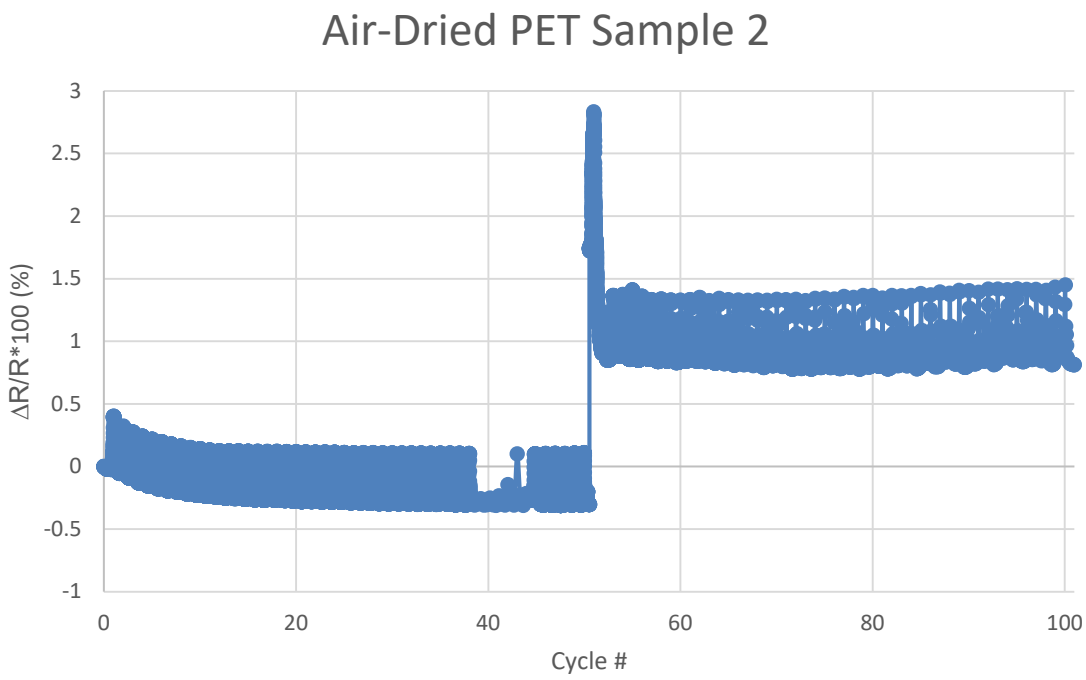

Figure 43: Results of air-dried PET sample 2 during 4 in. dome test

Figure 44 shows the locations of SEM imaging and these images of the second air-dried PET sample at zero cycles.

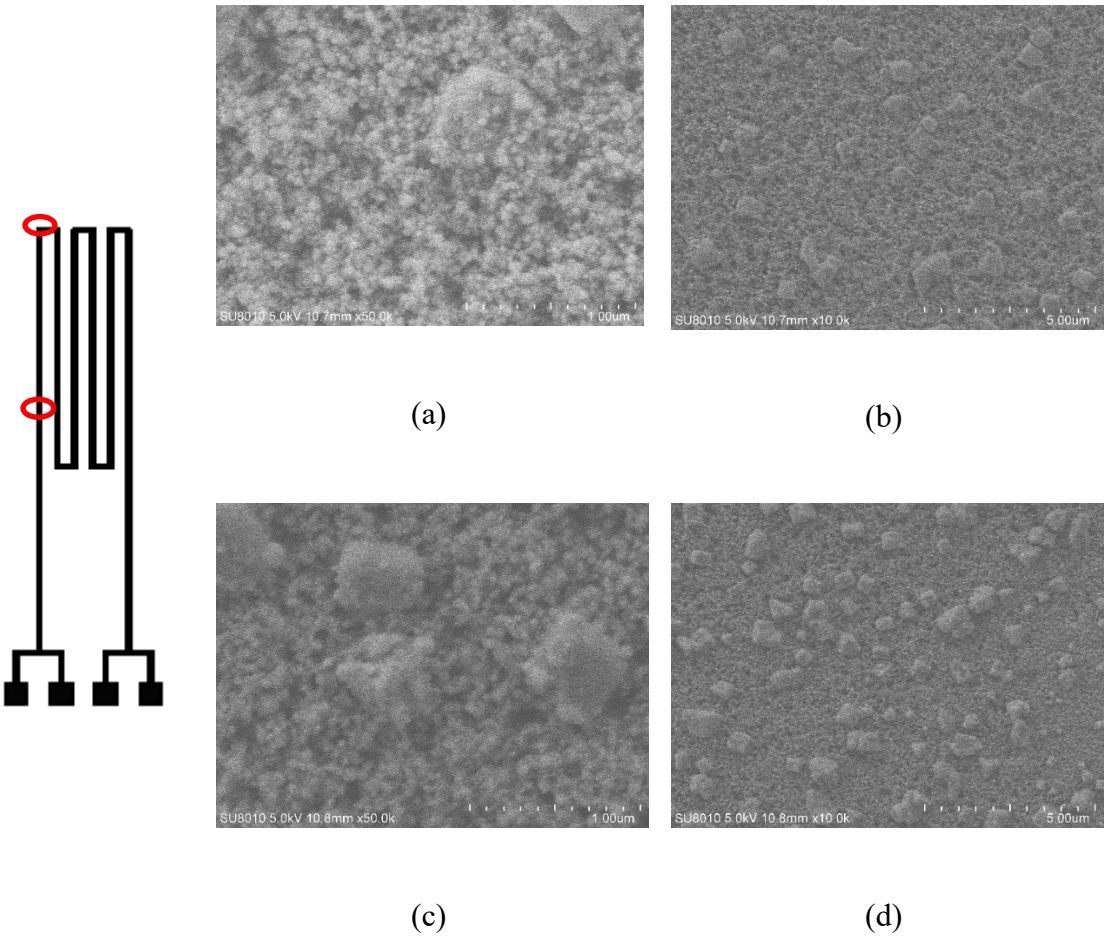

Figure 44: SEM images of second air-dried PET sensor sample at zero cycles. (a) Corner location, 50k magnification (b) corner location, 10k magnification, (c) side location, 50k magnification, and (d) side location, 10k magnification

Figure 45 shows the SEM images of the same regions of the second air-dried PET sample after 100 cycles.

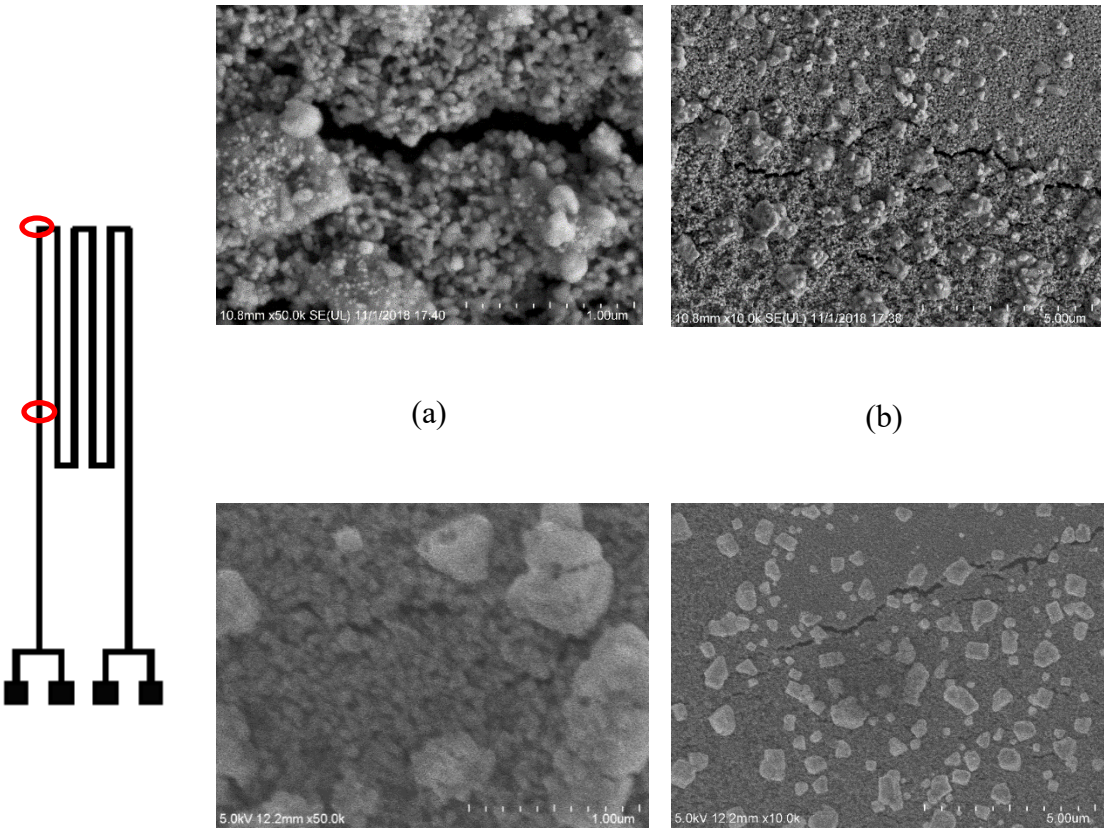

Figure 45: SEM images of second air-dried PET sensor at 100 cycles. (a) Corner location, 50k magnification (b) corner location, 10k magnification, (c) side location, 50k magnification, and (d) side location, 10k magnification

6.4 Testing of Oven-Cured Sensor Sample on PET

4 in. dome tests were performed on PET samples cured in the oven as well. Figure 46 and Figure 47 show the 4 in. dome results for an oven cured PET sample.

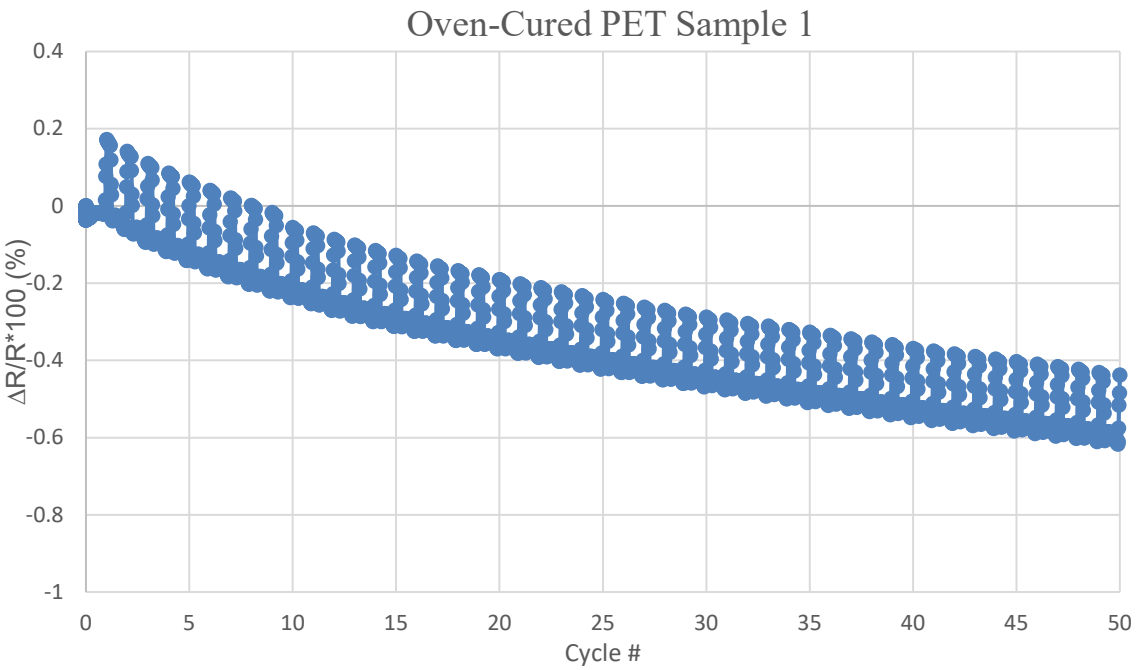

Figure 46: Results of oven-cured PET sample 1 during 4 in. dome test

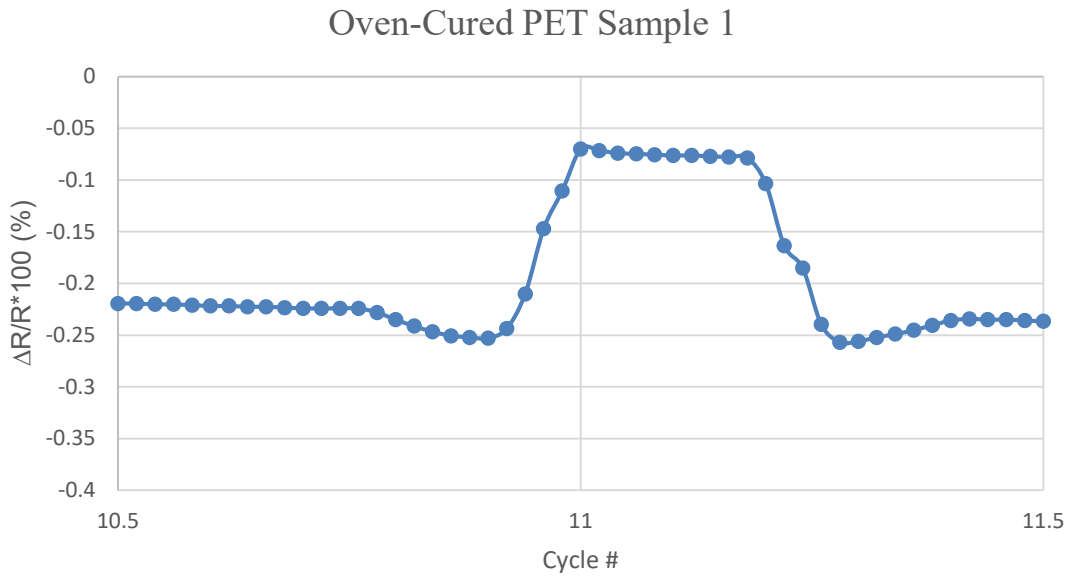

Figure 47: Close view of results of oven-cured PET sample 1 during 4 in. dome test

Figure 48 below shows the resistance results of a second oven-cured PET sample subjected to a 4 in. dome test.

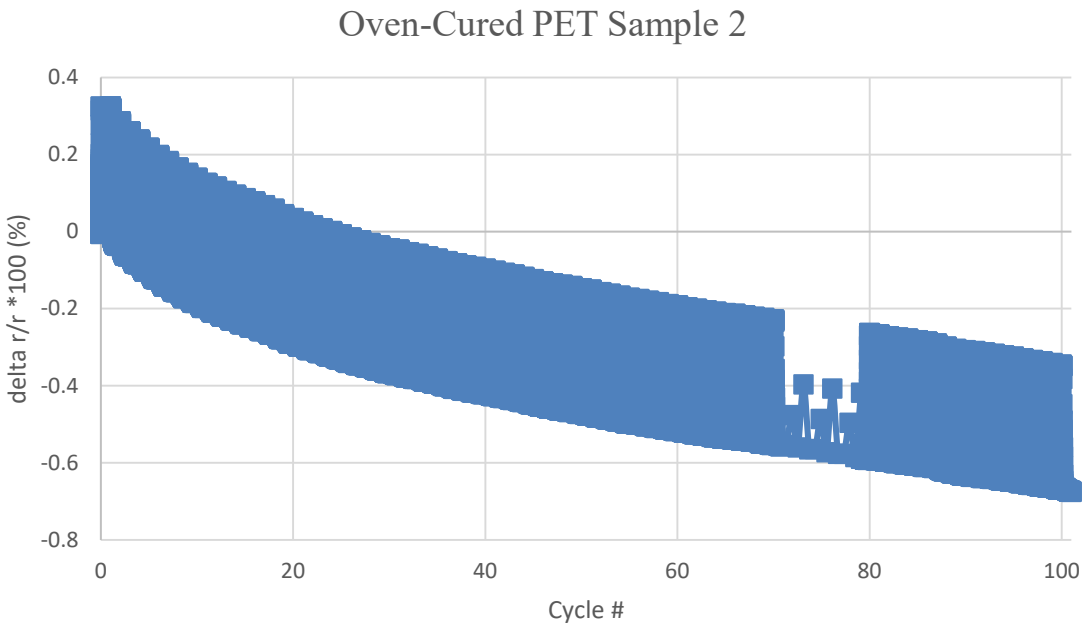

Figure 48: Results of all 100 cycles of oven-cured PET sample 2 during 4 in. dome test

As seen, with oven-cured sensor samples on PET, the overall resistance continues to drop cycling, as happened in air-dried samples. However, with the oven-cured samples, the resistance does not show any sudden increase after 50 cycles, unlike the air-dried sensor sample on PET. This indicates that there is possibly no cracking in the ink over 100 cycles. This is also demonstrated through SEM images as shown in Figure 49 and Figure 50.

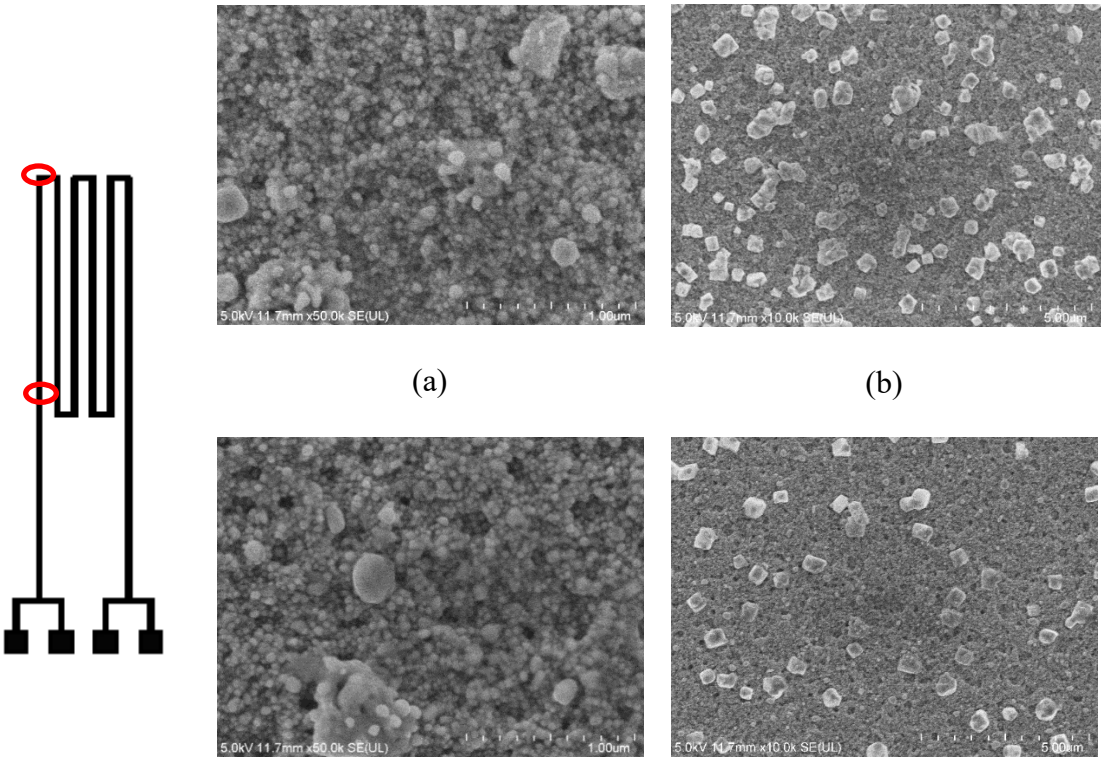

Figure 49: SEM images of 2nd oven-cured PET sensor at zero cycles. (a) Corner location, 50k magnification (b) corner location, 10k magnification, (c) side location, 50k magnification, and (d) side location, 10k magnification

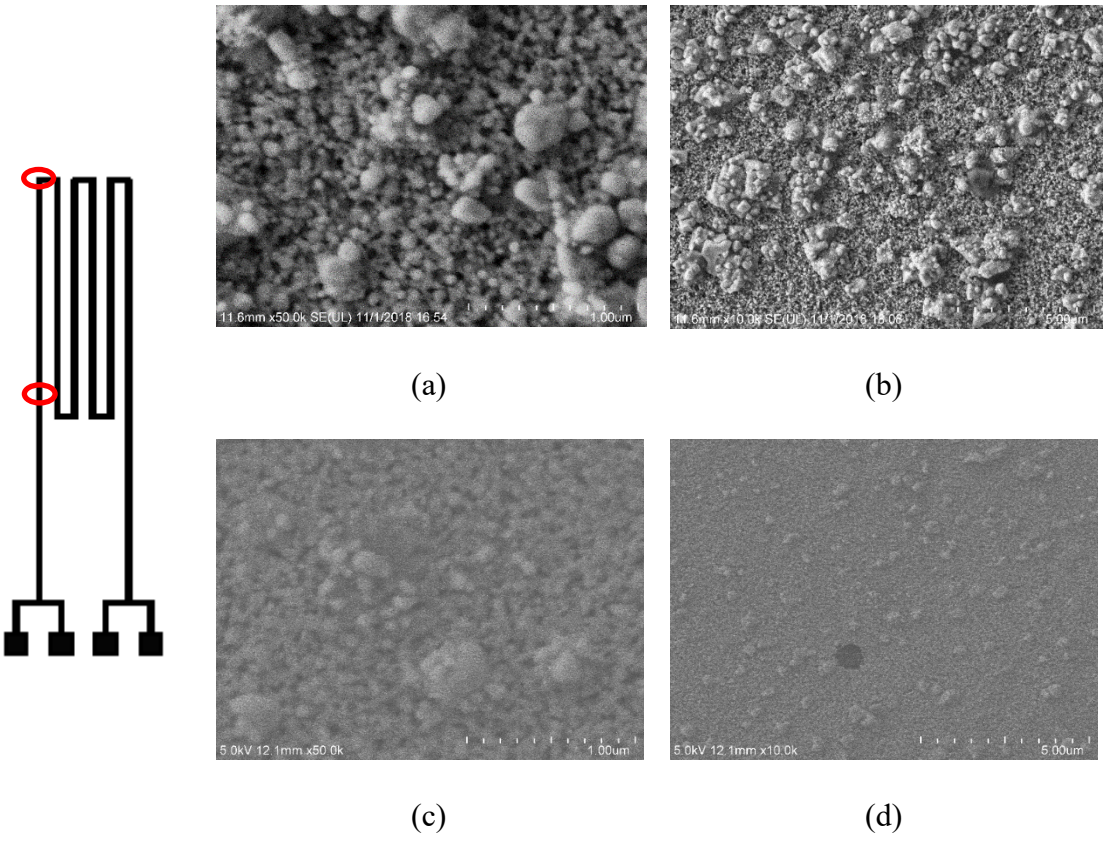

Figure 50: SEM images of 2nd oven-cured PET sensor at 100 cycles. (a) Corner location, 50k magnification (b) corner location, 10k magnification, (c) side location, 50k magnification, and (d) side location, 10k magnification

6.5 Testing of Oven-Cured Sensor Sample on LCP

Before discussing the test results for sensor sample on LCP, it may be worthwhile to re-state some of the processing conditions. The strain sensors were made with Suntronic® ink ink-jet printed on Rogers LCP and cured at 200°C for 30 minutes.

The LCP samples were tested in a similar way as the PET samples. One of the LCP samples was tested on the 4 in. saddle for 300 cycles with the length of the sensor in tension. SEM imaging was taken at 0, 100, 200, 250, and 300 cycles in the same way as the PET

samples. Figure 51 shows the SEM images of the side location of the sensor up to 200 cycles.

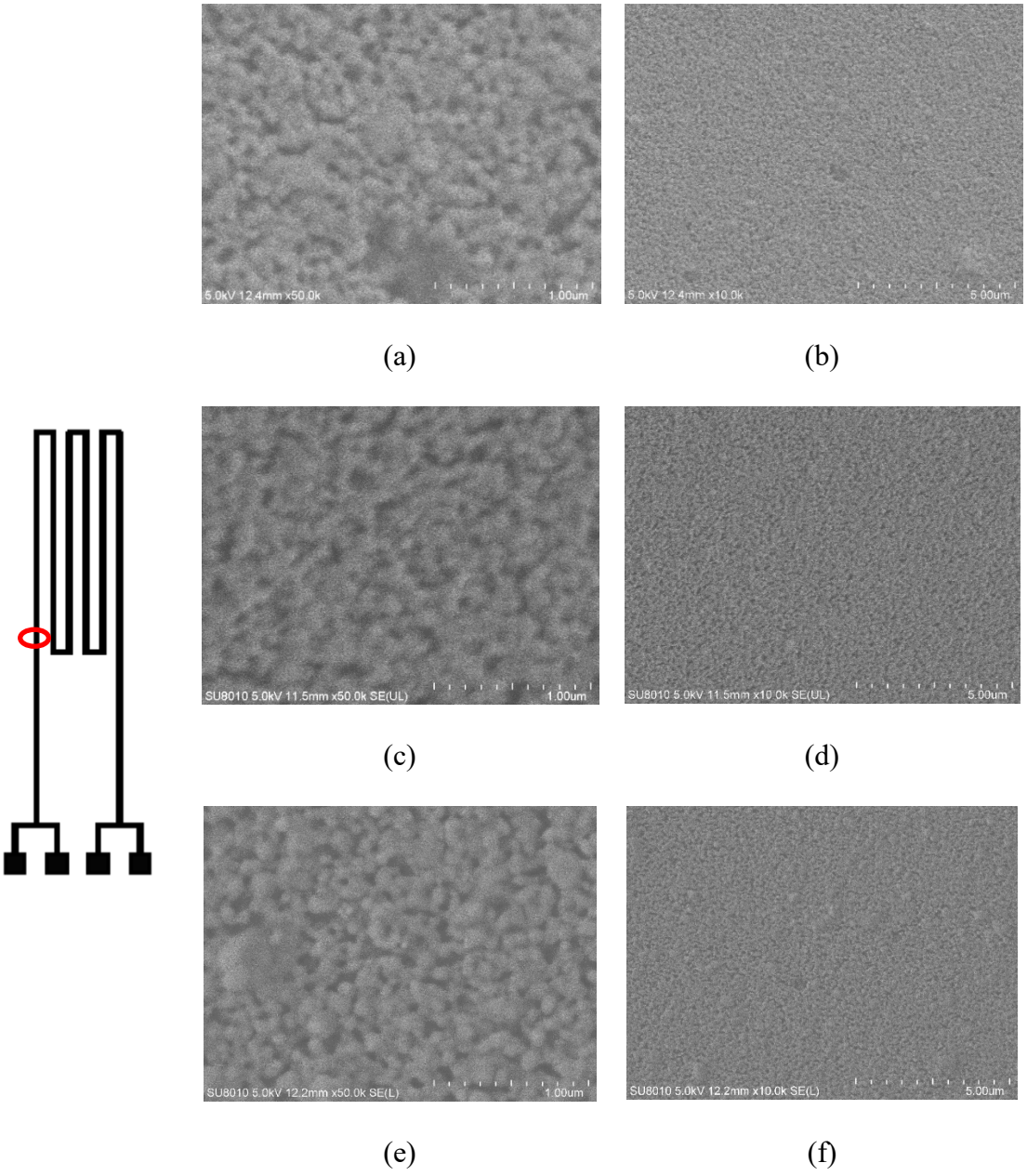

Figure 51: SEM images of Suntronic® ink on LCP taken at side location of the long test LCP sample. (a) side location, 50k magnification, 0 cycles, (b) side location, 10k magnification, 0 cycles, (c) side location, 50k magnification, 100 cycles, (d) side

location, 10k magnification, 100 cycles, (e) side location, 50k magnification, 200 cycles, (f) side location, 10k magnification, 200 cycles

The corner location of the sensor was also imaged at the same cycles as the side location. Figure 52 shows SEM images of the corner locations at 0 and 100 cycles before cracks were observed.

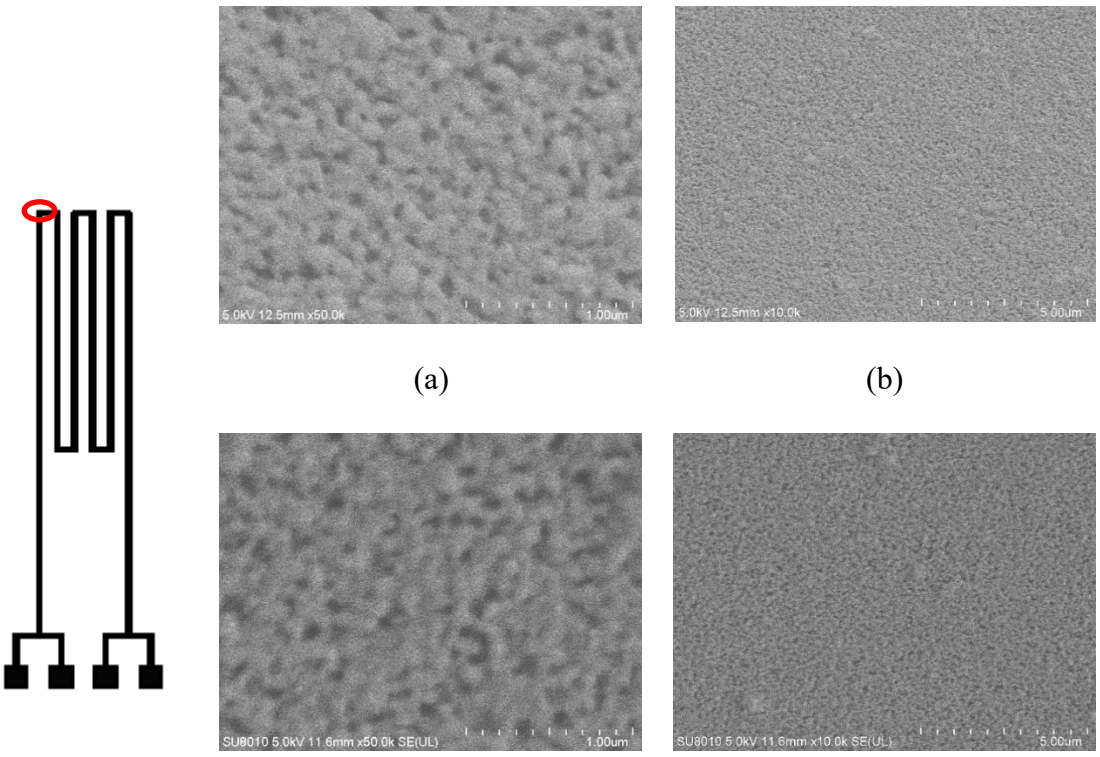

Figure 52: SEM images of Suntronic® ink on LCP taken at corner location of the long test LCP sample. (a) corner location, 50k magnification, 0 cycles, (b) corner location, 10k magnification, 0 cycles, (c) corner location, 50k magnification, 100 cycles, (d) corner location, 10k magnification, 100 cycles

Cracks were first seen in the corner location at 200 cycles. Figure 53 shows SEM images of cracks in the corner location at 200 cycles.

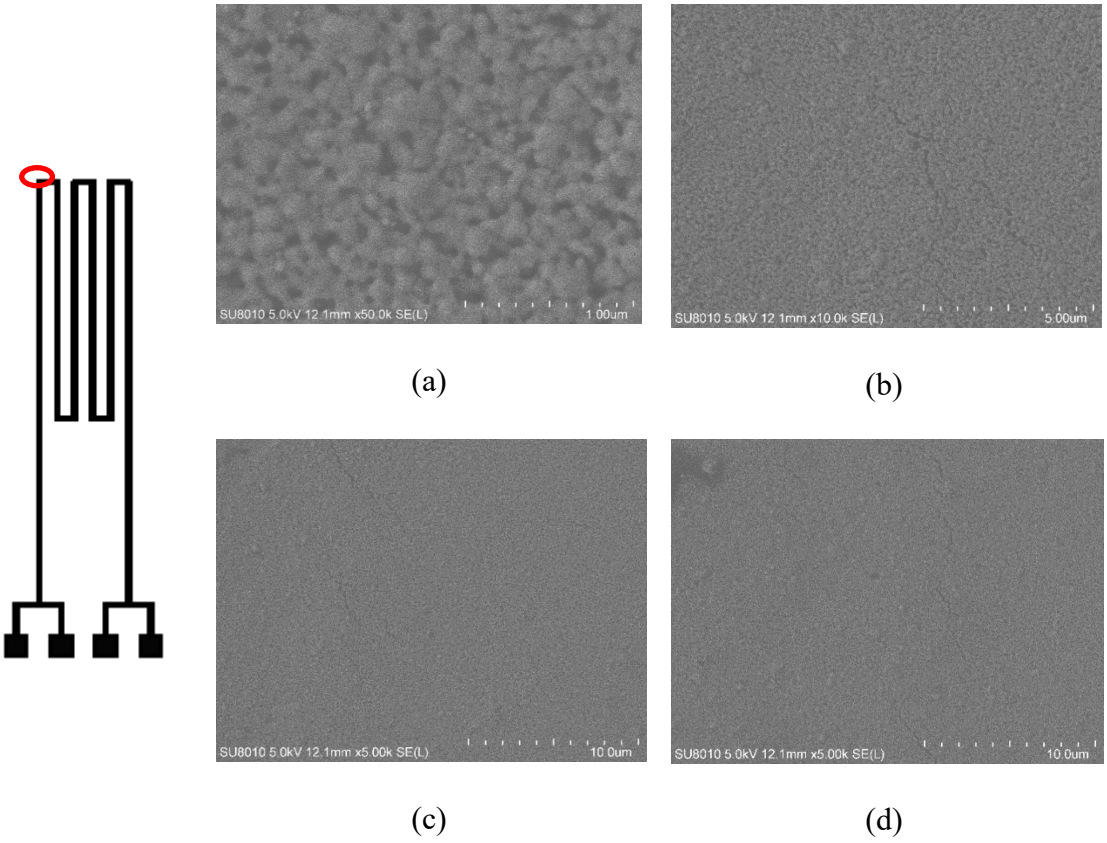

Figure 53: SEM images of Suntronic® ink on LCP taken at corner location of the long test LCP sample at 200 cycles. (a) Corner location, 50k magnification, (b) corner location, 10k magnification, (c) corner location, 10k magnification, (d) corner location, 5k magnification

Figure 54 shows resistance values just after 100 cycles.

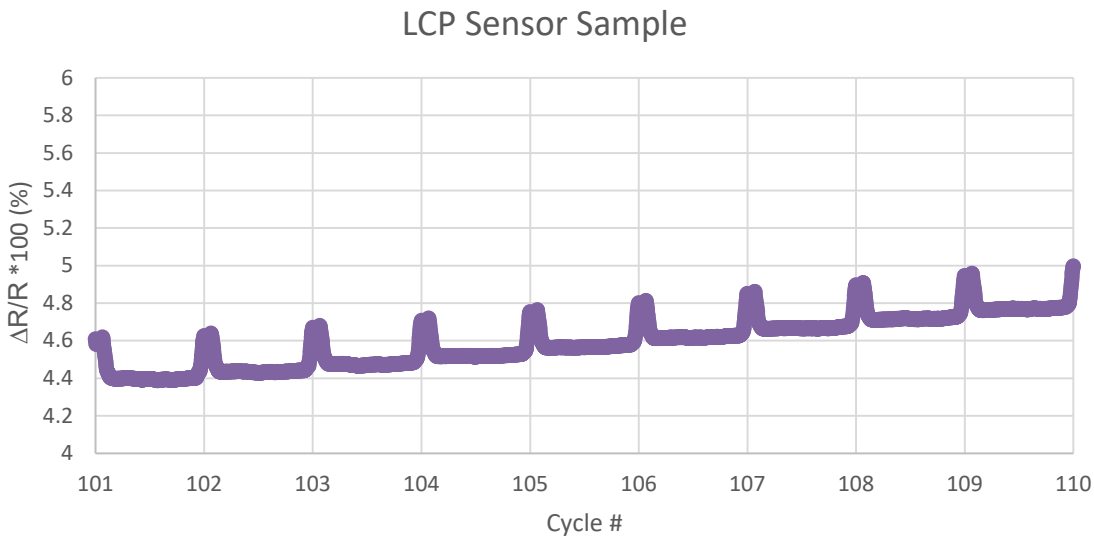

Figure 54: Resistance results of LCP sensor sample just after 100 cycles

The first cracks seen in the side locations appeared when the ink was imaged at 250 cycles. Figure 55 shows SEM images of the side location at 250 cycles while Figure 56 shows SEM images of the corner location at 250 cycles.

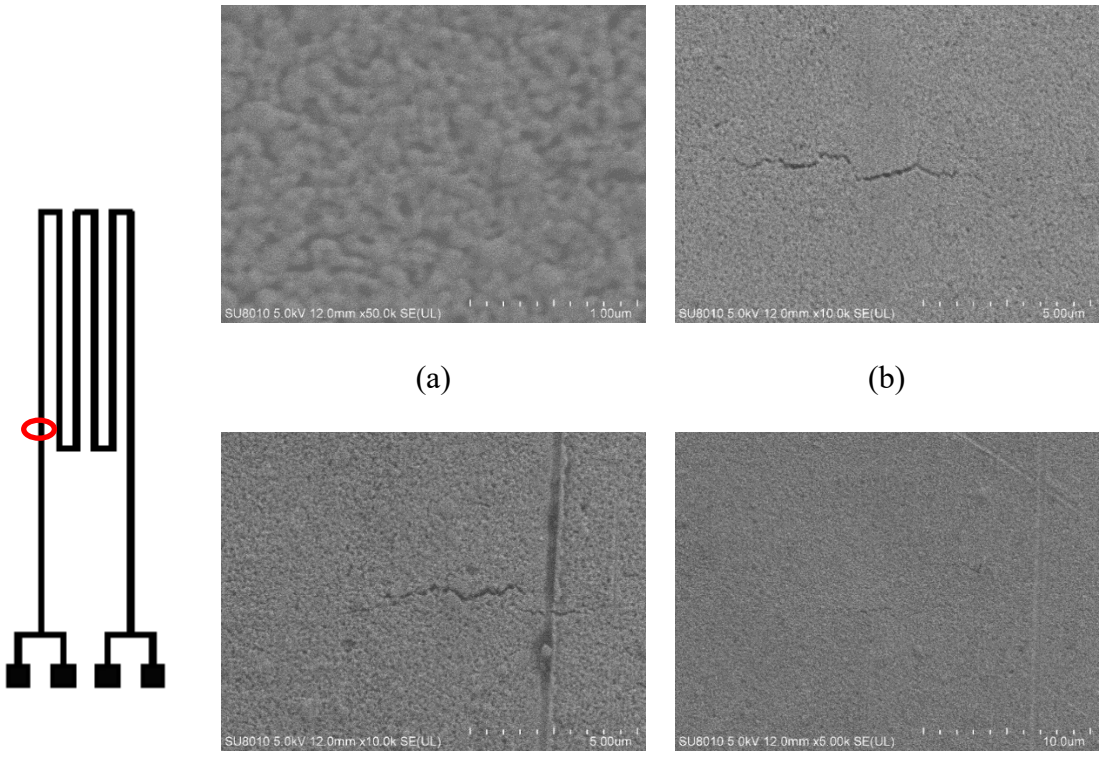

Figure 55: SEM images of Suntronic® ink on LCP taken at side location of the long test LCP sample at 250 cycles. (a) Side location, 50k magnification (b) side location, 10k magnification, (c) side location, 10k magnification, and (d) side location, 5k magnification

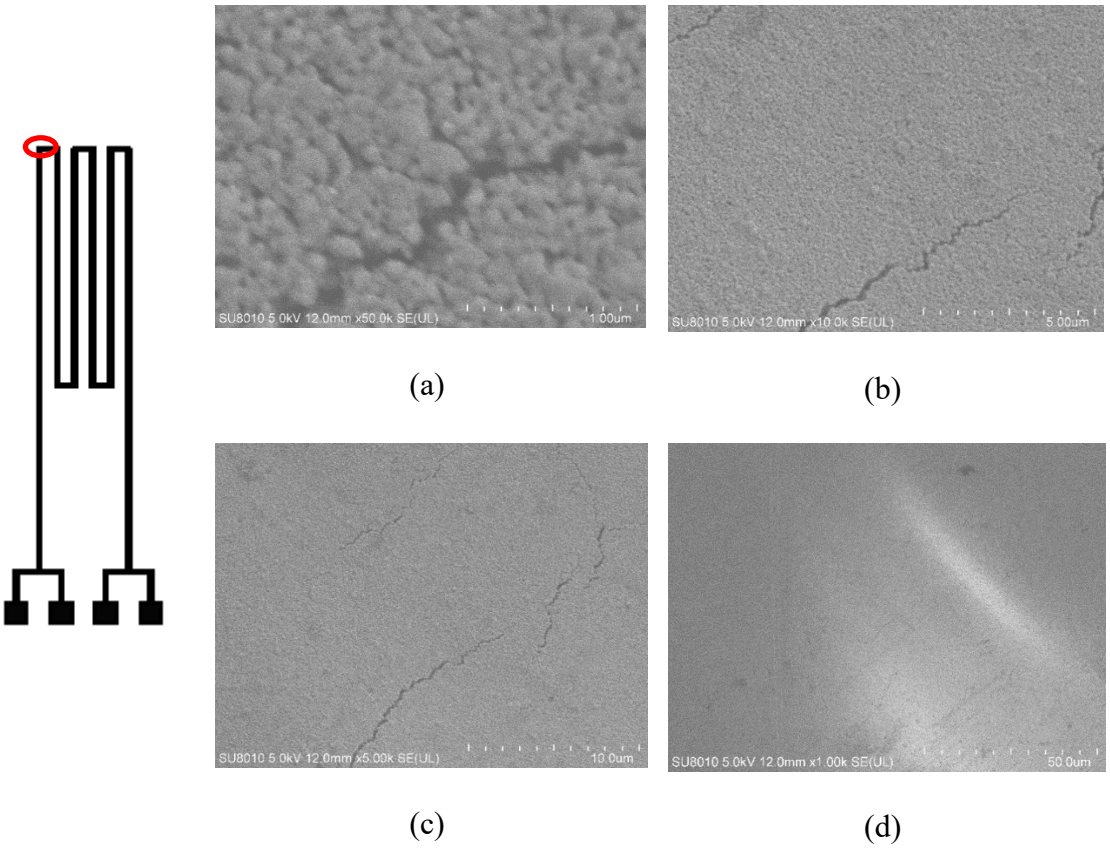

Figure 56: SEM images of Suntronic® ink on LCP taken at corner location of the long test LCP sample at 250 cycles. (a) Corner location, 50k magnification, (b) corner location, 10k magnification, (c) corner location, 5k magnification, (d) corner location, 1k magnification

Figure 57 shows resistance values just after 250 cycles.

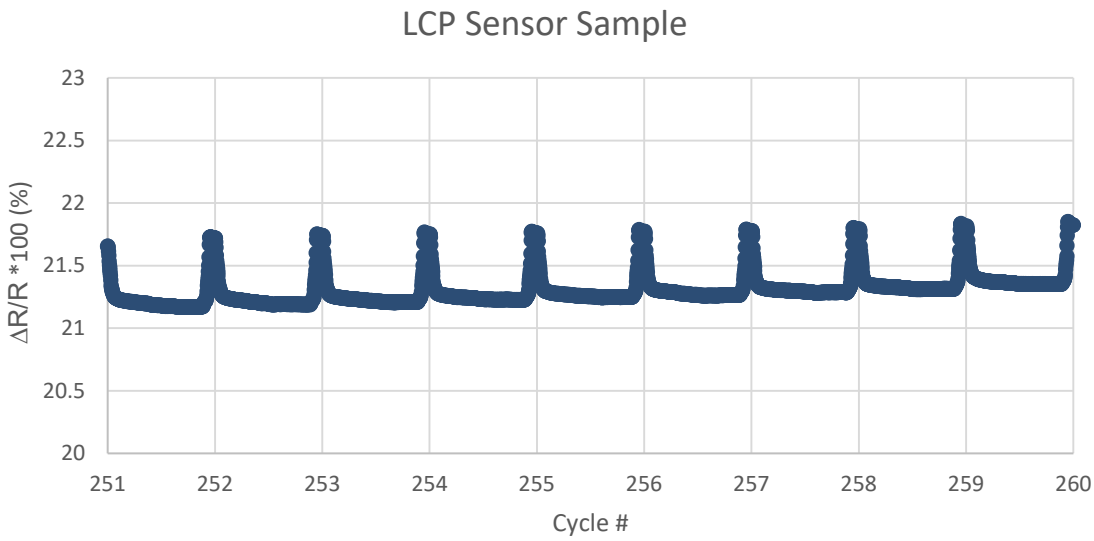

Figure 57: Resistance results of LCP sensor sample just after 250 cycles

The resistance continued to increase and the cracks continued to grow. Figure 58 shows SEM images of the side location and Figure 59 shows images of the corner location at 300 cycles after the test was complete.

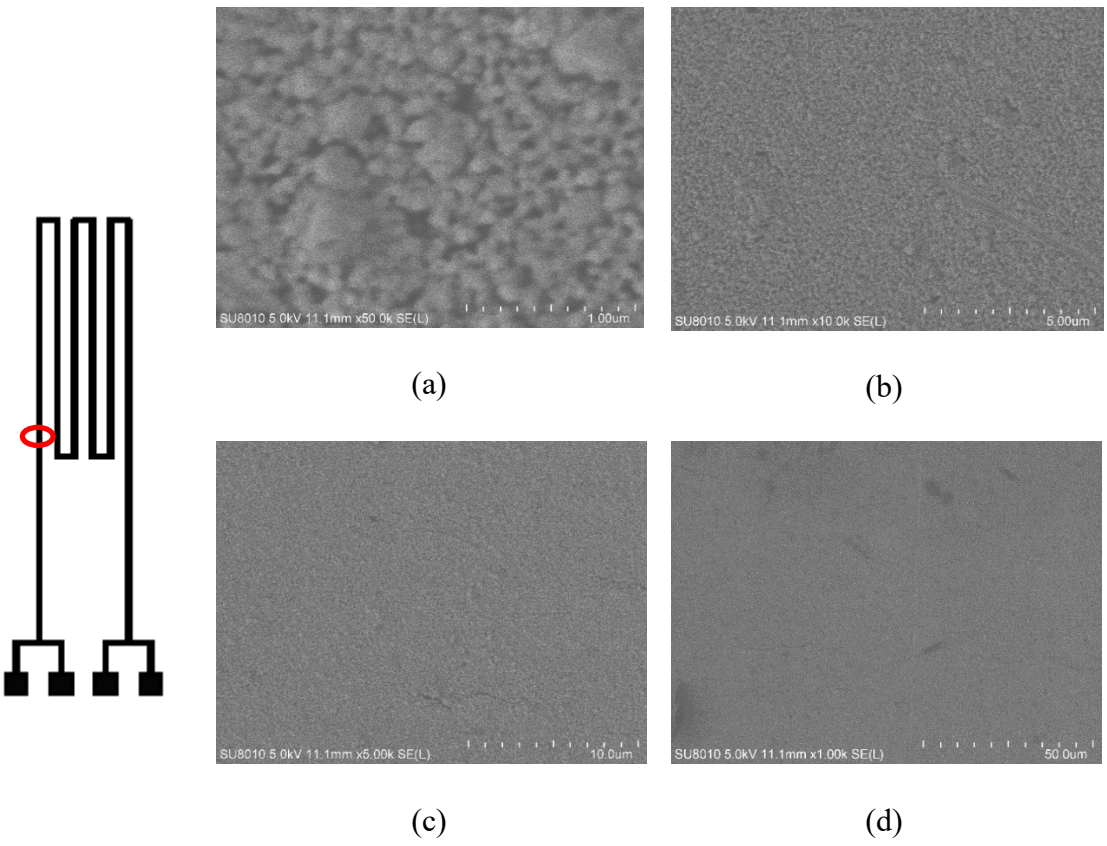

Figure 58: SEM images of Suntronic® ink on LCP taken at side location of the long test LCP sample at 300 cycles. (a) Side location, 50k magnification (b) side location, 10k magnification, (c) side location, 5k magnification, and (d) side location, 1k magnification

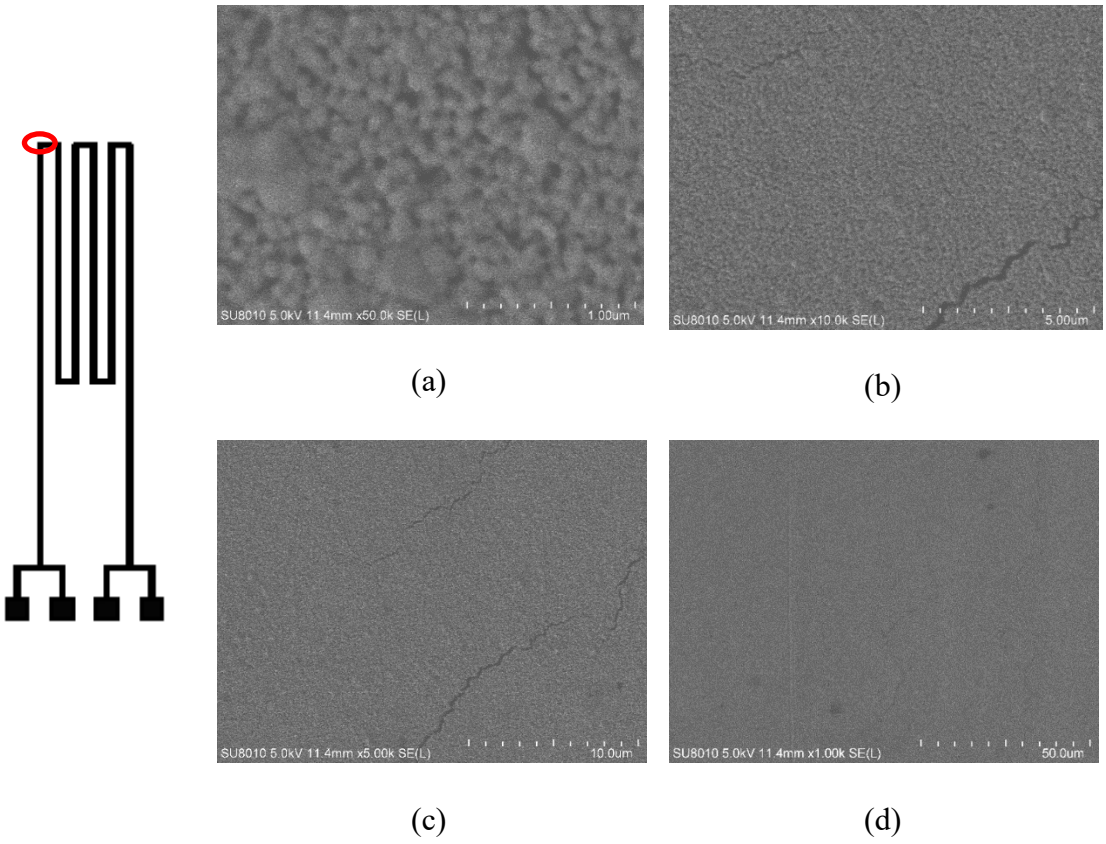

Figure 59: SEM images of Suntronic® ink on LCP taken at corner location of the long test LCP sample at 300 cycles. (a) Corner location, 50k magnification, (b) corner location, 10k magnification, (c) corner location, 5k magnification, (d) corner location, 1k magnification

Figure 60 shows the resistance results for this sample at the end of the test.

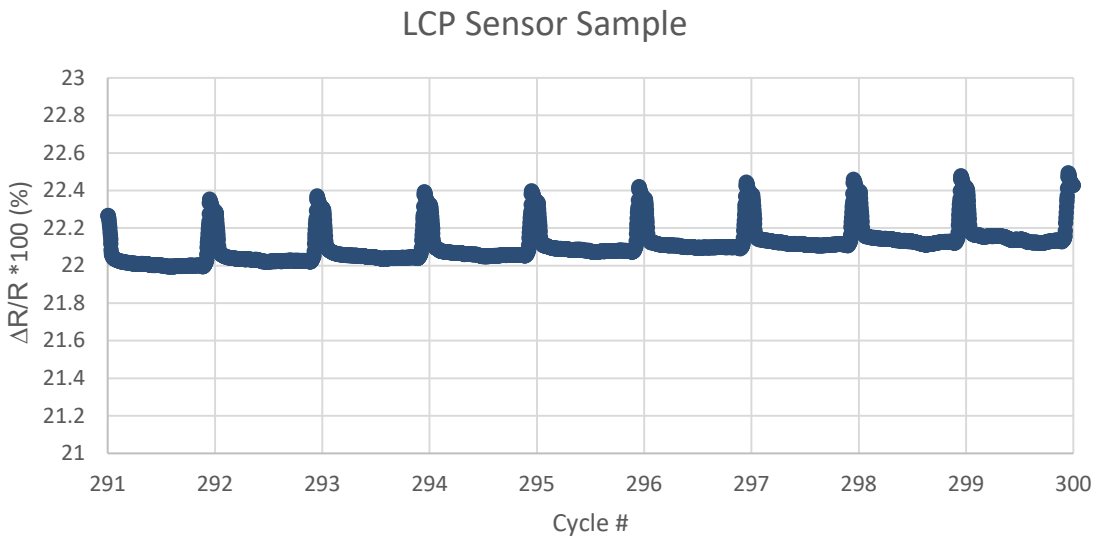

Figure 60: Resistance results of LCP sensor sample at end of test

As expected, the resistance kept increasing over time with a total increase of over 20%. The SEM images from the areas in the middle of the trace showed cracks developing in the horizontal direction, while those in the corner showed cracks developing at large angles. In addition, the cracks appeared earlier in the corner location and were larger. One can see from Figure 56 that the cracks are created from particles that have necked together pulling apart. There does not appear to be any individual particles splitting apart, which shows that failure depends on how much necking has occurred between the particles.

6.6 Results and Discussion

One major difference between the different silver inks are their particle distributions. On can see from Figure 49 that the Novacentrix® ink has a fairly large distribution of particles sizes from small to large, chunky looking pieces. The Suntronic® ink appears to have a more uniform particle size distribution as seen in Figure 51. One can

also see from Figure 51 that the particles in the Suntronic® ink appear to undergo significant necking together during the curing process. Unlike the Suntronic® ink, the Novacentrix® ink does not appear to have as much necking between particles in either the oven-cured or air-dried samples. The most likely reason for this is the difference between curing temperatures (200°C vs. 90°C). One interesting observation is the difference between the ink structures of the oven-cured and air-dried Novacentrix® ink. One can see from Figure 44 and Figure 49 that there does not appear to be a significant difference. Even though there is not much of a visual difference, the oven-cured samples did have a much lower electrical resistance. One possible reason is that the capping agent within the ink flows off the particles better at higher temperatures or the elevated temperature causes it to decompose.

The resistance trends during cycling for the Novacentrix® ink on PET samples had unexpected results. One would expect the resistance of the silver ink to immediately increase during cycling as the ink structure is damaged. The resistance of both the oven-cured and air-dried Novacentrix® samples decreased during each test. As the cycling continued, the resistance trend would either start to flatten out or begin to increase. This goes against what is usually seen in literature when silver inks undergo cyclic straining. There have been observed cases of thin metal films deposited by evaporation on polymers whose electrical resistance decrease during cyclic loading [44],[31]. This, however, was not seen in the silver ink tests performed alongside these films [31] . The decrease in resistance in the Novacentrix® ink samples most likely has something to do with the microporous coating on PET substrates onto which the ink was printed. It is hypothesized that with repetitive loading and unloading cycles, the encapsulant on the particle break and

thus, particle-to-particle contact improves resulting in lower resistance with fatigue cycling.

An interesting observation from the SEM images of the Suntronic® ink is the orientation of the cracks. When comparing the cracks from the middle location in Figure 61 to the cracks in the corner location in Figure 62, one can see that this in the middle are mostly horizontal, while those in the corner are angled. These crack directions seem to agree with the stress contours obtained through finite-element simulations in later sections.

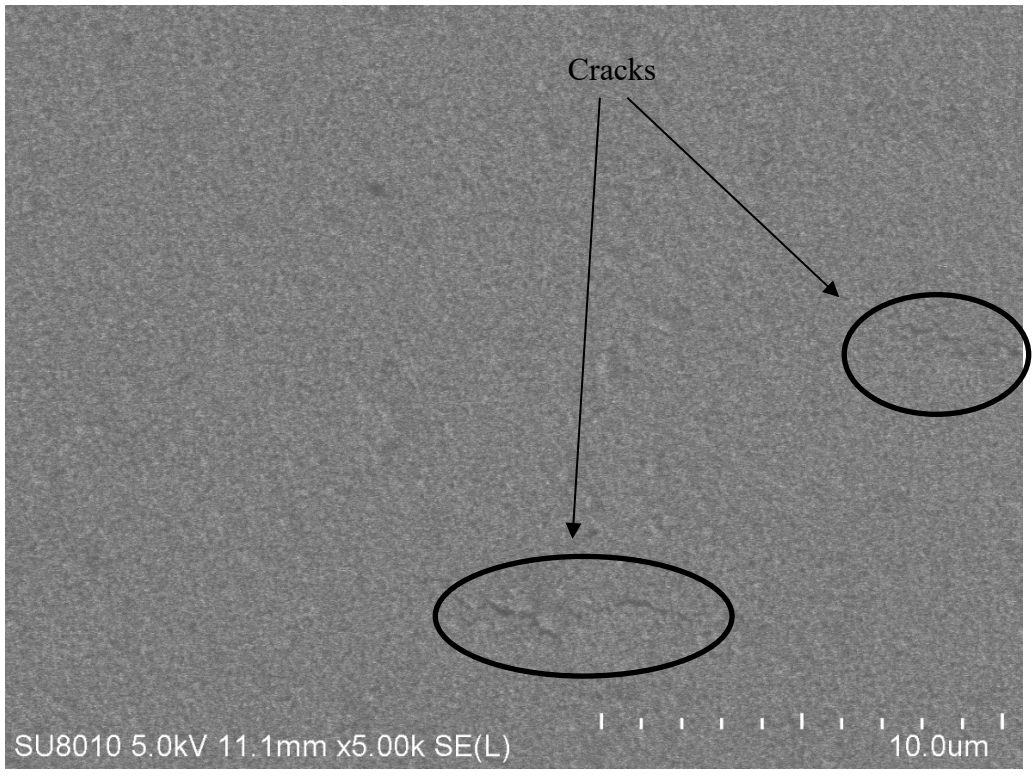

Figure 61: Cracks in Suntronic® ink in middle SEM location at 300 cycles

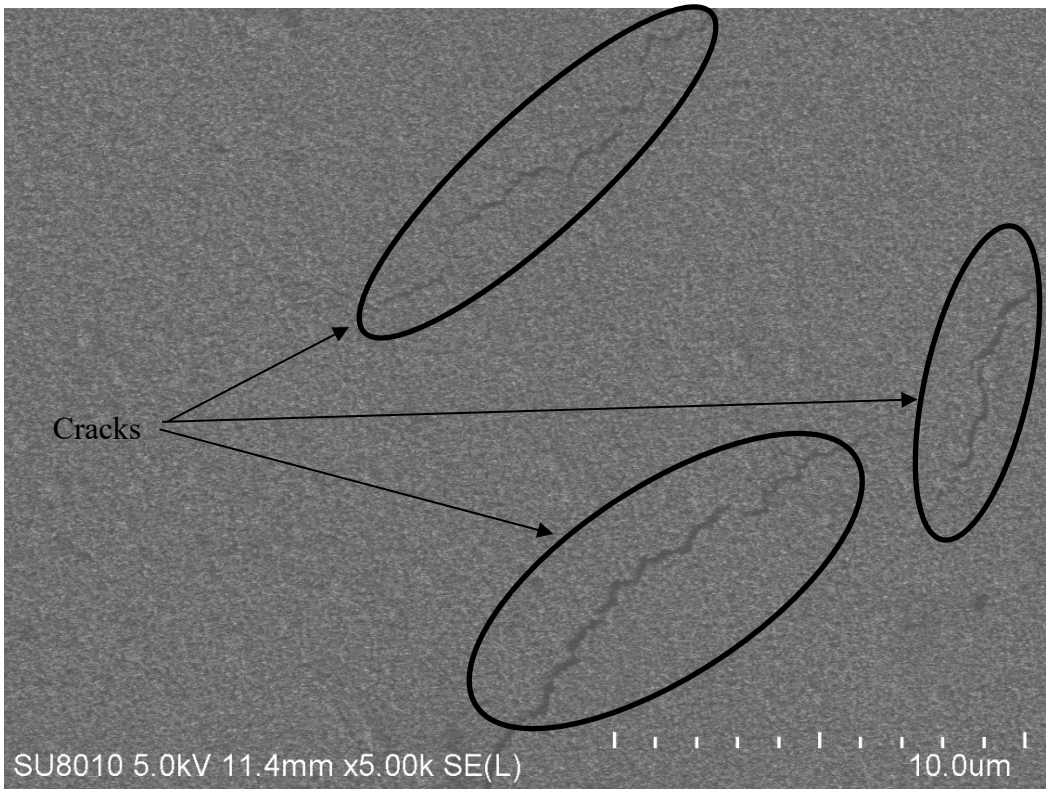

Figure 62: Cracks in Suntronic® ink in corner SEM location at 300 cycles

CHAPTER 7

ANTENNA TESTING

Measurements were taken for both uniaxial and biaxial bending. The uniaxial bending used various radii of curvature and orientations of the bending (bending along length and along width). A full set of measurements was first done before the environmental coating was applied, and then another full set was done after the coating. Plastic cylinders were used to apply the uniaxial bending to the antenna while the 3D printed fixtures seen in Figure 32 and Figure 33 were used to apply the saddle and barrel-like bends. All measurements were carried out in the Athena Lab at Georgia Tech.

7.1 Copper Antenna

The copper 8x8 antenna showed in Figure 26 was initially tested to obtain a baseline set of measurements. Figure 63 and Figure 64 show the copper antenna before coating undergoing cylindrical, and barrel-like bending. For saddle and barrel-like bending, the length direction of the antenna was under the 4 in. bend radius in tension, while the width direction was under the 40 in. bend radius in tension or compression.

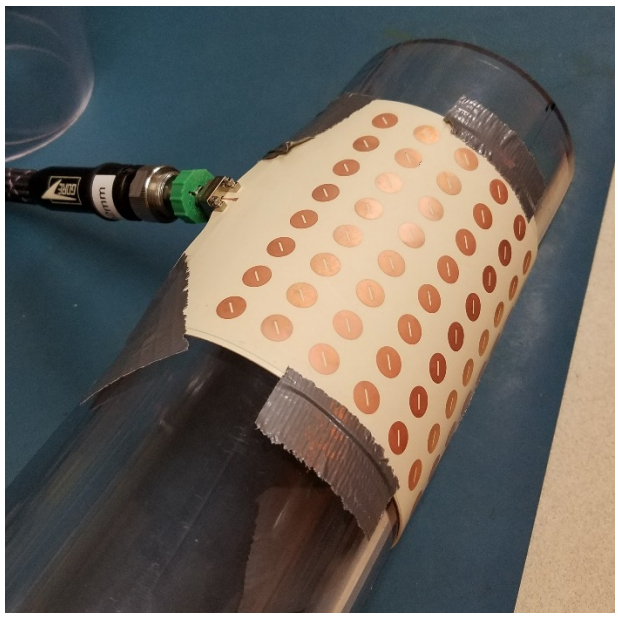

Figure 63: Uncoated 8x8 copper antenna bent along length on 2 in. radius cylinder

Figure 64: Uncoated 8x8 copper antenna sandwiched in between 4x40 in. barrel-like fixtures

The S11 results for the uncoated 8x8 copper antenna are shown in Figure 65 and Figure 66 below.

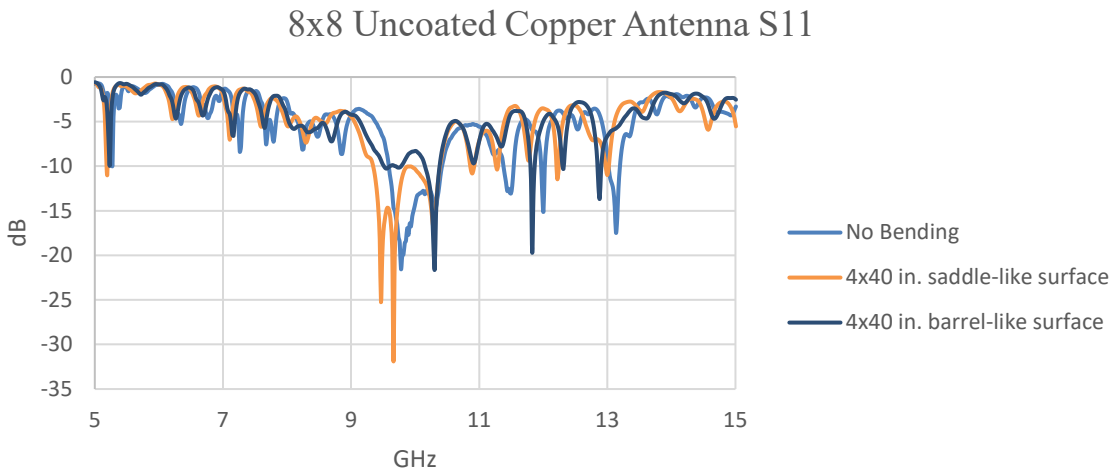

Figure 65: Uncoated 8x8 copper antenna S11 results for saddle and barrel-like bending

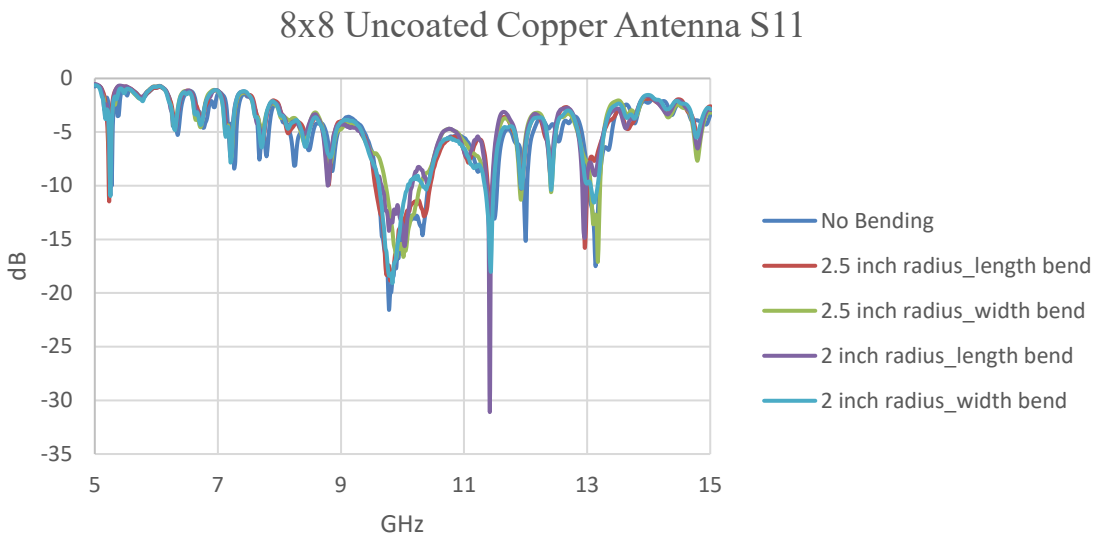

Figure 66: Uncoated 8x8 copper antenna S11 results for cylindrical bending

After applying the coating, the measurements were taken again. Figure 67 and Figure 68 show the S11 results after coating.

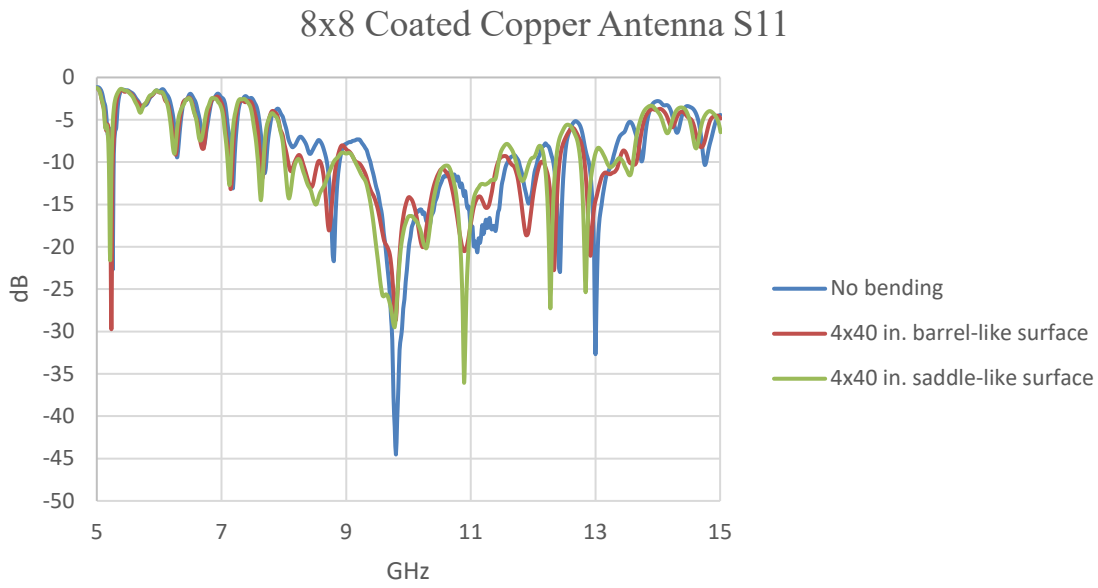

Figure 67: Coated 8x8 copper antenna S11 results for saddle and barrel-like bending

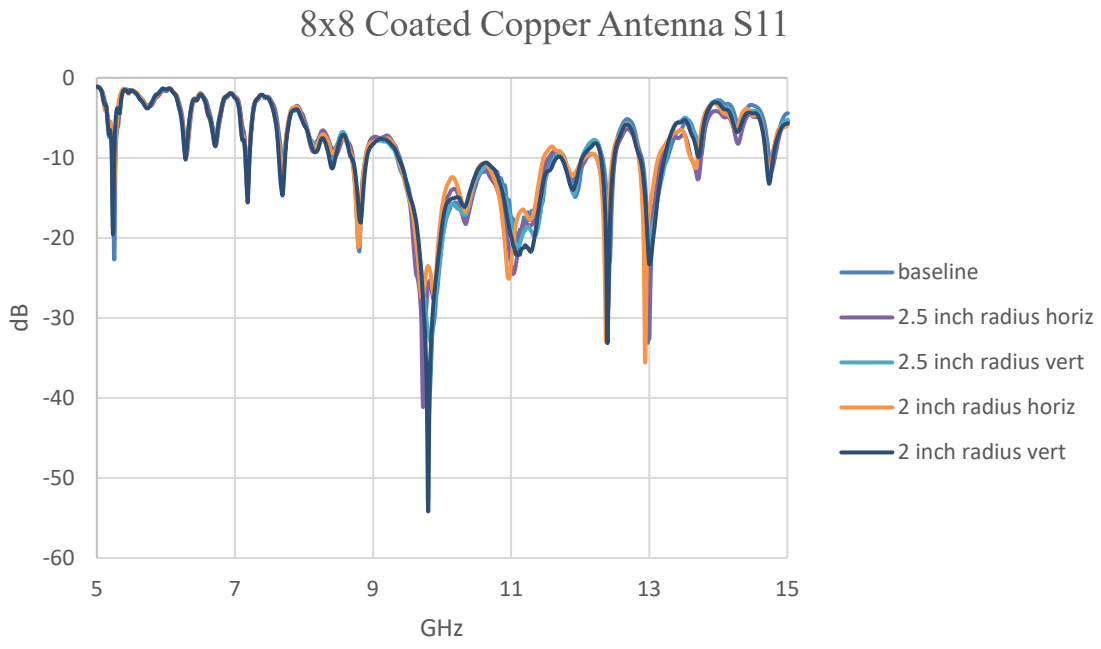

Figure 68: Coated 8x8 copper antenna S11 results for cylindrical bending

When bent over saddle and barrel-like surfaces, the uncoated copper antenna frequency seemed to shift lower for the saddle-like bend, and higher for the barrel-like bend. The cylindrical bending of the uncoated copper antenna did not produce significant changes. When the coated copper antenna was bent over the saddle and barrel-like surfaces, there were not significant changes. Similar to the uncoated copper antenna, the coated antenna did not experience significant changes during cylindrical bending.

7.2 Ink Antenna

After testing the copper antenna to obtain a baseline, the 8x8 ink antenna was tested. Figure 69 and Figure 70 show the S11 results of the uncoated ink antenna.

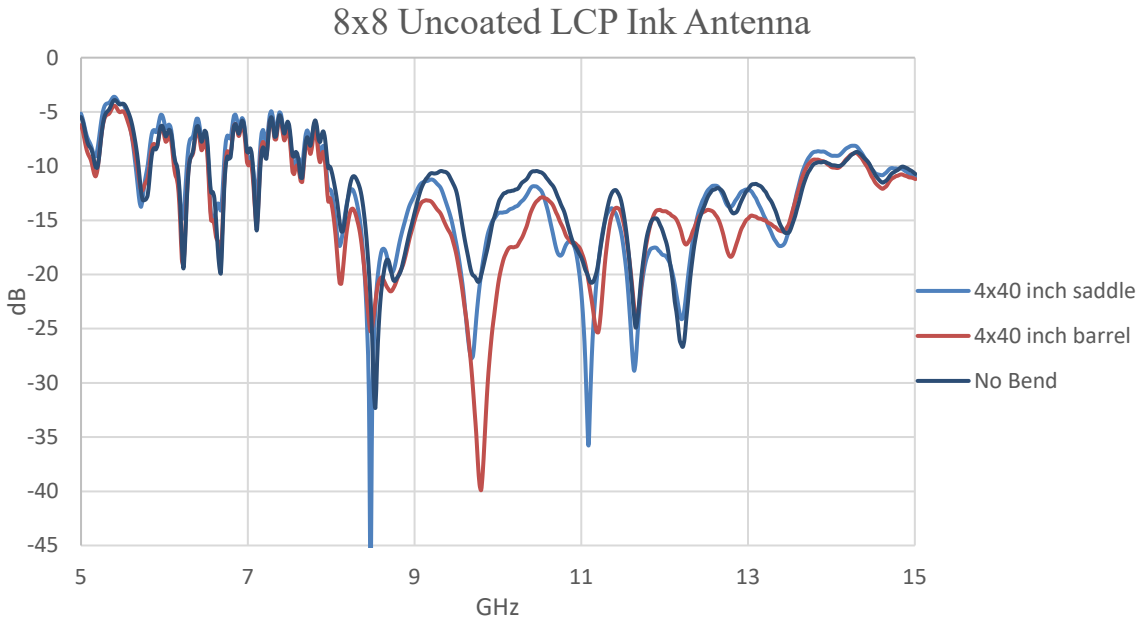

Figure 69: 8x8 uncoated LCP ink antenna S11 measurements when deformed to saddle and barrel-like surfaces

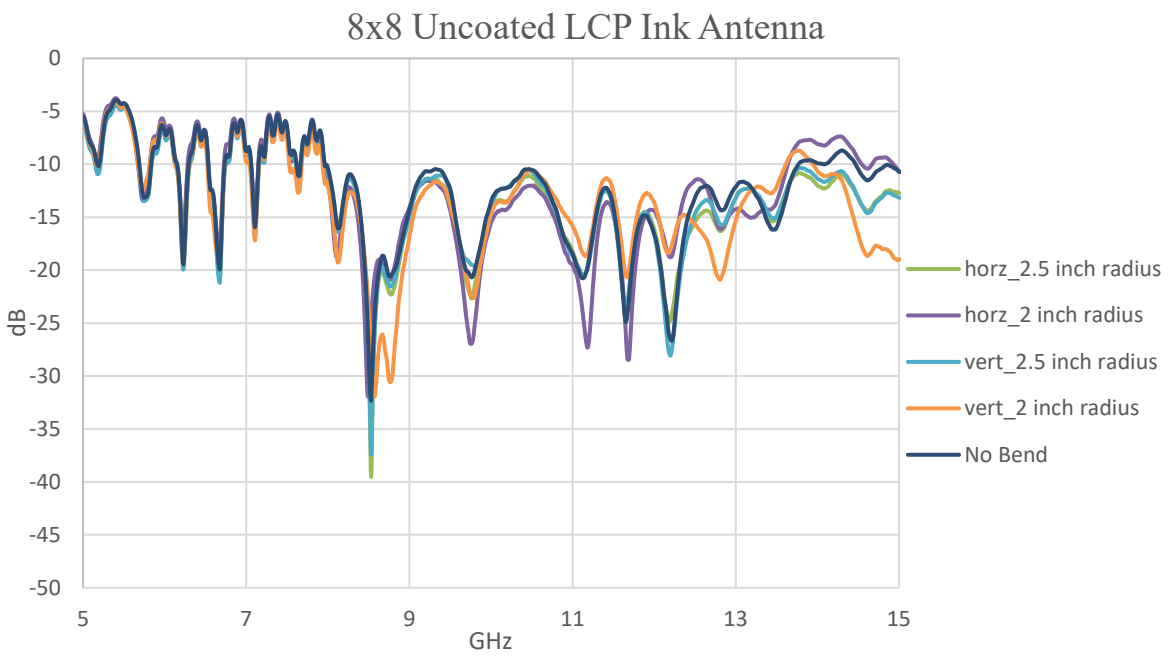

Figure 70: 8x8 uncoated LCP ink antenna S11 measurements undergoing cylindrical bending

The uncoated ink antenna results during saddle and barrel-like bending experienced some slight changes in the resonance, but not anything major. The cylindrical bending did not experience significant changes. The gain measurements were also measured. These results are shown in Table 5. The horizontal and vertical bends refer to how the antenna was bent (examples shown in Figure 71) while vertical and horizontal gain refer to the orientation of the antenna when the gain measurements were taken.

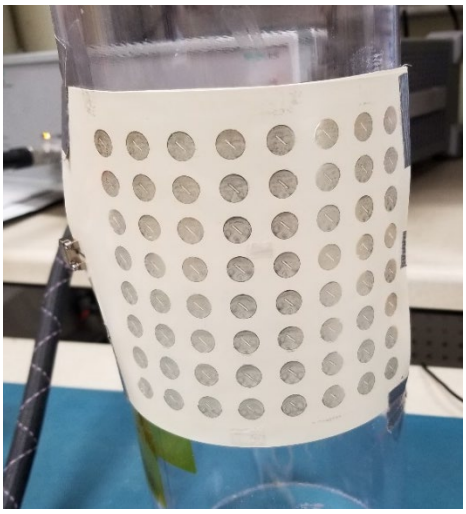

Figure 71: Antenna horizontal bend (left) (image corresponds to horizontal gain measurement; 90° rotated image will represent vertical gain measurement) and vertical bend (right) (image corresponds to vertical gain measurement; 90° rotated image will represent horizontal gain measurement) examples

Table 5: 8x8 uncoated LCP ink antenna gain measurements

Bend	Vertical Gain (dB)	Horizontal Gain (dB)
No Bend	15.1	15.0
Horizontal 2.5in	13.0	11.0
Vertical 2.5in	9.1	9.3
Horizontal 2in	5.3	8.4
Vertical 2in	8.4	8.1

Even though the S11 measurements were not significantly affected by the bending, the gain results were. The vertical and horizontal gain values were fairly close to each other for most of the given bend scenarios. One outlier was the horizontal 2 in. bend, which most likely had a measurement issue.

Figure 72 and Figure 73 show the S11 results for the same 8x8 LCP ink antenna after applying the environmental coating while Table 6 shows the gain results.

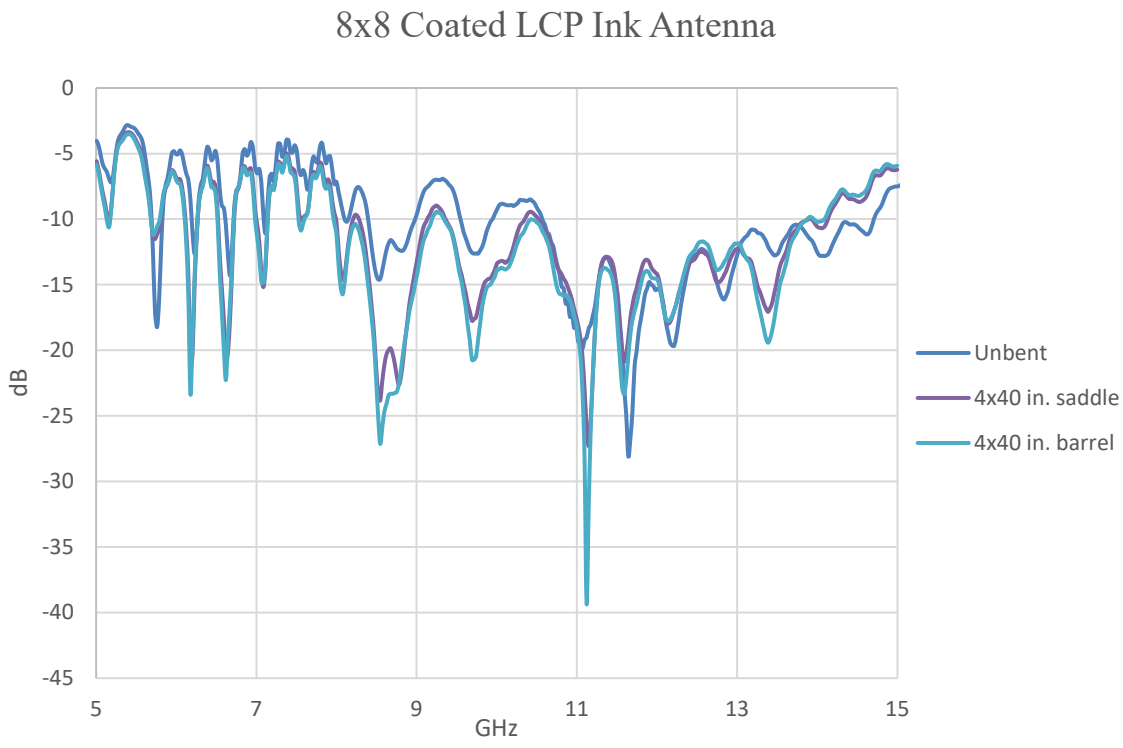

Figure 72: 8x8 coated LCP ink antenna S11 measurements when deformed to saddle and barrel-like surfaces

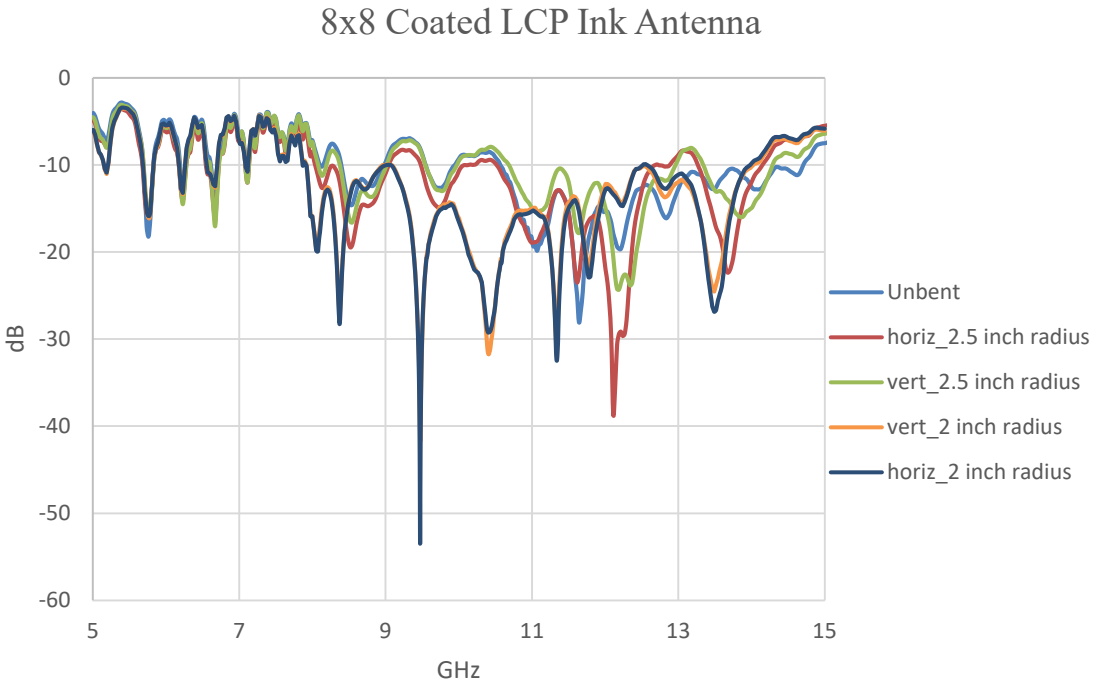

Figure 73: 8x8 coated LCP ink antenna S11 measurements undergoing cylindrical bending

As seen in Figure 72 and Figure 73, there did appear to be some changes between the uncoated and coated antenna S11 results. For the coated antenna, the saddle and barrel-like bends seemed to shift the results downwards slightly, similar to the uncoated antenna. But for the cylindrical bending, there seemed to be more variation between each of the bends. The results for the unbent and 2.5 in. radius bends seemed to have moved up.

Table 6: 8x8 coated LCP ink antenna gain measurements

Bend	Vertical Gain (dB)	Horizontal Gain (dB)
No Bend	15.0	15.0
Horizontal 2.5in	12.8	12.1
Vertical 2.5in	9.5	9.2
Horizontal 2in	8.2	8.2
Vertical 2in	8.1	8.0

As seen in Table 6, after applying the coating the gain measurements did not change much for the antennas.

CHAPTER 8

MATERIAL CHARACTERIZATION

8.1 Nanoindentation Characterization of Printed Silver Ink

To create finite element models of the printed sensors and antennas, mechanical properties of various materials are needed. Although properties for most polymer substrates are available in literature, the properties for printed ink, based on the process temperature profile, are scarce. Thus, the ink was printed using the same printer as used in the flexible substrates and cured using the same temperature profile before employing nanoindentation technique to determine its Young's modulus.. The Poisson's ratio of the ink was assumed to be 0.37 that is close to that of bulk silver [45].

The indentation was performed using a Hysitron Triboindenter. Dimatix™ inkjet printer was used to print 5x5 mm squares of Suntronic™ ink on LCP. The ink was cured in the oven for 200°C for 30 minutes in the same way as the sensors and antennas were fabricated. During indentation, it is necessary to have the thickness of the printed ink at least an order of magnitude greater than the indentation depth so that the substrate properties do not influenced the measured ink properties. Thus, to mitigate the effects of the substrate on the measurement of the ink modulus, eight layers of the ink were printed and cured. Several 5 x 5 mm squares of m layers of ink were printed and cured. A piece of the LCP with one such square was then adhered onto a glass slide using superglue in order to keep the sample flat during the nanoindentation. This sample is shown in Figure 74.

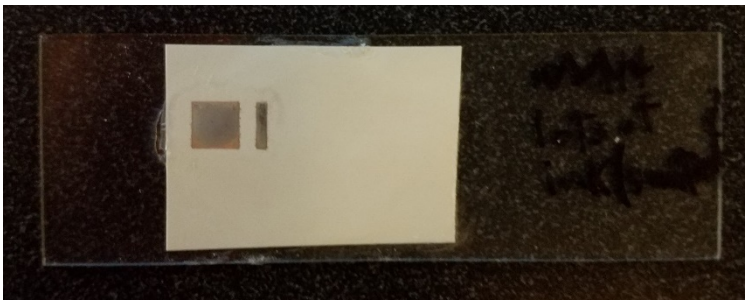

Figure 74: Suntronic™ silver ink sample for nanoindentation

A second printed square of ink that was printed on the same LCP was cross sectioned. An optical microscope was then used to measure the thickness of the ink film. Figure 75 shows the cross-sectioned ink square.

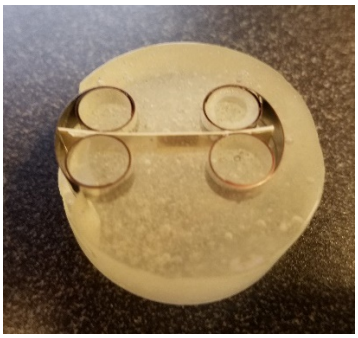

Figure 75: Cross section of eight-layer thick Suntronic™ ink

Figure 76 shows a microscope image of this cross sectioned ink square. The thickness of the ink was found to be between 8 and 9 μm.

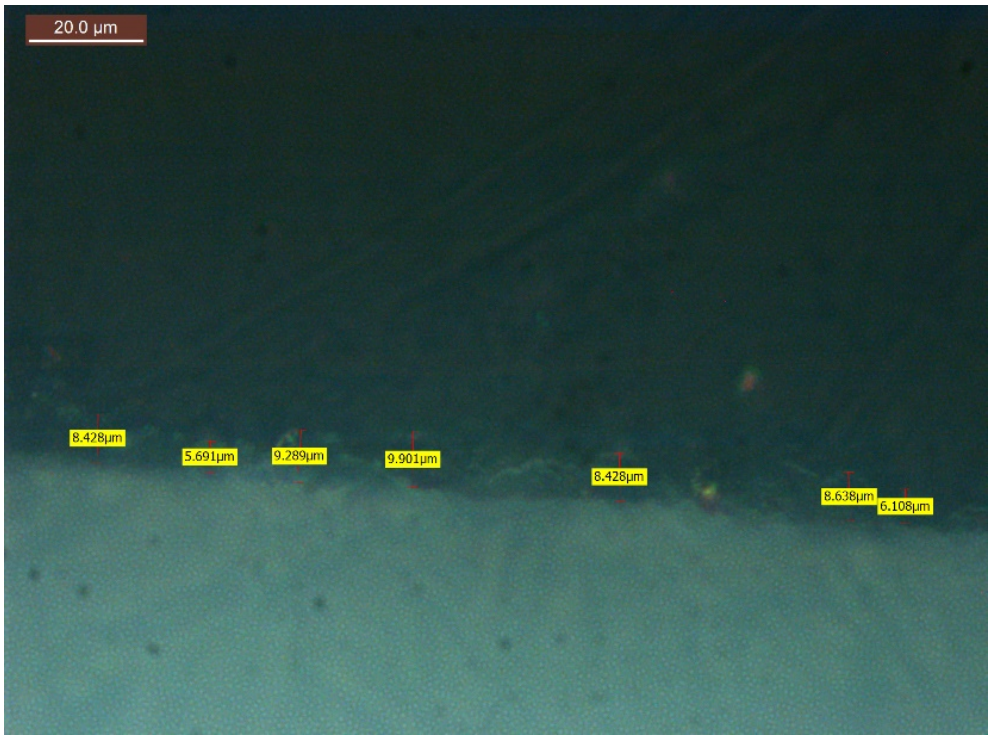

Figure 76: Microscope image of extra thick Suntronic silver ink

8.2 Nanoindentation Results

A conosphereical tip with a one µm radius was used to perform the nanoindentation. Nine different indentations in a 3x3 grid were made on the ink square. Each of the nine indentations were indented to a different depth by giving them different load values. The results of the nine indentations are shown in Figure 77. As seen, the maximum indentation depth was 300 nm which was less than 10% of the thickness of the ink thickness of 8 to 9 µm, and thus, the results produced are expected to be those of the ink, not of the substrate.

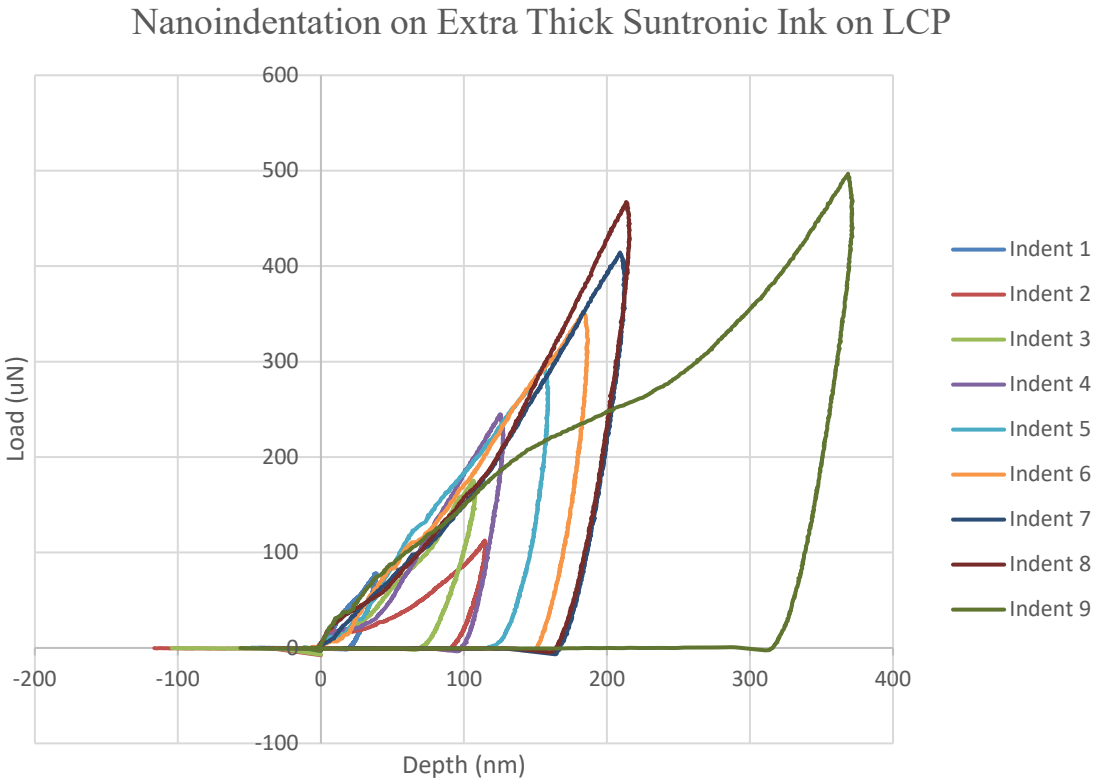

Figure 77: Nanoindentation load and unload vs. indentation depth experimental data for 9 indentations on a sample

Indents two and nine gave results that seemed to be outliers. Figure 78 shows the results with indent two and nine removed.

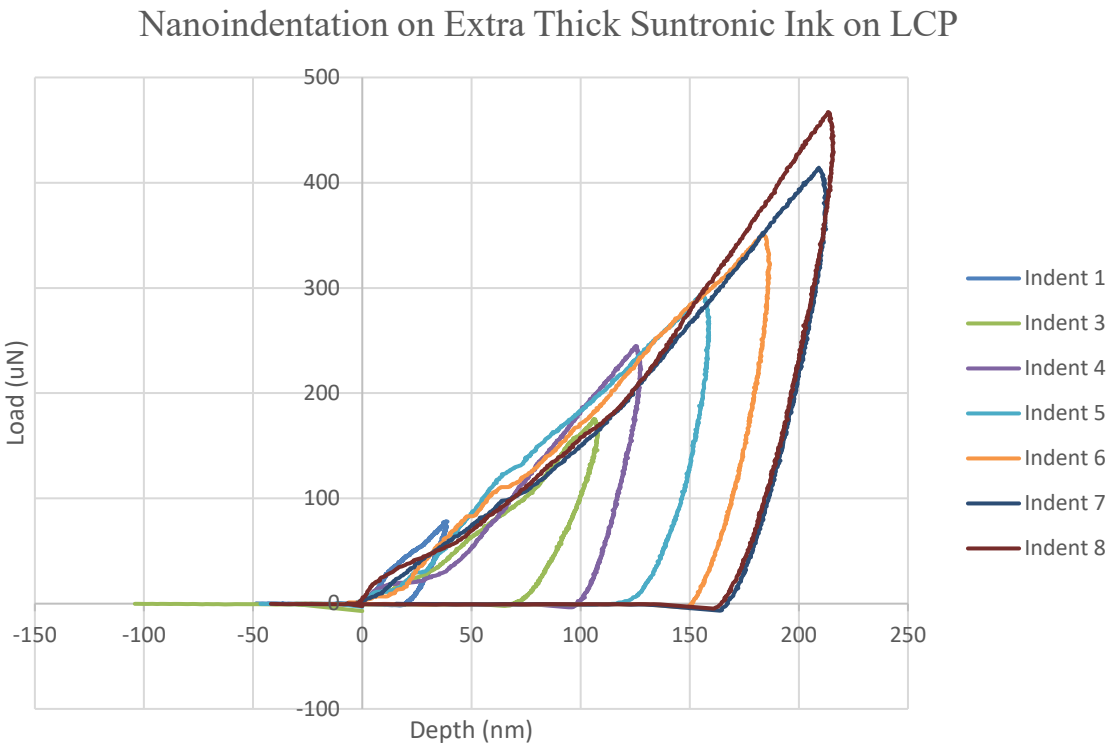

Figure 78: Nanoindentation results with outliers removed

Table 7 shows a summary of the modulus obtained from each indent. The average modulus from all nine indents is 12.42 GPa and the average after removing indentation two and nine is 13.45 GPa.

Table 7: Young's modulus results from nanoindentation

Indent Number	Modulus (GPa)
1	15.34
2	9.35
3	9.43
4	15.10
5	15.77
6	15.60
7	11.50
8	11.42
9	8.30
Average	12.42

CHAPTER 9

NUMERICAL MODELING OF FLEXIBLE SUBSTRATES DEFORMED OVER BIAXIAL SURFACES

9.1 Modeling Overview

Simulations of multiple different loading conditions were conducted for the sensor and antenna geometries. For the sensor simulations, only the Suntronic™ ink printed on LCP geometry was examined. For the antenna simulations, Suntronic™ ink printed on LCP substrate and DuPont™ CBO28 ink printed on Pyralux® substrate were examined. The 2x2 antenna geometry was used in the simulations due to it being smaller than the full sized 8x8 array antenna while still being able to obtain the desired results. Since the areas of interest on the ink structures are present in both sizes of antennas, the 2x2 antenna geometry is the better choice.

9.2 Material Modeling

The sensor material combination chosen was the Suntronic™ ink printed on LCP substrate. The antenna consisted of two different sets of materials: Suntronic™ ink printed on LCP substrate and DuPont™ CBO28 ink printed on Pyralux® substrate. Also, the effect of an environmental coating, DuPont® Elvax™, on the stresses seen in the ink structures of the antenna was examined.

Isotropic elastic material models were used in the simulations. A modulus of 13.5GPa was used for the silver ink from the nanoindentation experiments described

earlier. Poisson's ratio was assumed to be the same as bulk silver at 0.37. The LCP and Kapton® material properties were taken from the products' datasheets [11, 46]. The fixtures were modelled as extremely rigid with a modulus of elasticity of 200 GPa so that the stiffness would be much greater than the sensor and the deformation of the fixtures would be negligible. This high modulus of elasticity is intended to ensure that there is no deformation in the fixtures. Table 8 shows a summary of the material models used.

Table 8: Material Properties

Material	Modulus (GPa)	Poisson's Ratio
Rogers Ultralam® 3850 LCP	3.4	0.30
Kapton®	2.5	0.34
Suntronic™ silver ink	13.5	0.37
Copper	110.0	0.34
Rigid fixtures	200.0	0.30
Elvax® 250	0.019	0.33

9.3 Geometric Modeling

3D geometry models for the sensor and the antenna were created in Autodesk® Inventor. The ink structure in Figure 80 is 8 µm thick to represent the thickness after curing in the oven. The substrate was modeled as a 50 x 20 mm rectangle 117.8 µm (7 mils) thick. Figure 79 shows a CAD model of the sensor, while Figure 80 shows a close-up side view.

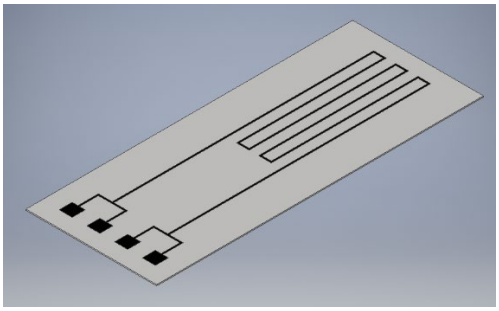

Figure 79: CAD model of Suntronic™ ink on LCP sensor

Figure 80: Close up side view of CAD model Suntronic™ ink on LCP

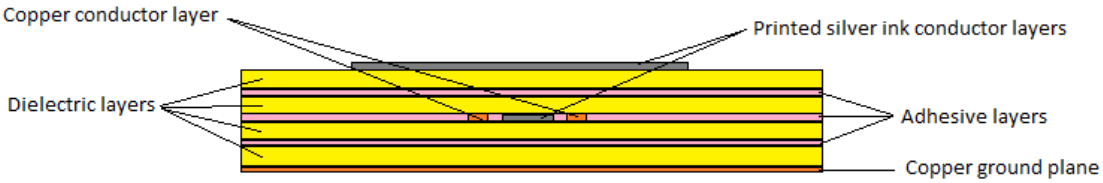

Figure 81: Cross-section view of antenna layers

The antenna model consisted of a copper ground plane, two LCP layers, and two ink layers. The ink was modeled as 5 µm thick. The two LCP layers represent the physical antenna's bottom two and top two LCP layers respectively. Each of the LCP layers was

modeled 355.6 μm (14 mils) thick and it was assumed the LCP layers were perfectly bonded together. Figure 81 shows a cross-section view of the antenna layers. The thickness of the adhesive used was assumed to be negligible and the layers were treated as completely bonded together. The planar dimensions of the antenna were 42.042 mm in length and 32.91 mm in width. Figure 82 and Figure 83 show the full and close-up side views of the CAD model.

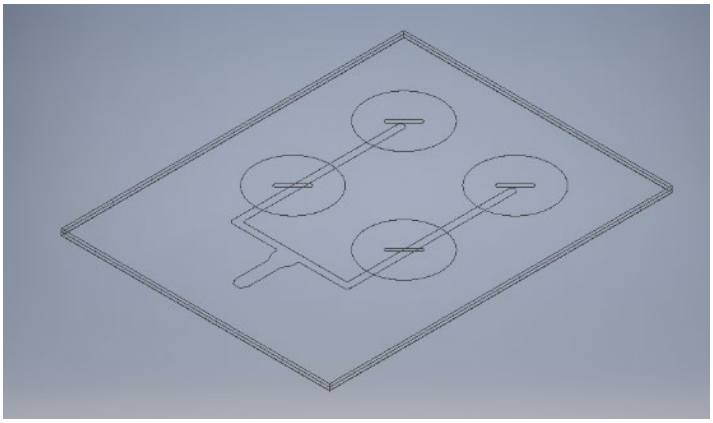

Figure 82: CAD model of 2x2 antenna with Suntronic ink on LCP

Figure 83: Close-up side view of CAD model of 2x2 antenna with Suntronic™ ink on LCP. Top to bottom: top-layer array antenna in silver ink, top LCP dielectric, middle-layer ink feeder lines, bottom LCP dielectric, and copper ground plane

A similar geometry was made for the 2x2 antenna using Kapton® instead of LCP for the dielectric layers and CBO28 ink instead of the Suntronic™ ink. The geometry

stayed the same except the dielectric layers were 508 µm (20 mils) thick and the ink was 30 µm thick.

In addition, the effect of an environmental coating on the stresses seen by the top ink layer was investigated. An 80 µm coating layer was added to the antenna geometry with LCP and Suntronic™ ink. Figure 84 and Figure 85 show the antenna with the coating and a close side view of the top section of the antenna with the coating.

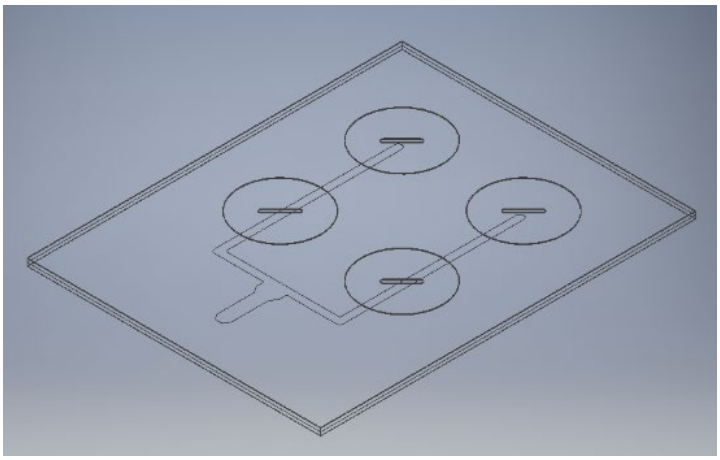

Figure 84: LCP and Suntronic™ ink 2x2 antenna with 80 µm coating

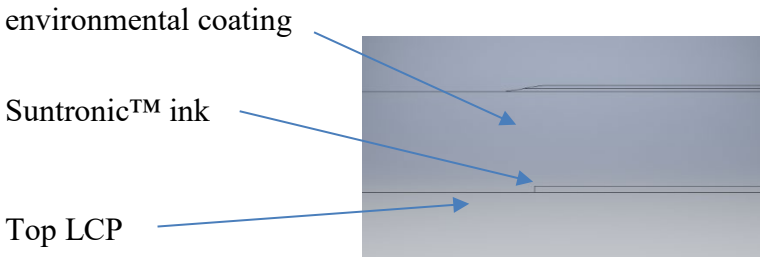

Figure 85: Close up side view of antenna coating on top layers of LCP and Suntronic™ ink. Top to bottom: Elvax® 250 environmental coating, Suntronic™ ink, and top LCP dielectric layer

To apply the desired deformations to the structures and simulate the actual test conditions, simplified models of the saddle and dome fixtures were used. 0.254 mm (0.01 in.) thick sections of the curved areas of the fixtures were created for the simulations. These sections were trimmed to be only as large as the area of the sensor or antenna that they were being used to deform. This was done to minimize the number of elements used in the simulations. The sensor and antennas were placed in between these top and bottom fixtures. The fixtures were placed at a height where they were slightly above and below the sensor and antennas. Figure 86 and Figure 87 show examples of the sensor with 4 in. saddle-like fixtures and the LCP antenna with 4 x 40 in. saddle-like fixtures.

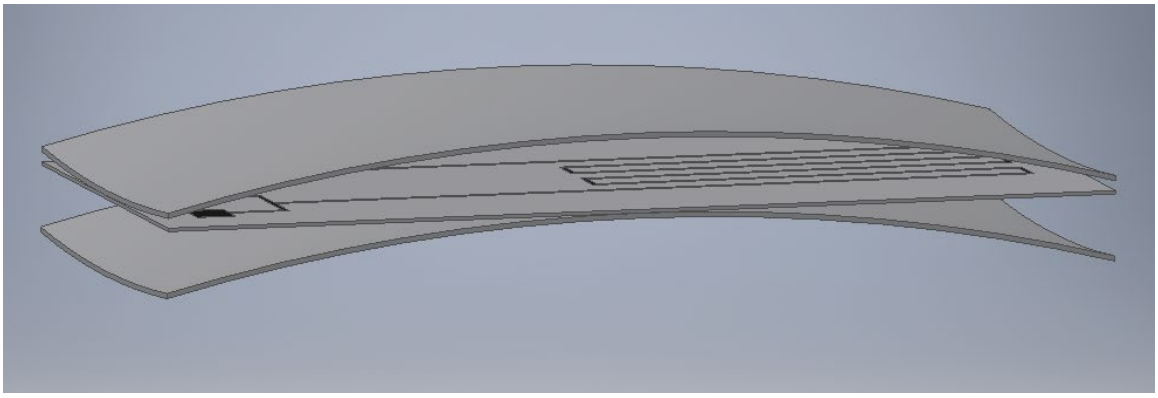

Figure 86: Sensor with 4 x 4 in. saddle-like fixtures

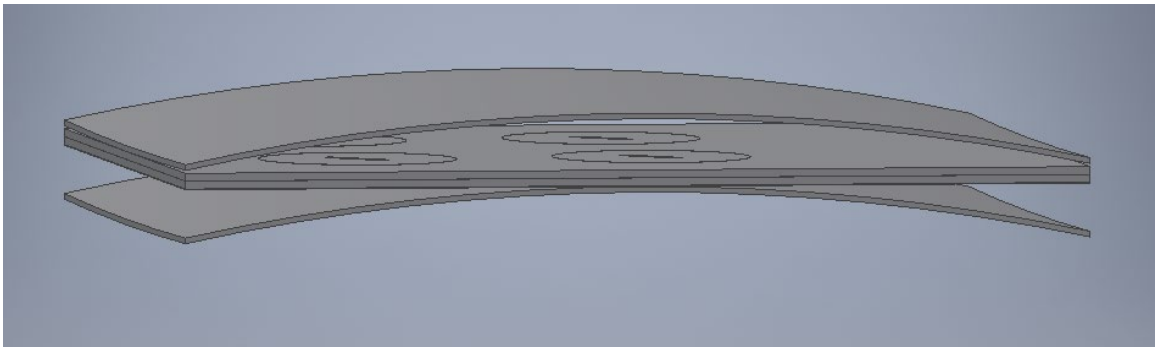

Figure 87: 2x2 LCP antenna with 4 x 40 in. saddle-like fixtures

The simulations were carried out in ANSYS® Workbench 17.1. The sensor was meshed with 20-node 3D brick elements for the ink structure and 4-node shell elements for the substrate. The fixture was also meshed with 20-node 3D brick elements. A sweep meshing method was used and the ink structure was meshed three layers thick. Fully bonded contact elements were used between the ink and the substrate. In other words, the ink was assumed to be fully bonded to the underlying substrate. Also, three frictionless contact element sets were used between: bottom of substrate to bottom fixture, top of substrate to top fixture, and top of ink to top fixture. These contact elements were present to ensure that the substrate or ink would not penetrate the rigid fixtures or vice versa. Figure 88 shows the mesh of the sensor with the 4 x 4 in. saddle-like fixtures

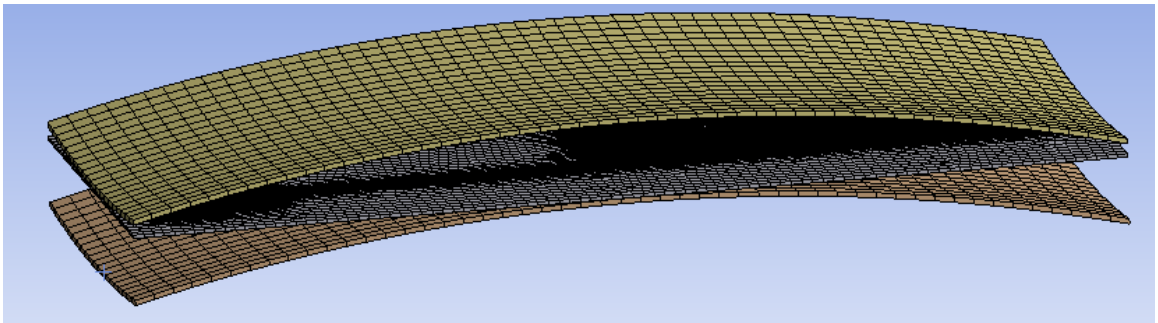

Figure 88: Finite-Element Mesh of LCP Substrate with Printed Ink Placed in-between Fixtures

The antenna was meshed entirely with solid elements. Twenty-node brick elements were used for the fixtures, ground plane, and ink structures. The fixtures and ground plane geometries were meshed one-element thick while the ink structures were meshed three-elements thick. The dielectric and coating structures were meshed with 10-node

tetrahedrons. Figure 89 shows the mesh of the 2x2 LCP antenna with the 4 x 40 in. saddle-like fixtures.

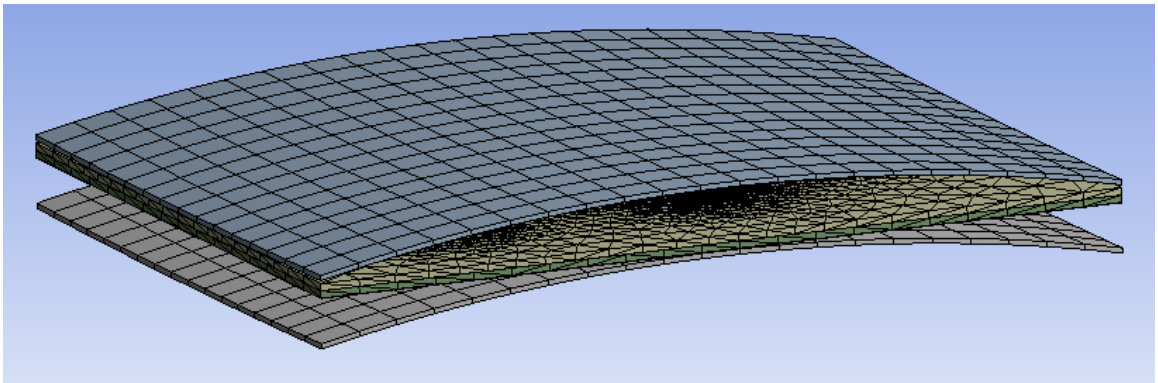

Figure 89: Mesh of LCP 2x2 antenna with 4 x 40 in. saddle-like fixtures

9.4 Boundary Conditions

Conforming the sensors and antennas to the desired shape was obtained by moving the top fixture downwards toward the bottom fixture and sandwiching the sample. This method of applying the deformation simulates the actual physical test loading. The nodes along the bottom surface of the bottom fixture were fixed in place while the nodes on the bottom surface of the top fixture (inside) were give displacement downwards. Multiple load steps were used with each one displacing the top fixture 0.1 mm. The total vertical displacement was equal to the initial spacing between the fixtures minus the thickness of the sensor or antenna. In order to keep the sensor or antenna sliding out from in between the fixtures or rotating, three nodes along one of the sides were given in plane displacements of zero while being free to move vertically. Figure 90 shows the geometry of the antenna with 4 x 40 in. saddle-like fixtures with the boundary conditions. In Figure 90, A is the fixed nodes on the bottom side of the bottom fixture, B is the nodes on the

bottom side of the top fixture that are displaced downwards, and C is the group of nodes that are only allowed to move vertically to prevent sample sliding.

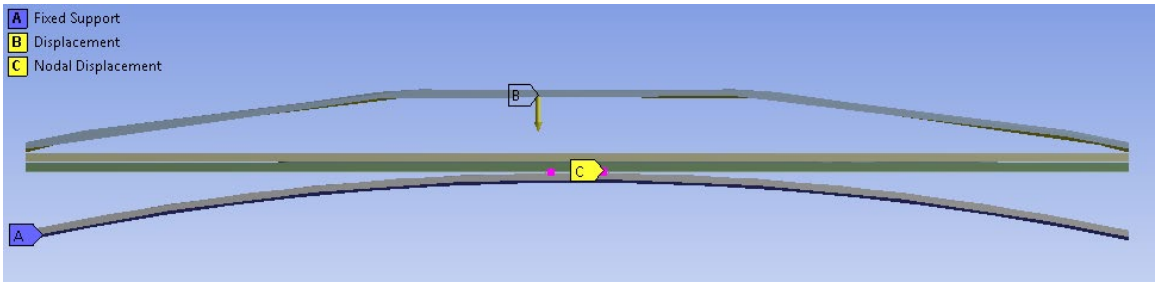

Figure 90: 2x2 antenna with 4 x 40 in. saddle-like fixtures boundary conditions. A) Fixed nodes on bottom surface of bottom fixture, B) Vertically displaced nodes on bottom surface of top fixture, and C) Nodes on antenna allowed to only be displaced vertically.

9.5 Simulation Results

9.5.1 Sensor Results

The sensor's *X* (length) normal strains (ε_{xx}) are shown in Figure 91 and Figure 92 and the *Y* (width) normal strains (ε_{yy}) are shown in Figure 93 and Figure 94 below for the 4 in. dome bend.

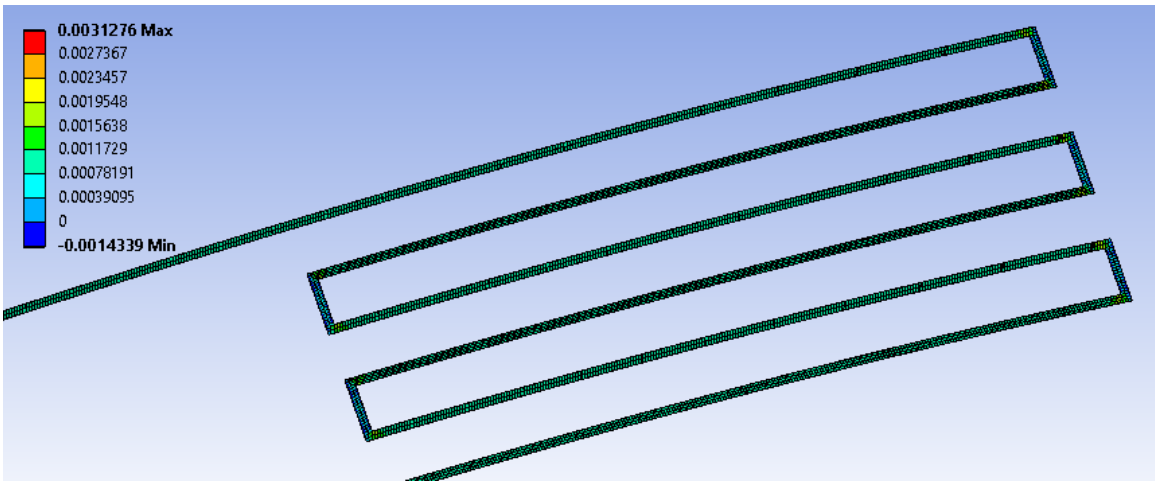

Figure 91: Length-direction normal strain (ε_{xx}) for sensor deformation in 4 in. dome fixtures

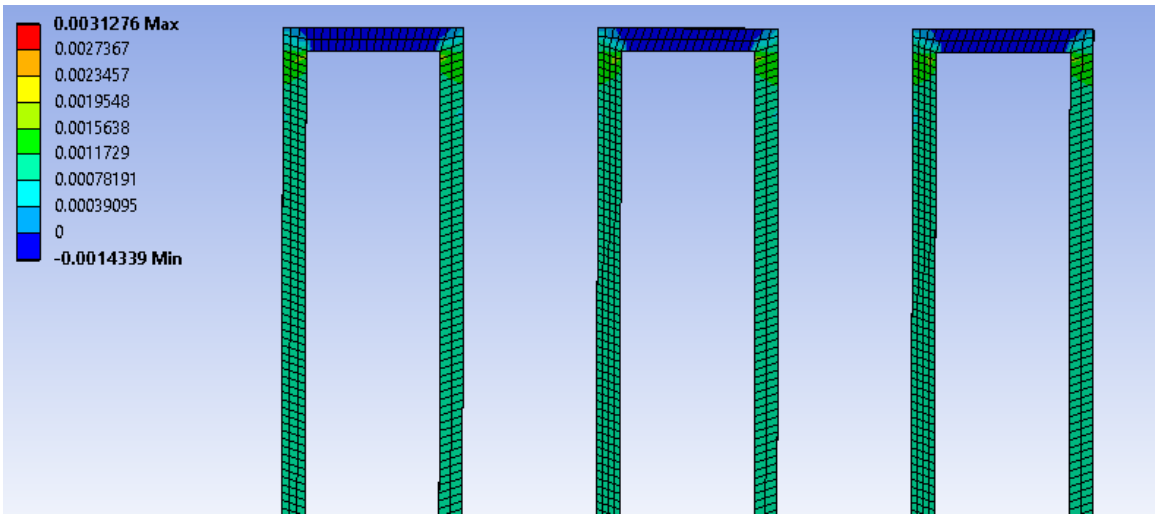

Figure 92: Close-up view of sensor deformation with length-direction normal strain (ε_{xx}) contours in 4 in. dome fixtures

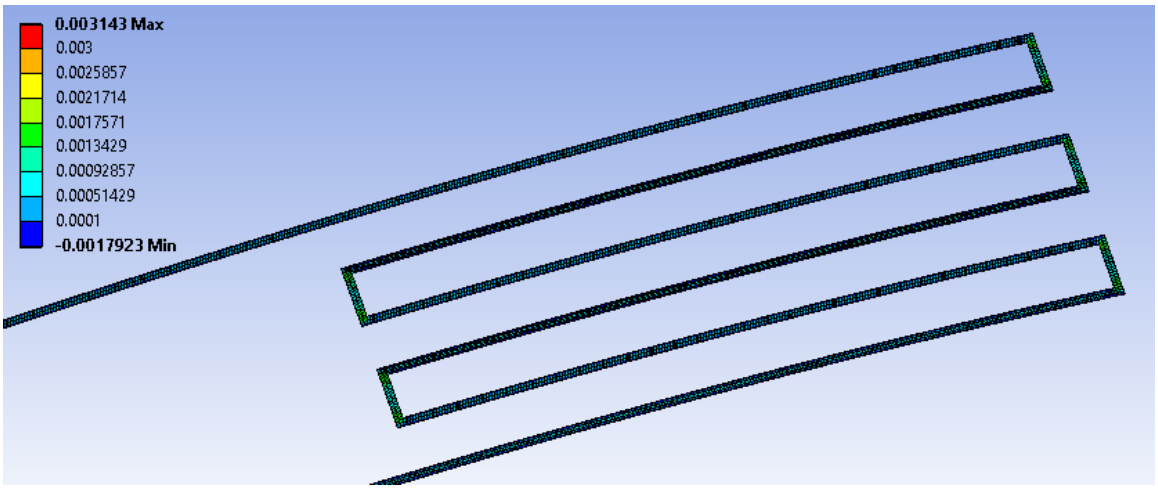

Figure 93: Width-direction normal strain (ε_{yy}) for sensor deformation in 4 in. dome fixtures

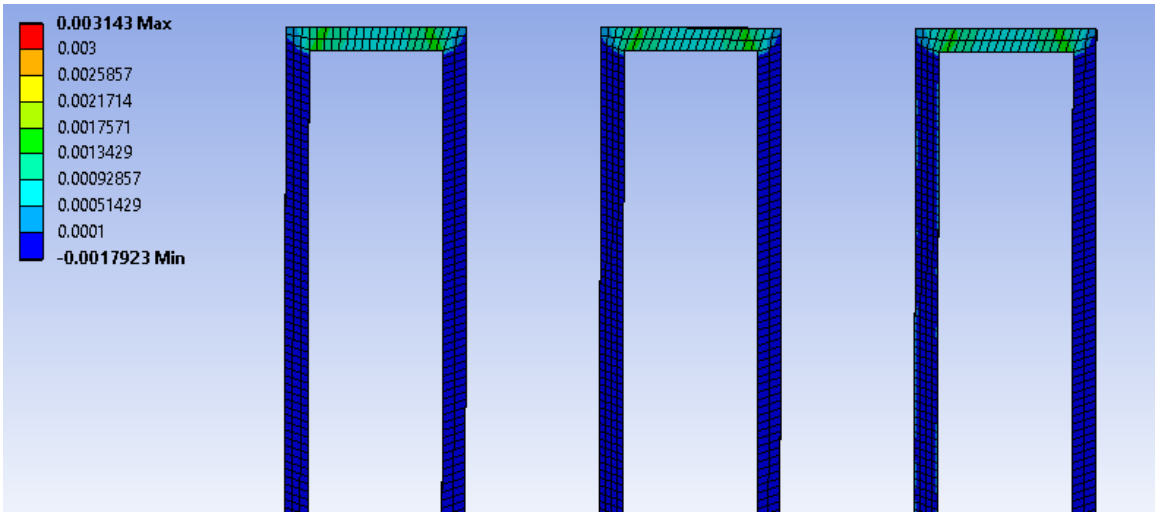

Figure 94: Close-up view of sensor deformation with width-direction normal strain (ε_{yy}) contours in 4 in. dome fixtures

The sensor's *X* (length) normal strains (ε_{xx}) are shown in Figure 95 and Figure 96 and the *Y* (width) normal strains (ε_{yy}) are shown in Figure 97 and Figure 98 below for the 4 in. saddle-like bend.

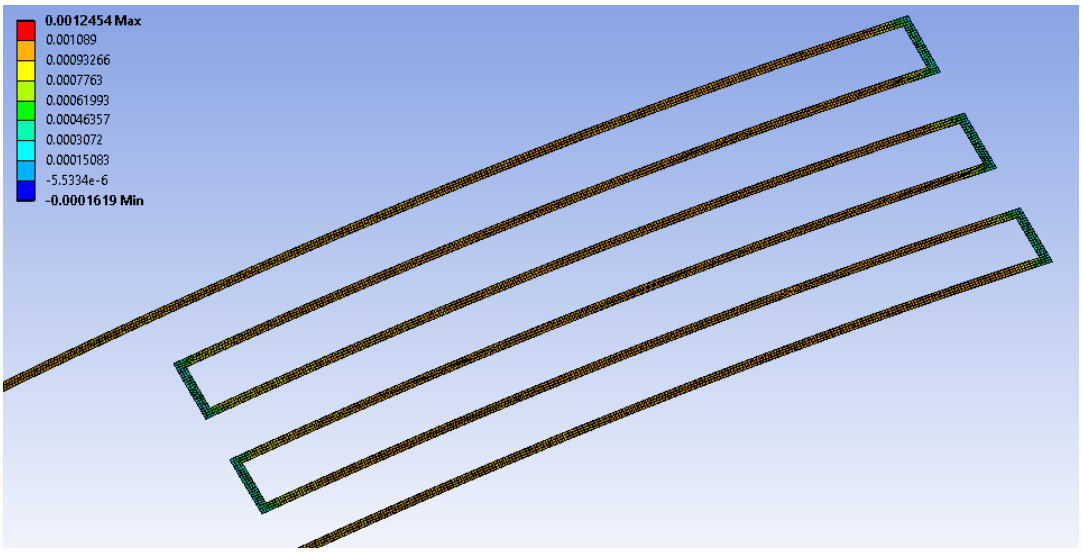

Figure 95: Length-direction normal strain (ε_{xx}) for sensor deformation in 4 in. saddle-like fixtures

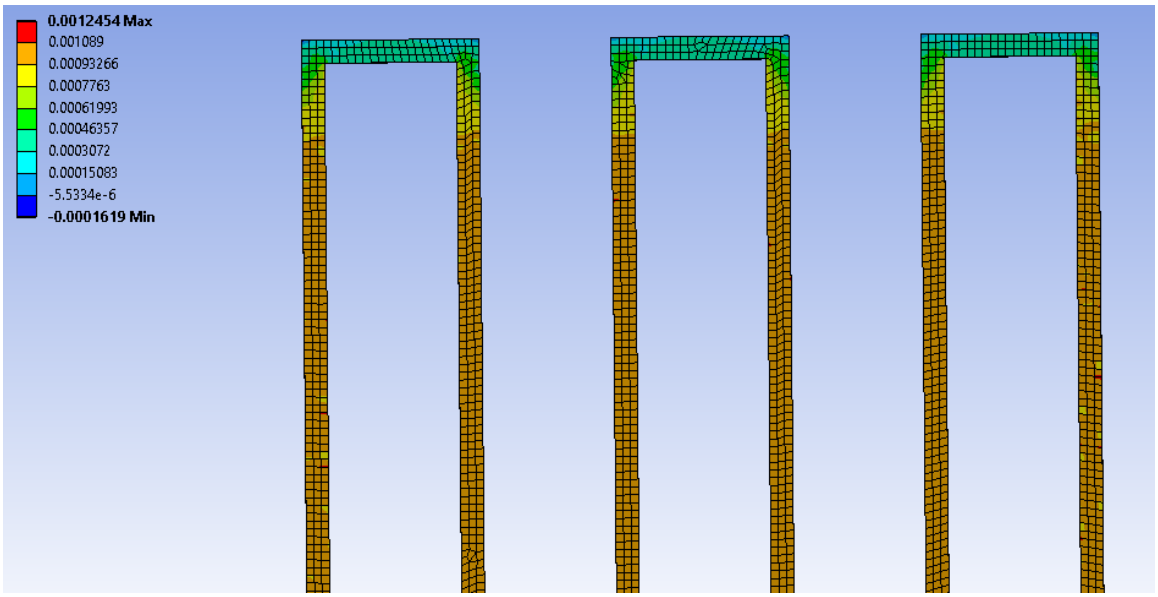

Figure 96: Close-up view of sensor deformation with length-direction normal strain (ε_{xx}) contours 4 in. saddle-like fixtures

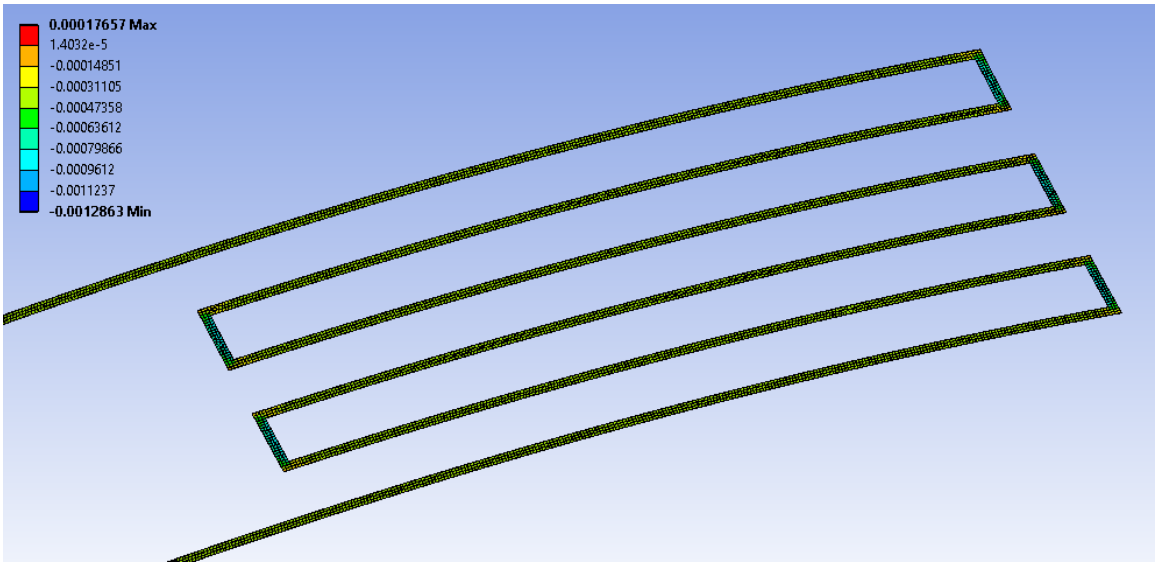

Figure 97: Width-direction normal strain (ε_{yy}) for sensor deformation in 4 in. saddle-like fixtures

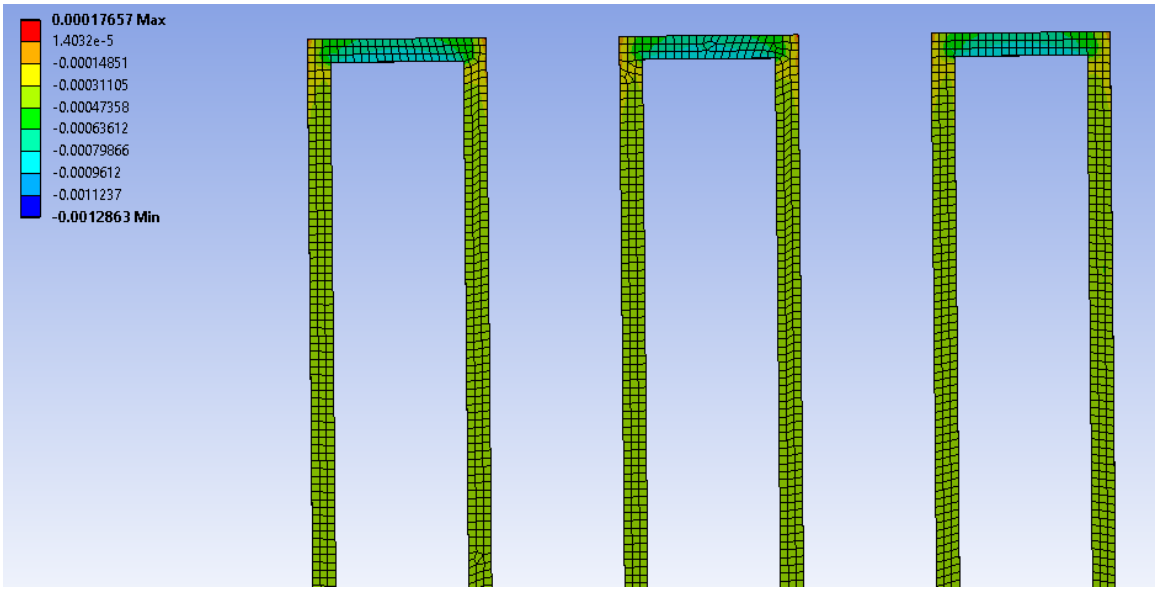

Figure 98: Close-up view of sensor deformation with width-direction normal strain (ε_{yy}) contours in 4 in. saddle-like fixtures

The maximum principal and shear stresses can be examined to predict the direction of the cracks that develop during cyclic deformation. The elements used and maximum principal and shear stresses of the corner location of the Suntronic ink sensor on the LCP substrate in 4 x 4 in. saddle-like fixtures are shown in Figure 99 and Figure 100 while those at the side location are shown in Figure 101 and Figure 102.

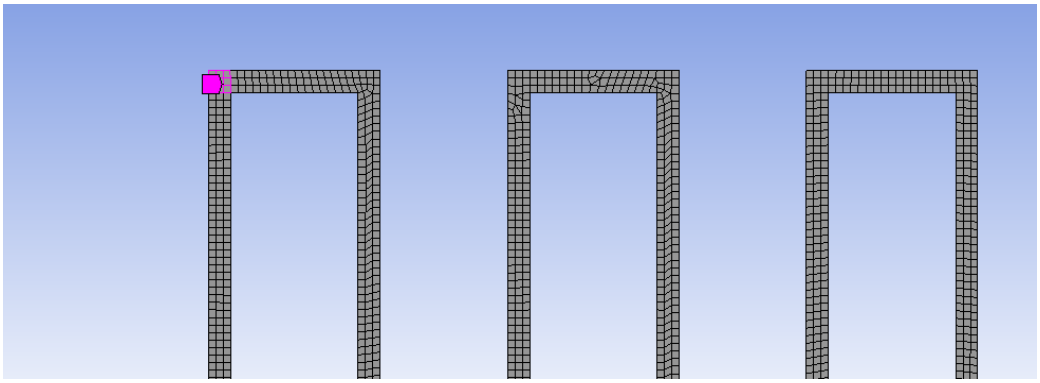

Figure 99: SEM corner location elements

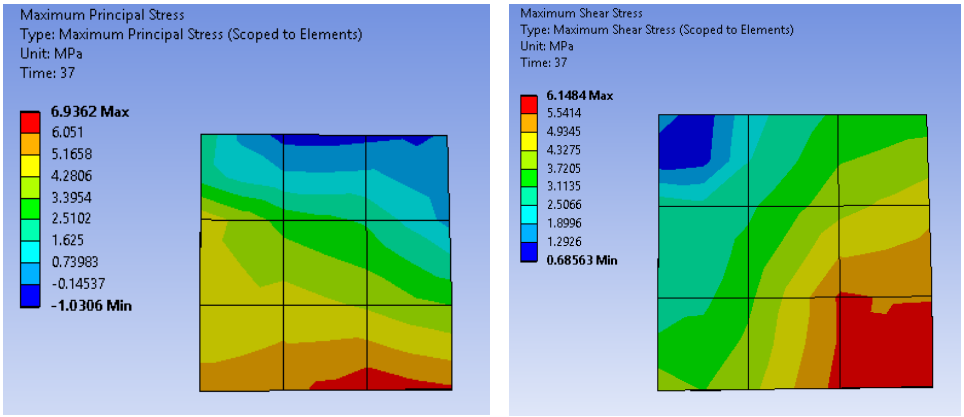

Figure 100: Maximum principal and shear stresses in SEM corner location

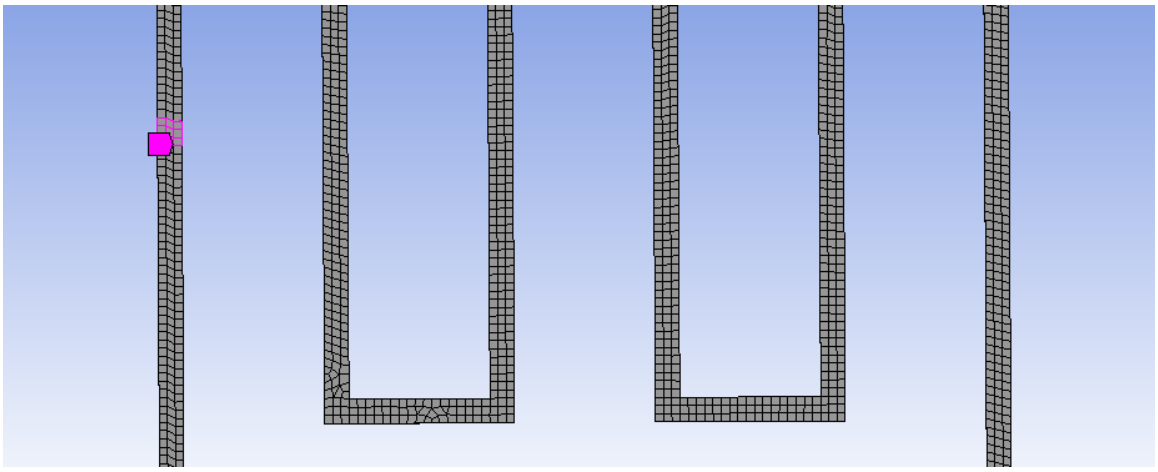

Figure 101: SEM side location elements

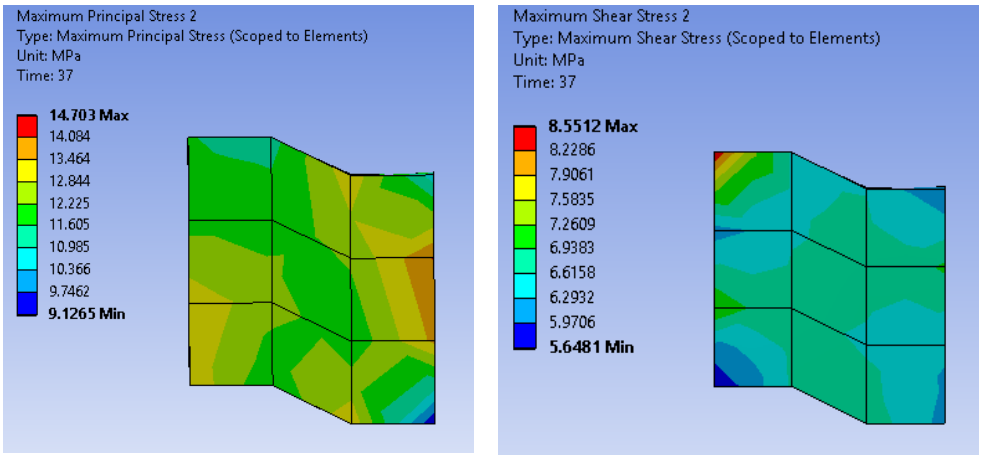

Figure 102: Maximum principal and shear stresses in SEM side location

Figure 103 shows the maximum principal stress plot at the corner location next to the SEM imaged cracks at 300 cycles. As seen, the cracks occur in locations where the stresses are maximum.

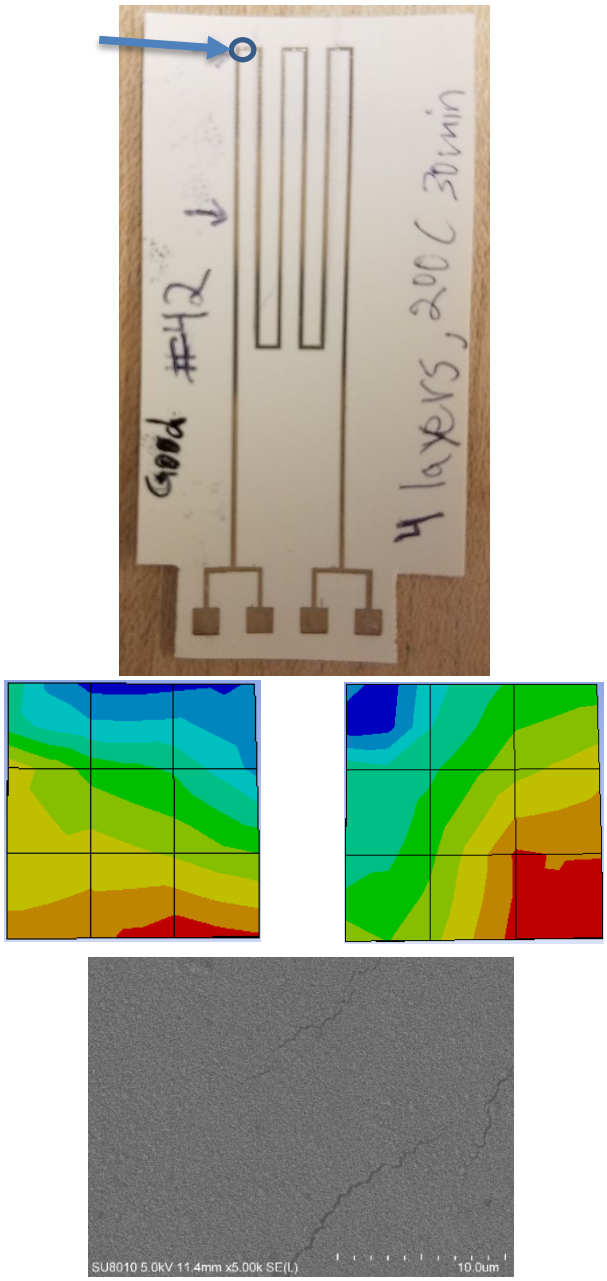

Figure 103: SEM corner location on sample (top), maximum principal stress (middle left), maximum shear stress (middle right), and cracks at 300 cycles (bottom)

Likewise, the maximum principal and shear stress plots with the cracks at the side location at 300 cycles are shown in Figure 104.

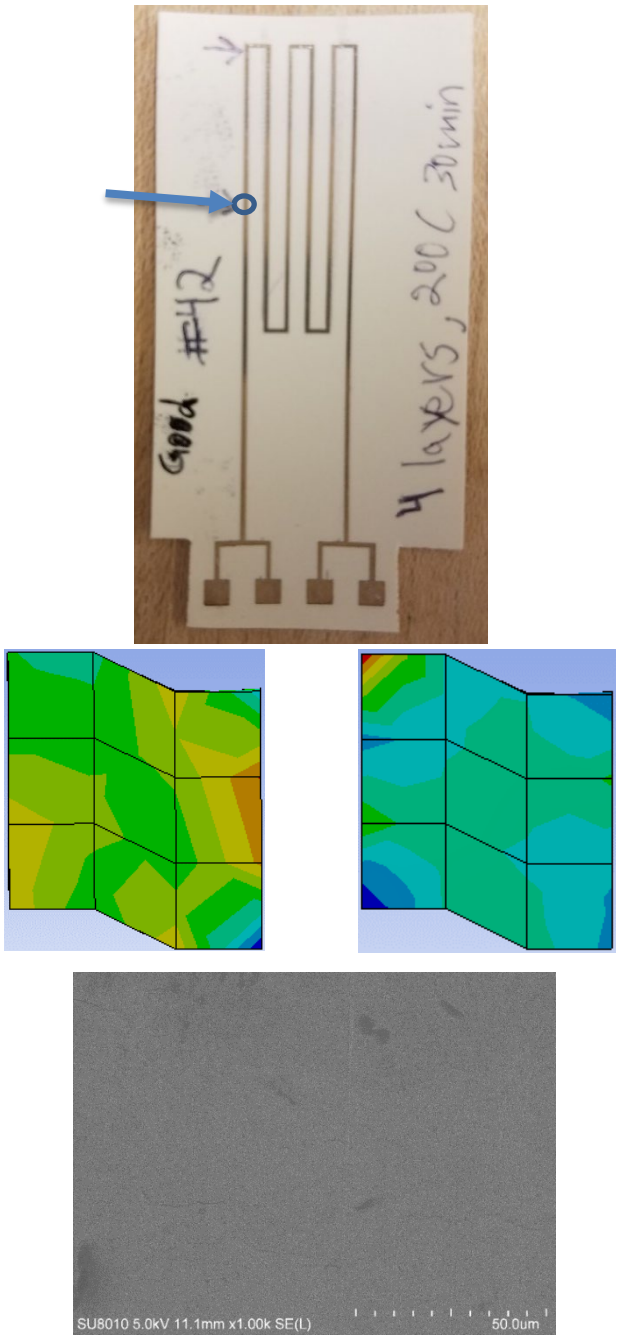

Figure 104: SEM side location on sample (top), maximum principal stress (middle left), maximum shear stress (middle right), and cracks at 300 cycles (bottom)

At the side location, the cracks appear to be propagating perpendicular to the trace direction. This is expected due to the trace experiencing tension along its length direction and compression in the width direction.

The theoretical strains in the ink structure can be calculated using (3) and (4) below. The *x* direction represents the lengthwise direction and *y* represents the width direction.

$$\varepsilon_{xx} = \frac{d}{\rho_x} - \nu \frac{d}{\rho_y} \tag{3}$$

$$\varepsilon_{yy} = \frac{d}{\rho_y} - \nu \frac{d}{\rho_x} \tag{4}$$

Where d is the distance from the neutral axis, ρ_x is the radius of curvature in the length direction, ρ_y is the radius of curvature in the width direction, and ν is the Poisson's ratio.

The theoretical strains for the saddle and dome shapes simulated are shown in Table 9

Table 9: Theoretical strain of printed silver ink on LCP

Deformation Shape	$\boldsymbol{\varepsilon_{xx}}$	$\boldsymbol{\varepsilon_{yy}}$
4-in. dome	0.000489	0.000489
4 in. saddle	0.00106	-0.00106

The strains in the 4 in. dome simulations (about 0.12%) appear to be higher than the theoretical strains (0.05%). One possible reason for this is that the out-of-plane (*z* axis)

compression of the silver ink by the top fixture is not taken into consideration in the analytical formulation. Figure 105 shows the out-of-plane strain (ε_{zz}) of the silver ink and Figure 106 shows the length-wise normal (ε_{xx}) strain, and it is seen that their magnitudes are very close to each other. As seen, the negative strain in the out of plane direction appears to be of the same order of magnitude as the tensile in-plane strain. The Poisson effect when compressing the ink thus causes an increase in the in-plane strain.

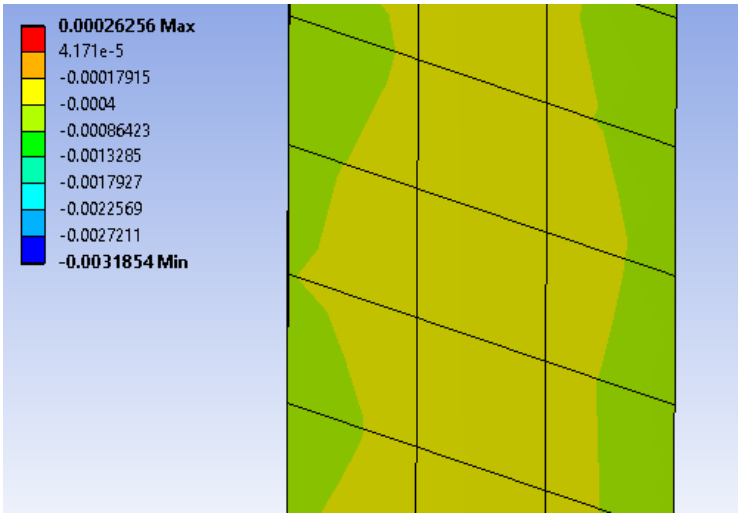

Figure 105: Sensor 4 in. dome bend out of plane strain

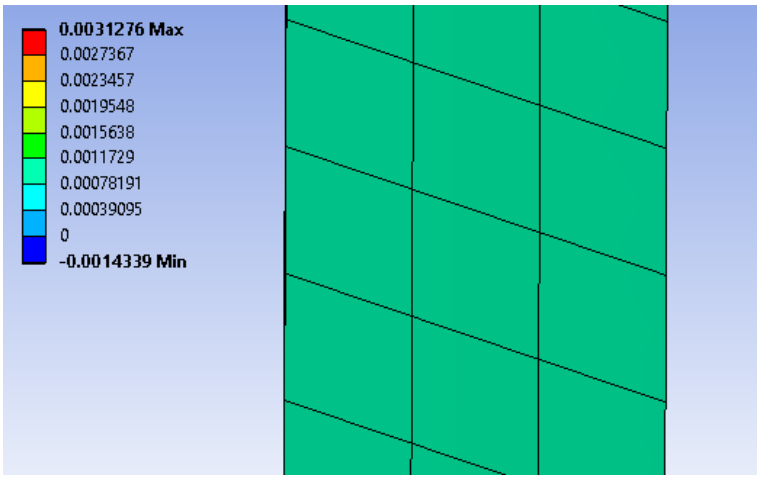

Figure 106: Sensor 4 in. dome bend very close length strain in middle of trace

9.5.2 Antenna Results

Mechanical failure of the antenna is expected to be in the top ink structures due to their farthest distance from the neutral axis of the deformation. There will be a stress concentration at the curved areas of the slots in the top ink patches. X (4 in. radius) and Y (40 in. radius) normal strain values are shown for the top ink patches in Figure 107 and Figure 108. Figure 109 and Figure 110 give close-up views of these strains at one of the slots of the patch at the front left of the antenna.

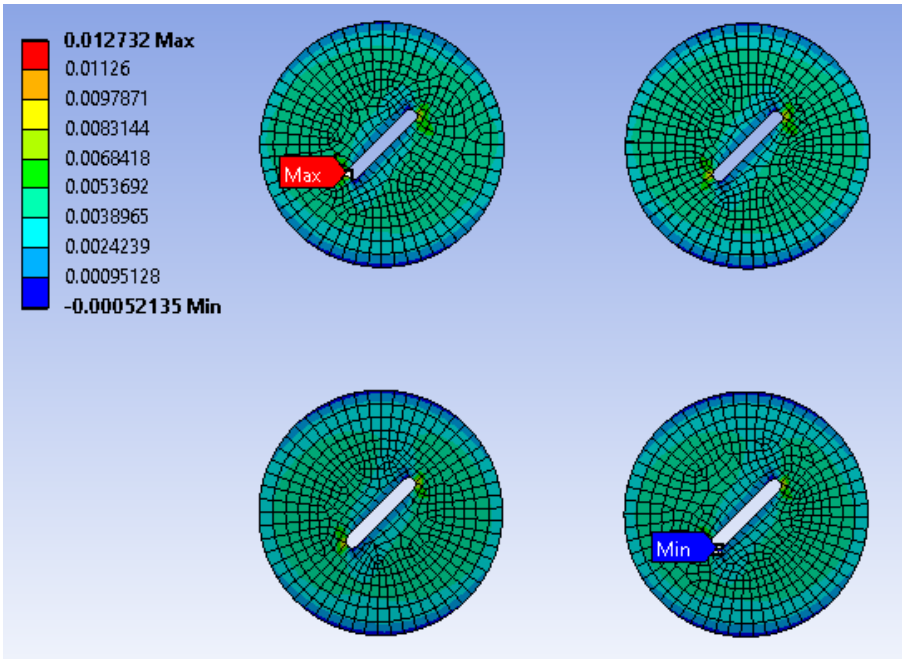

Figure 107: LCP antenna top ink strain (ε_{xx}) for deformation in 4 in. x 40 in. saddle-like fixtures

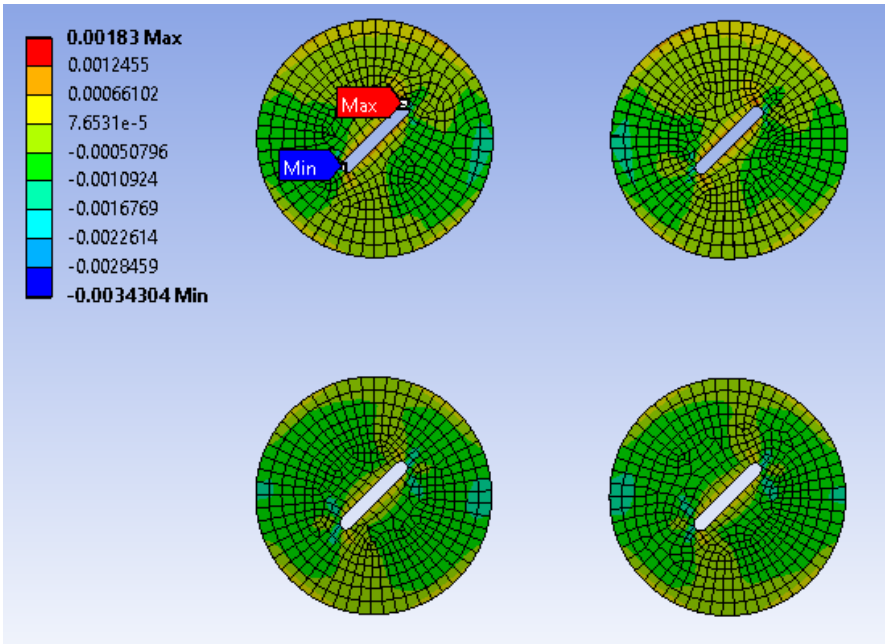

Figure 108: LCP antenna top ink strain (ε_{yy}) for deformation in 4 in. x 40 in. saddle-like fixtures

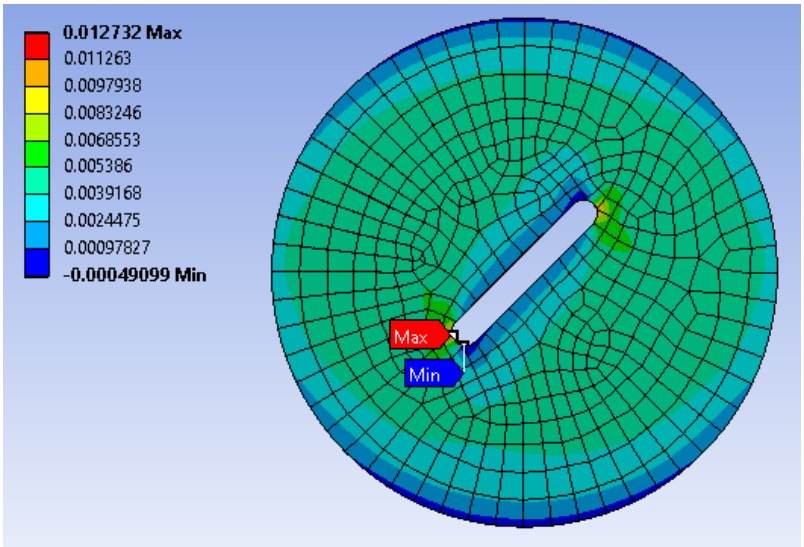

Figure 109: Close-up view of LCP antenna top ink strain (ε_{xx}) for deformation in 4 in. x 40 in. saddle-like fixtures

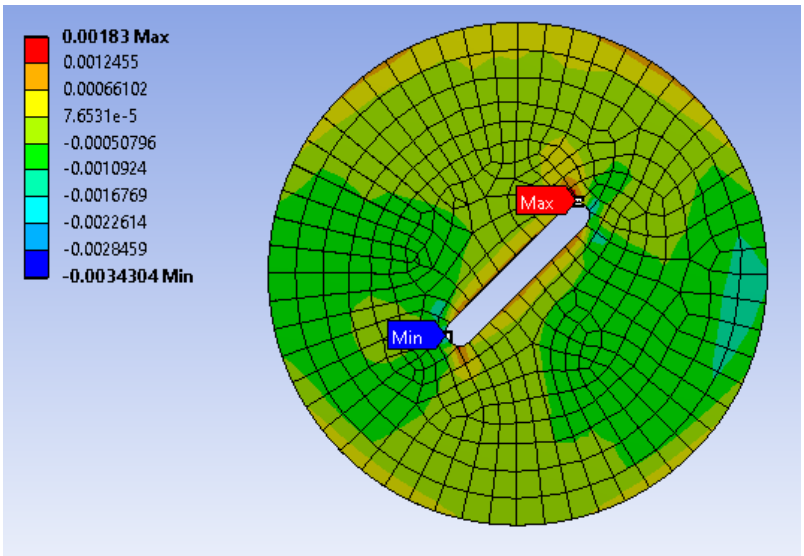

Figure 110: Close-up view of LCP antenna top ink strain (ε_{yy}) for deformation in 4 in. x 40 in. saddle-like fixtures

Results of the same saddle bend on the antenna with the environmental coating are shown in Figure 111 and Figure 112. The presence of the coating resulted in a decrease of 18% in the length direction strain and a decrease of 17% in the width direction strain.

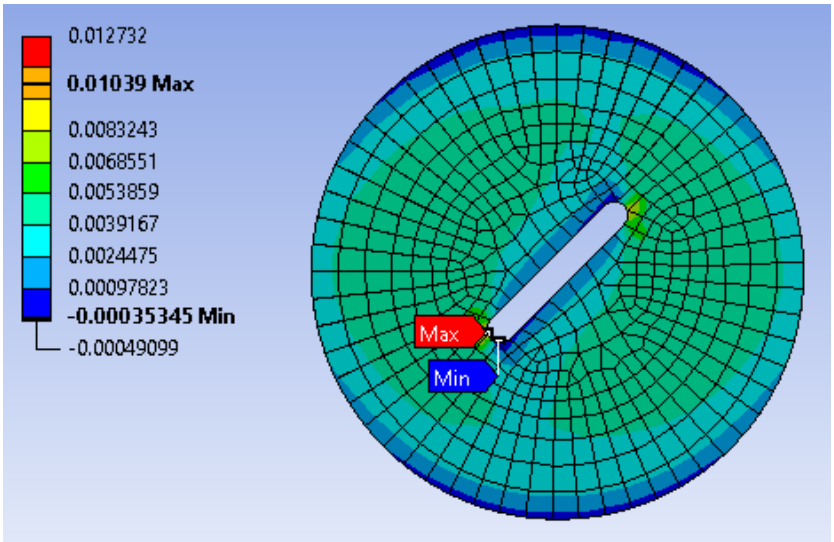

Figure 111: Close-up view of LCP antenna with coating top ink strain (ε_{xx}) for deformation in 4 in. x 40 in. saddle-like fixture

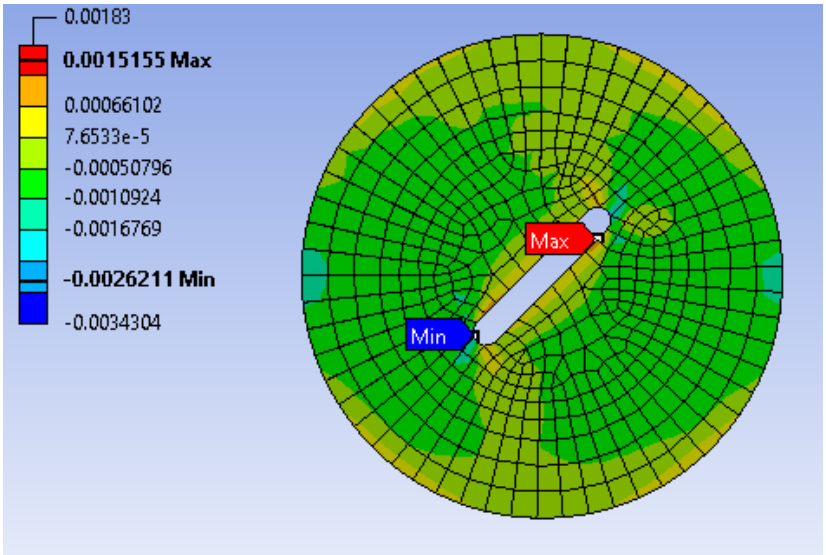

Figure 112: Close-up view of LCP antenna with coating top ink strain (ε_{yy}) for deformation in 4 in. x 40 in. saddle-like fixture

The strains seen in the silver ink patches at the top of the antenna will occur at the inside curves of the slots. The curved slots will create a concentration and are expected to be the first location where cracks form when the antenna is deformed. Due to the geometry of the slot, a simple stress concentration factor of a hole was used [47]. The strains expected in the top silver ink are calculated from (5) and (6) where the X and Y

strains are initially found using (3) and (4). The stress concentration factor is calculated with (7).

$$\varepsilon_{xx,max} = K_t \varepsilon_{xx} \tag{5}$$

$$\varepsilon_{yy,max} = K_t \varepsilon_{yy} \tag{6}$$

$$K_t = 3 - \frac{\sigma_{yy}}{\sigma_{xx}} = 3 - \frac{\varepsilon_{yy}}{\varepsilon_{xx}} \ (Elastic\ model) \tag{7}$$

The *X* strain is calculated to be 0.0130 which is close to the simulation result of 0.0127. The *Y* strain value is calculated to be -0.00590 which is a considerably higher magnitude than the simulation result of -0.00343.

CHAPTER 10

CONCLUSION, CONTRIBUTIONS, AND FUTURE WORK

10.1 Conclusion

Additive 3D printing can be utilized to quickly fabricate fixtures with many different complex surfaces to use in testing flexible electronics. These fixtures can easily be adapted to fit a universal test machine and test many different flexible electronics all on the same test apparatus. With appropriate access to the contact pads, various electrical characteristics of the flexible electronic samples can be assessed. A downside of the discussed test in this thesis is that the fixtures need to be fabricated, and the fabrication can be time consuming and expensive if one needs to test on many different surfaces. Also, the samples undergo mostly bending and very little stretching during testing. Another test that can be used for biaxial stretching is the Bladder Inflation Stretch test. This other test is currently in development.

Novacentrix® Metalon® JS-B25P air-dried silver ink on PET sensors were tested on a 4 in. dome structure. As the ink structure was put in tension, the resistance increased and then decreased when the structure returned to its original shape. The resistance of the ink sensor decreased for about 50 cycles, and then increased from about 50 to 100 cycles. Significant interparticle cracking in the printed ink was observed in SEM images. This cracking is believed to be the reason for the increase in resistance. The initial decrease in resistance with cycling is believed to be from the particles rubbing together during as the structure is strained. As the particles rub together, the capping agent on the individual

particles is further removed, increasing the electrical contact between the particles. As long as no significant cracking is present, this rubbing together of the particles causes the resistance to decrease.

Novacentrix® Metalon® JS-B25P silver ink on PET sensors cured at 90C for 30 minutes were also tested on a 4 in. dome structure. The initial resistance of the silver ink was around half that of the air-dried silver ink on PET. The resistance increased when put into tension and decreased when returned to its original shape. Similar to the air-dried silver ink on PET sensors, the resistance trended downward during repetitive cycling. The oven-cured silver ink on PET trended downward for all 100 cycles. There were not any visible cracks in the SEM images of the silver structure. The lack of cracking explains the lack of resistance increase during cyclic loading. The decrease of resistance during testing is believed to be caused by the same mechanism as with the air-dried PET samples.

A third type of sensor was fabricated by printing Sun Chemical® Suntronic™ EMD 5730 silver ink on LCP and curing in an oven at 200°C. This ink had an average resistance of 24.55 ohms, significantly lower than the other two ink categories. This sensor was subjected to a 4 in. saddle-like bend test. The resistance of the ink increased when conformed to the surface and decreased when returned to its original flat shape. The resistance of the ink increased for all 300 cycles it was subjected to. After 300 cycles, the resistance had increased by over 20%. The lack of a resistance decrease like that seen from the PET samples is believed to be due to more densification from the higher curing temperature and the lack of a microporous coating on the LCP. The silver ink structure was imaged at 0, 100, 200, 250, and 300 cycles. Cracks were first observed at the corner location at 200 cycles and the side location at 250 cycles. The cracks in the corner location

prorogated at an angle of approximately 45 degrees while those in the side location propagated horizontally.

While testing antenna samples using the developed fixtures, it is seen through S-parameter measurements that there is minimal effect in the resonant frequency of the antennas or the bandwidth when the antennas are deformed over barrel-like or saddle-like shapes. This is because the shapes had a relatively large radius of curvature – 4 x 40 in. (101.6 x 1016.0 mm) compared to the thickness of the antenna samples (729 um for LCP and 1034 um for Pyralux®). The uniaxial bending only created minor differences in S11 results for the antenna compared to the flat or unbent reading. The gain results, however, did seem to be affected by the different uniaxial bend scenarios. In addition, the presence of the environmental coating on the printed silver LCP antenna did have a noticeable effect on the S11 measurements. Although the developed fixtures are helpful to assess the performance of antennas, one limitation of this test method is that when testing the electrical performance of antennas when conformed to complex surfaces, the gain cannot be accurately measured due to the antenna being sandwiched between two fixtures.

The mechanical properties of oven cured silver nanoparticle ink was found to be considerably different than that of bulk silver. The modulus was measured using nanoindentation and was found to be 13.5 GPa, considerably less than that of bulk silver. By increasing the temperature or time of curing the ink, the densification of the structure could be increased and lead to a higher modulus.

A finite-element model was created of the LCP sensor to determine the stress and strain distributes when conformed to 4 in. dome and 4 in. saddle-like surfaces. The max

principal and max shear stress contours were observed at the side and corner locations of the geometry where the SEM images were taken on the physical sample. It was observed that the cracks seen in the physical sample were perpendicular to the max principal stress and parallel to the max shear stress contours seen in the finite element simulations. This shows that these simulations can be used to predict the directions in which the fatigue cracks will propagate.

A finite element model of the 2x2 LCP antenna was also created to investigate the stress and strain seen in the ink structures when conformed to 4 x 40 in. saddle-like and 4 x 40 in. barrel-like surfaces. It was observed that the most likely area of cracking is the curved section of the slot of the top ink patches. Therefore, in order to decrease cracking that would occur during cyclic loading, the top ink patch geometry should be modified to decrease the stress concentration seen in the curved section of the slots.

10.2 Contributions

This thesis has investigated the performance of flexible electronics conformed over complex surfaces. The contributions of this work are:

- Complex surfaces with interconnect-access were designed and fabricated for testing flexible electronic prototypes, and the developed surfaces were used to test strain sensors and antennas. The developed test fixtures and the test method are one of the first for testing flexible electronic elements.
- In-situ resistance changes in strain sensors were measured and were correlated to cracking in the silver ink through SEM images as well as to stress/strain contours in the silver ink through numerical simulations.

- Antenna performance was measured when conformed to complex surfaces in addition to uniaxial bending. This provides insight into how the antenna would behave in a realistic case where it is conformed to a complex surface. Numerical simulations of the antenna were carried out that provide insight into likely failure locations when conformed to complex surfaces and where the geometry could be modified to decrease the chance of failure.

10.3 Future Work

There are various areas of this research that could be further explored. Major areas for further research include:

- Running tests of printed sensors until complete failure. This would provide information about the fatigue life.
- Testing the antenna on smaller radii to understand the effect on S11 parameters as well as gain measurements.
- Testing more combinations of substrate and ink materials on more surface geometries to obtain a broader understanding of how different materials behave on different surfaces.
- Running more tests of Sun Chemical® Suntronic™ EMD 5730 ink sensor samples with different curing parameters to investigate the effect of ink densification on fatigue behavior.
- Performing nanoindentation on Sun Chemical® Suntronic™ EMD 5730 ink for different curing time and temperatures to find the effect of curing parameters on modulus.

- Performing cyclic loading tests on antennas while obtaining measurements in situ to provide insight into the antenna performance degradation while being repeatedly conformed to complex surfaces. This testing would provide useful life estimates for the antenna.
- Adding adhesion values between printed inks and substrates in finite element models to investigate delamination when conformed to complex surfaces.
- Obtaining more information about material properties to create elastic-plastic material models for finite element models.

REFERENCES

1. Hannu Sillanpää, E.H., Toni Liimatta, and Matti Mäntysalo *Inkjet Printed Wireless Biosensors on Stretchable Substrate*. in *2014 International Conference on Electronics Packaging*. 2014. Toyama, Japan: IEEE.

2. Dae-Hyeong Kim, R.G., Nanshu Lu, and John A. Rogers, *Flexible and stretchable electronics for biointegrated devices.* Annual Review of Biomedical Engineering, 2012. **14**.

3. Tentzeris, S.K.a.M.M., *Parylene coated waterproof washable inkjet-printed dual-band antenna on paper substrate.* International Journal of Microwave and Wireless Technologies, 2018. **10**(7): p. 814-818.

4. Tentzeris, B.S.C.a.M.M. *A miniaturized wearable high gain and wideband inkjet-printed AMC antenna*. in *2013 IEEE Antennas and Propagation Society International Symposium (APSURSI)*. 2013. Orlando, FL, USA: IEEE.

5. Yi Li, R.T., Steve Beeby and John Tudor *An all-inkjet printed flexible capacitor on a textile using a new poly(4-vinylphenol) dielectric ink for wearable applications*. in *SENSORS, 2012 IEEE*. 2012. Taipei, Taiwan: IEEE.

6. Dae-Hyeong Kim, Y.-S.K., Jian Wu, Zhuangjian Liu, Jizhou Song, Hoon-Sik Kim, Yonggang Y. Huang, Keh-Chih Hwang, and John A. Rogers, *Ultrathin silicon circuits with strain-isolation layers and mesh layouts for high-performance electronics on fabric, vinyl, leather, and paper.* Advanced Materials, 2009. **21**: p. 3703-3707.

7. Yoshihiro Kawahara, S.H., Benjamin S. Cook, Cheng Zhang, and Gregory D. Abowd. *Instant inkjet circuits: lab-based inkjet printing to support rapid prototyping of UbiComp devices*. in *2013 ACM international joint conference on Pervasive and ubiquitous computing*. 2013. Zurich, Switzerland: ACM.

8. Dirk Godlinski, R.Z., Volker Zöllmer, and Reinhard R. Baumann, *Printing technologies for the manufacturing of passive microwave components: antennas.* IET Microwaves, Antennas & Propagation, 2017. **11**(14): p. 2010-2015.

9. Bruce H. King, M.J.O.R., and Stephen M. Barnes *Characterzing aerosol Jet®multi-nozzle process parameters for non-contact front side metallization of silicon solar cells*, in *34th IEEE Photovoltaic Specialists Conference (PVSC)*. 2009, IEEE: Philadelphia, PA, USA.

10. Thomas Reitberger, J.F., Gerd-Albert Hoffmann, Ludger Overmeyer, Lukas Lorenz, and Klaus-Juergen Wolter, *Integration of Polymer Optical Waveguides by Using Flexographic and Aerosol Jet Printing*, in *12th International Congress Molded Interconnect Devices (MID)*. 2016, IEEE: Wurzburg, Germany.

11. DuPont, *DuPont Kapton HN*. 2011.

12. Wypych, G., *PET poly(ethylene terephthalate)*, in *Handbook of Polymers*. 2016, ChemTec Publishing. p. 398-403.

13. Mahnke, J.F.a.D., *Flexible Circuit Materials*, in *Flexible Circuit Technology*, D. Neer, Editor. 2011, BR Publishing: Seaside, OR. p. 126-166.

14. Jongwoo Lim, J.K., Young Joon Yoon, Hyotae Kim, Ho Gyu Yoon, Sung-Nam Lee, Jonghee Kim, *All-inkjet-printed Metal-Insulator-Metal (MIM) capacitor.* Current Applied Physics, 2012. **12**: p. e14-e17.

15. Abhinav M. Gaikwad, D.A.S., Tse Nga Ng, David E. Schwartz, and Gregory L. Whiting, *A flexible high potential printed battery for powering printed electronics.* Applied Physics Letters, 2013. **102**(23).

16. Lee, S.-Y. *Beyond flexible batteries: aesthetically versatile, printed rechargeable power sources for smart electronics*. in *SPIE Defense + Security*. 2017. Anaheim, California: SPIE.

17. Justin H. Chow, C.M., Joseph May, and Suresh K. Sitaraman. *Study of Wearables with Embedded Electronics through Experiments and Simulations*. in *2018 IEEE 68th Electronic Components and Technology Conference (ECTC)*. 2018. San Diego, CA, USA: IEEE.

18. Gi-Dong Sim, Y.H., Hyun-Ho Kim, Soon-Bok Lee, and Joost J. Vlassak, *Fatigue of polymer-supported Ag thin films.* Scripta Materialia, 2012. **66**(11): p. 915-918.

19. Maria A. Torres Arango, A.M.C., Jared J. Beard, and Konstantinos A. Sierros *Direct writing and electro-mechanical characterization of Ag micro-patterns on polymer substrates for flexible electronics.* Thin Solid Films, 2015. **596**: p. 167-173.

20. Rui Chen, J.C., Christine Taylor, Jeffrey Meth, and Suresh K. Sitaraman. *Adaptive Curvature Flexure Test to Assess Flexible Electronic Systems*. in *2018 IEEE 68th Electronic Components and Technology Conference (ECTC)*. 2018. San Diego, CA, USA: IEEE.

21. Eerik Halonen, A.H., Tapio Karinsalo, Pekka Iso-Ketola, Matti Mäntysalo, Riku Mäkinen. *Dynamic Bending Test Analysis of Inkjet-Printed Conductors on Flexible Substrates* in *2012 IEEE 62nd Electronic Components and Technology Conference (ECTC)*. 2012. San Diego, CA, USA: IEEE.

22. Jackson, H.U.L.a.T.N., *Flexibility Testing Strategies and Apparatus for Flexible Electronics.* IEEE Transactions on Electron Devices, 2016. **63**(5): p. 1934-1939.

23. ASTM, *Standard Test Method for Determining the Effects of Bending a Membrane Switch or Printed Electronic Device*. 2016, ASTM.

24. ASTM, *Standard Test Methods of Tension Testing of Metallic Foil*. 2016, ASTM.

25. T. Li, Z.Y.H., Z.C. Xi, S.P. Lacour, S. Wagner, and Z. Suo *Delocalizing strain in a thin metal film on a polymer substrate.* Mechanics of Materials, 2005. **37**(2-3): p. 261-273.

26. Suo, T.L.a.Z., *Deformability of thin metal films on elastomer substrates.* International Journal of Solids and Structures, 2006. **43**(7-8): p. 2351-2363.

27. Street, J.R.G.a.R.A., *Mechanical characterization of solution-derived nanoparticle silver ink thin films.* Journal of Applied Physics, 2007. **101**(10).

28. Wang, J.C., *Young's modulus of porous materials.* Journal of Materials Science, 1984. **19**: p. 801-808.

29. Andrew A. Wereszczak, D.J.V., Hsin Wang, Mattison K. Ferber, and Zhenxian Liang, *Properties of Bulk Sintered Silver As a Function of Porosity*. 2012, Oak Ridge National Laboratory: Oak Ridge, TN, USA.

30. Nanshu Lu, X.W., Zhigang Suo, and Joost Vlassak, *Metal films on polymer substrates stretched beyond 50%.* Applied Physics Letters, 2007. **91**(22).

31. O. Glushko, A.K., E.J.W. List-Kratochvil, M.J. Cordill, *Relationship between mechanical damage and electrical degradation in polymer-supported metal films subjected to cyclic loading.* Materials Science & Engineering A, 2016. **662**: p. 157-161.

32. Byoung-Joon Kim, H.-A.-S.S., Ji-Hoon Lee, and Young-Chang Joo, *Effect of cyclic outer and inner bending on the fatigue behavior of a multi-layer metal film on a polymer substrate.* Japanese Journal of Applied Physics, 2016. **55**(6S3).

33. Sang-Il Park, J.-H.A., Xue Feng, Shuodao Wang, Yonggang Huang, and John A. Rogers, *Theoretical and Experimental Studies of Bending of Inorganic Electronic Materials on Plastic Substrates.* Advanced Functional Materials, 2008. **18**(18): p. 2673-2684.

34. Taha A. Elwi, H.M.A.-R., Daniel G. Rucker, and Haider R. Khaleel, *Effects of twisting and bending on the performance of a miniaturized truncated sinusoidal printed circuit antenna for wearable biomedical telemetry devices.* International Journal of Electronics and Communications (AEÜ), 2011. **65**(3): p. 217-225.

35. Liu, Y.C.L.a.T.X., *Deformation of Multilayer Flexible Electronics Subjected to Torque.* Experimental Techniques, 2011. **38**(1): p. 13-20.

36. Justin Chow, K.K., Gabriel Cahn, Rui Chen, Jeffrey S Meth, Olivier Pierron, Samuel Graham, and Suresh Sitaraman. *Stretch Testing of Flexible Electronics*. in *2018FLEX*. 2018. Monterey, CA, USA: SEMI.

37. Sari Merilampi, T.B., Veikko Haukka, Pekka Ruuskanen, Leena Ukkonen, Lauri Sydänheimo *Analysis of electrically conductive silver ink on stretchable substrates under tensile load.* Microelectronics Reliability, 2010. **50**(12): p. 2001-2011.

38. Pecht, A.M.a.M., *A stretchable and screen-printable conductive ink for stretchable electronics.* Applied Physics Letters, 2016. **109**(18).

39. Sang Min Yang, Y.S.L., Yonghee Jang, Doyoung Byun, and Sung-Hoon Choa, *Electromechanical reliability of a flexible metal-grid transparent electrode prepared by electrohydrodynamic (EHD) jet printing.* Microelectronics Reliability, 2016. **65**: p. 151-159.

40. J. A. Quintero, R.D.M., A. W. C. De Oliveira, D. C. Rolim, O. C. Da Silva, and J. M. Silva Neto *Electro-mechanical evaluation of Ag trace patterns by ink-jet printing*, in *11th Electronics Packaging Technology Conference* 2009, IEEE: Singapore. p. 1000-1005.

41. Novacentrix, *Metalon® JS-B25P*, Novacentrix, Editor. 2016.

42. Novacentrix, *Novele™ IJ-220.* 2011.

43. Chemical, S. *Nanosilver Conductive Ink EMD5730*. 2013.

44. Cordill, O.G.a.M.J., *Electrical Resistance Decrease Due to Grain Coarsening Under Cyclic Deformation.* The Journal of The Minerals, Metals & Materials Society (TMS), 2014. **66**: p. 598-601.

45. MatWeb. *Silver, Ag*. Available from: http://www.matweb.com/search/datasheet.aspx?matguid=63cbd043a31f4f739ddb7632c1443d33&ckck=1.

46. Corporation, R., *Ultralam 3850HT Liquid Crystalline Polymer Circuit Material Double-Clad Laminates*. 2016.

47. Pilkey, W.D., *Formulas for Stress, Strain, and Structural Matrices*. 2nd ed. 2005: John Wiley & Sons.